Technische Universität München

Department of Electrical Engineering and Information Technology

Institute for Communications and Navigation

Prof. Dr. sc. nat. Christoph Günther

Master thesis

Partial ambiguity fixing for precise point positioning with multiple frequencies in the presence of biases

Supervisor: Dipl.-Ing. Patrick Henkel

Author: Víctor Danubio Gómez Pantoja

victor.gomez.pantoja@mytum.de

Started: 01.09.2008

Completed: 20.03.2009

Contents

Acknowledgement

I would like to thank Prof. Dr. sc. nat. Christoph Günther for the cordially incorporation to his team and for giving me the chance to fulfill my master thesis on this interesting research topic.

I am greatly thankful to my supervisor, Patrick Henkel, for the allocation of this very interesting topic, for his always friendly and excellent provided support, and for his singular suggestions and ideas to improve this work.

My sincere thanks to Kaspar Giger and Vladimir Kuryshev for their help and friendly discussions.

Besides, I would like to thank the family of my girlfriend Linda, particularly her parents, for all their support in Germany.

Especially, I want to thank my family, mainly my parents for all their support, trust and affection, as well as my sisters, Silvia and Perla, and my brothers, Goyo and Héctor, for all their help and advice.

Finally, I want to express my special gratitude to mi lovely pequeñita Linda for her support in all respects and invaluable company.

Chapter 1

Introduction

The use of Global Navigation Satellite Systems (GNSS) for navigation, surveying and geophysics has continuously increased over the last decades. However, not only the demand has increased but also the requirements on accuracy, precision, reliability, availability and continuity of the systems. Therefore, a new generation of GNSS is built, the European Galileo system, and a modernization of the first and current Global Positioning System (GPS) is also on track.

In order to meet the more stringent with respect to precision, integrity and real-time positioning, carrier phase measurements are used. These measurements are extremely precise but ambiguous by an unknown number of cycles, which are known to be integer-valued. For solving this problem integer ambiguity resolution algorithms have been developed. The integer estimation process usually consists of three steps: First, a standard least-squares method is applied by disregarding the integer property of the ambiguities and the so-called float solution is obtained. In the second step, the integer constraint of the ambiguities is considered, i.e. the float ambiguities are mapped to integer values. Different choices for this mapping are available. The most simple, for example, is by rounding to the nearest integer value. However, for this choice between different estimators, the probability of correct integer estimation should be taken into account. Finally, the fixed integer-valued ambiguities are use to adjust the remaining unknown parameters by their correlation.

The least-squares integer ambiguity decorrelation adjustment (LAMBDA) proposed by Teunissen in [1] is widely applied for integer ambiguity resolution. After obtaining the float solution, an integer-valued ambiguity decorrelation transformation is computed from the covariance matrix of the float ambiguities by alternating integer-approximated Gaussian eliminations and permutations of ambiguities (de Jonge and Tiberius [2]). Afterwards, a

search and a back-transformation from the decorrelated search space into the original ambiguity space is performed by using the inverse of the decorrelation matrix. This integer decorrelation transformation has been originally derived for unbiased measurements where it performs very well; however, it becomes critical for biased measurements as it amplifies the biases, which affects the reliability of the ambiguity resolution. Therefore, a partial integer decorrelation is suggested to achieve an optimum trade-off between the noise variance reduction and the biases amplification. The LAMBDA method was originally used for double-difference (DD) carrier phase measurements. However, it can be applied also to single-difference (SD) measurements.

A successful resolution of all ambiguities, also known as *Full Ambiguity Resolution*, may not always be possible (i.e. the probability of correct integer estimation is too low). Severe multipath or large uncorrected biases may prevent this reliable resolution. However, a reliable resolution of a subset of the ambiguities can still be possible, also referred to as *Partial Ambiguity Resolution* and introduced by Teunissen et al. in [3]. The aim of partial ambiguity resolution is to identify the subset of ambiguities which gives the largest possible probability of correct integer estimation. Partial ambiguity fixing for double-differences have been analyzed by Cao et al. in [4] with a short baseline.

On this thesis, different partial ambiguity fixing methods in the presence of biases are investigated for carrier phase absolute positioning with satellite-satellite single-difference measurements at a single epoch. A *new* partial ambiguity fixing method is used for sequential fixing, which considers all the possible orders of fixing to obtain an optimum largest subset of fixable ambiguities. This new method is the so-called *Sequential optimum fixing order search* (SOFOS) method. Moreover, a *new* exponential profile is suggested to upper-bound the residual biases.

This thesis is outlined as follows. In Chapter 2, a brief introduction to the current and future Global Navigation Satellite Systems is given. The GNSS measurement model is also introduced.

In Chapter 3 absolute carrier phase positioning and the ambiguity resolution problem are described. Three different methods to simplify and improve the ambiguity resolution are discussed: Satellite-satellite single differences (SD), linear combinations and carrier smoothing. The derivation of a *new* four-frequency code-carrier linear combination for Galileo is also presented. Furthermore, three integer estimators are briefly described: integer rounding, integer bootstrapping and integer least-squares. Finally, the quality of the ambiguity estimates is analyzed.

The presence of biases on the GNSS measurements and how they affect the ambiguity resolution is analyzed in Chapter 4. A biased carrier phase absolute positioning model using the simplification methods from the previous chapter is discussed. Moreover, an upper-bound for the biases is derived by using an exponential bias profile. Furthermore, due to the amplification of the biases from the ambiguity decorrelation transformation matrix of the LAMBDA method, a partial integer decorrelation is discussed. Finally, partial ambiguity fixing is introduced for severe multipath and large uncorrected biases.

In Chapter 5 different partial ambiguity fixing methods using sequential and batch fixing are described. The methods are implemented in Matlab®, and simulations are used to investigate their performance. The comparison of their performance is presented in Chapter 6.

Finally, the conclusions are summarized and an outlook is given in Chapter 7.

Chapter 2

Global Navigation Satellite Systems

Global Navigation Satellite Systems (GNSS) are built of medium earth orbit (MEO) satellites that provide a global coverage for positioning with applications in navigation, surveying, location-based services and geophysics. Four global navigation systems – GPS, Galileo, GLONASS and Compass – will be available within the next years. A brief description of them is given below. The frequency allocations for their signals (Misra and Enge [5], InsideGNSS [6], and Verhagen [7]) are illustrated in Figure 2.1.

2.1 GNSS projects

GPS

The *Global Positioning System* (GPS), developed by the U.S. Air Force in the 1970's, is the first operational GNSS, and is currently the most utilized satellite navigation system on the world. The fully operational GPS constellation consists of 24 MEO satellites, divided over 6 orbital planes, but it can uses up to 32 satellites. The orbital inclination angle is 55, with an orbital radius of 26,600 km. GPS transmits currently on two radio frequencies in the L-band using code division multiple access CDMA techniques. On the L1 (*Link* 1) band, centered at 1575.42 MHz, two signals are transmitted, the free coarse acquisition (C/A) code for civil users, and the military precision P-code for military users. One P-code for military users is transmitted at the L2 band, centered at 1227.60 MHz. Civil users can only access the P-code encrypted form (Y-code).

The frequency band L5, centered at 1176.45 MHz, is being added to the system, under the GPS modernization plan, and the codes transmitted on it will be freely available. In

addition, a civil signal is being introduced at the L2 band, and a modernized M-code signal for military users is currently being implemented on L1 and L2 bands.

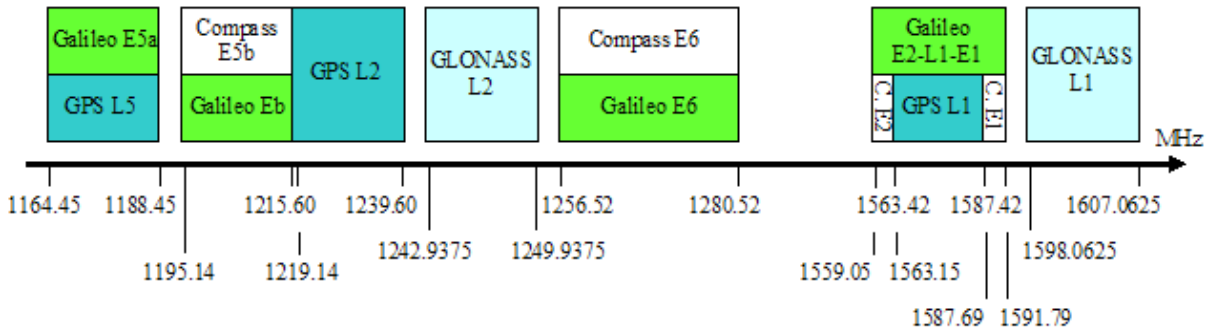

Figure 2.1: Frequency allocations for GPS, GLONASS, Galileo and Compass.

GLONASS

The Russian acronym GLONASS stands for *GLObal'naya NAvigationsnaya Sputnikovaya Sistema*, which literally is the Russian's GNSS. It is chronologically the world's second GNSS system. The satellite constellation consists of 24 satellites and can be described compactly as a Walker 24/3/2 with an orbital inclination angle of 64.8, and an orbital radius of 25,500 km. GLONASS transmits also on the L1 (1598.0625–1607.0625 MHz) and L2 (1242.9375–1249.9375 MHz) frequency bands using frequency division multiple access FDMA techniques.

Due to the fall of the Soviet Union and the followed economical collapse, a full GLONASS constellation was available only for a short time in 1995; thereafter, it declines to only seven operational satellites in 2001. That year, a GLONASS modernization program was initiated. It is expected a fully operational constellation by 2011. Furthermore, the addition of a third frequency in the band 1190–1212 MHz as well as a CDMA signal is being evaluated.

Note: A *Walker constellation* (Walker $T/P/F$), represents a satellite constellation of T satellites in circular orbits, divided over P equally spaced orbital planes. The satellites are evenly distributed in each orbit and the relative spacing of the satellites between adjacent planes is F in units of $360°/T$.

Galileo

Galileo is the currently under development European's Union GNSS. In contrast to GPS, it will be an independent and civilian system. The project has been led by a 50-50 partnership between the European Commission (EC) and the European Space Agency (ESA). It will have international participation and investment, and will be interoperable and compatible with GPS and GLONASS systems. The Galileo constellation, compactly described as a Walker 27/3/1, will consist of 30 satellites, divided over 3 orbital planes (9 operational satellites and one active spare). The orbital inclination will be 56 and the orbital radius of 29,600 km. Galileo signals will be transmitted using CDMA techniques on four frequency bands: E5a (1176.45 MHz), E5b (1207.14 MHz), E6 (1278.75 MHz) and E2-L1-E1 (1575.42 MHz).

- **Services**

Galileo signals will be assigned to provide the following types of services (Ávila et al. [8]), which are summarized in Table 2.1.

Open Service (OS): Free-accessible use for anyone, providing basic navigation.

Commercial Service (CS): Fee-based service offering additional commercial data, service availability and higher accuracy than the OS.

Safety-of-Life Service (SoL): Fee-based service aimed to safety-critical transport applications (e.g. air-traffic control) offering integrity reliability and authentication of the signal, certification and guarantee of service.

Public Regulated Service (PRS): Fee-based service aimed to security authorities and military applications offering the same services as SoL. Additionally, it uses encrypted PRS codes and anti-jamming signals.

Search And Rescue Service (SAR): Used for detection of distress alerts and coordination of search-rescue teams.

Table 2.1: Galileo services mapped to signals.

Frequency band	OS	CS	SoL	PRS	SAR
E5a	√	√			
E5b	√	√	√		
E6		√		√	√
E1	√	√	√	√	

Compass

Compass is a GNSS project to be developed by China. The Compass constellation will consist of 35 satellites (5 geostationary orbit (GEO) satellites and 30 MEO satellites). Compass signals will be transmitted on the E1 (1587.69–1591.79 MHz), E2 (1559.05–1563.15 MHz), E5b (1195.14–1219.14 MHz) and E6 (1256.52–1280.52 MHz) frequency bands. It will offer an open and a restricted service.

2.2 GNSS Measurements

Two types of measurements result from processing the GNSS signals: code and carrier phase measurements.

2.2.1 Code measurements

Code tracking provides a coarse measure of the distance between the satellite and the receiver, also referred to as pseudorange. It estimates the apparent transit time of the signal, defined as the difference between the signal reception time at the receiver and the signal transmission time at the satellite. The corresponding pseudorange is defined as the given transit time multiplied by the speed of light in vacuum

$$\rho(t) = c[t_u(t) - t^k(t-\tau)], \tag{2.1}$$

where $t_u(t)$ is the reception time at user u; $t^k(t-\tau)$ is the transmission time from satellite k; c is the speed of light in vacuum; and τ is the travel time of the signal.

This measurement is biased by the receiver and satellite clocks, which are not equal and also differ from the GPS Time (GPST). Taking into account these errors into equation (2.1) yields

$$\rho(t) = c[(t + \delta t_u(t)) - (t - \tau + \delta t^k(t-\tau))] = c[\tau + (\delta t_u(t) - \delta t^k(t-\tau)], \tag{2.2}$$

where $\delta t_u(t)$ and $\delta t^k(t-\tau)$ are the receiver and satellite clock offsets, respectively.

Atmospheric effects (ionospheric and tropospheric delays), multipath, orbital errors and noise also affect the code measurements. A brief explanation of them will be given in Section 2.2.3. Extending the code measurement model of user u, satellite k on frequency m and epoch i

yields

$$\begin{aligned}\rho^k_{u,m}(t_i) &= r^k_u(t_i) + T^k_u(t_i) + q^2_{1m} I^k_u(t_i) + \delta r^k_u(t_i) \\ &\quad + c(\delta\tau_u(t_i) - \delta\tau^k(t_i)) + b_{\rho_{u,m}} + b^k_{\rho_m} + \varepsilon^k_{\rho_{u,m}}(t_i),\end{aligned} \tag{2.3}$$

where $r^k_u = c\tau$, is the satellite-user range; T^k_u is the tropospheric delay; I^k_u is the ionospheric delay depending on the ratio of frequencies q_{1m}; δr^k_u is the projected satellite orbital error; $b_{\rho_{u,m}}$ and $b^k_{\rho_m}$ are the receiver and the satellite code biases including instrumental delays; $\varepsilon^k_{\rho_{u,m}}$ is the code noise including multipath; $\delta\tau_{u,m}$ is the receiver clock error; and $\delta\tau^k_m$ is the satellite clock error.

2.2.2 Carrier phase measurements

The carrier phase measurement is much more precise than the code measurement. It is defined as the difference between the phase of the carrier received from the satellite and the phase of the receiver-generated carrier signal at the instant of the measurement. The phase is measured in terms of the number of cycles generated or received since the starting point at zero time. Then, the carrier phase measurement will be the measured fractional cycle plus an unknown number of whole cycles, which is also called *integer ambiguity*.

The carrier phase measurement in units of meters (Φ) at the user u from satellite k on frequency m at epoch i is modeled as

$$\begin{aligned}\Phi^k_{u,m}(t_i) = \lambda_m \phi^k_{u,m}(t_i) &= r^k_u(t_i) + T^k_u(t_i) - q^2_{1m} I^k_u(t_i) + \lambda_m N^k_{u,m} + \delta r^k_u(t_i) + \lambda_m b_{\phi_{u,m}} \\ &\quad + c(\delta\tau_u(t_i) - \delta\tau^k(t_i)) + \lambda_m b^k_{\phi_m} + \varepsilon^k_{\phi_{u,m}}(t_i),\end{aligned} \tag{2.4}$$

where λ_m is the wavelength of the carrier; r^k_u, is the user-satellite range; T^k_u is the tropospheric delay; I^k_u is the ionospheric delay depending on the ratio of frequencies q_{1m}; δr^k_u is the projected satellite orbital error; $b_{\phi_{u,m}}$ is the receiver phase noise; $b^k_{\phi_m}$ is the satellite phase bias; and $\varepsilon^k_{\phi_{u,m}}$ is the phase noise including multipath. In contrast to the code measurements, the phase ionospheric delay is negative and the phase multipath is also different, which will be explained on the next section. Note that the multiplication of the phase noise and biases by the wavelength will be later stipulated on the notation $b_{\phi_{u,m}}, b^k_{\phi_m}$ and $\varepsilon^k_{\phi_{u,m}}$.

The carrier phase measurements are extremely precise, but affected by integer ambiguities, whose estimation can be performed by a variety of algorithms (e.g. LAMBDA, *Three-Carrier Ambiguity Resolution* (TCAR) (Forssell et al. [9]), Rounding, ... etc.).

2.2.3 Measurement's errors and delays

Receiver noise, multipath, errors in the navigation message from the satellite and atmospheric delays are different kind of error sources, which affect the precision of the GNSS measurements.

Ephemeris and clock errors

The satellite computed orbit or *ephemeris* is uploaded to the satellite to be broadcast in their navigation message over several days. It offers the states of the satellites and their clocks. Errors on the estimation and prediction of the ephemeris parameter values result in a false satellite predicted orbit. Therefore, the more accurate are the prediction models, and the more frequent the ephemeris uploads, the lower the sizes of the range errors.

Atmospheric delays

The earth's atmosphere modifies the speed and direction of propagation of the GNSS signals. This effect, referred to as *refraction*, generates a propagation delay, i.e. the signal transit time is changed. Two layers of the atmosphere affect particularly the propagation of the GNSS signals: the ionosphere and the troposphere.

• Ionospheric delay

The ionosphere is the layer of the earth's atmosphere that is ionized by solar radiation. It extends from 50km to 1000km above the surface of the Earth. The UV radiation of the sun heats the neutral gas molecules, which then break and liberate free electrons and ions. This process is referred to as *ionization*. Depending upon the solar activity, the free electron density varies considerable.

The ionosphere is a dispersive medium for radio signals, which means that the ionospheric delay depends on the frequency of the signal. The ionosphere effects are inversely proportional to the square of the frequency of the signal. The first order ionospheric delays can be estimated by collecting measurements on different frequencies

$$q_{1m}^2 = \frac{f_1^2}{f_m^2} = \frac{\lambda_m^2}{\lambda_1^2}.$$

The number of free electrons in the path of a signal affects the code and carrier phase measurements differently, but with the same magnitude. That is, in the ionosphere, the

phase velocity of the GNSS carrier signals exceeds that of light in vacuum, whereas the group velocity is delayed. Therefore, the ionospheric phase delay is negative (see equation (2.4)), i.e. the phase is advanced.

- **Tropospheric delay**

The troposphere, composed of dry gases and water vapor, is the lower layer of the earth's atmosphere, and generates also a signal delay. It extends from the surface of the Earth to about 9 km above the poles and about 16 km above the equator. In contrast to the ionosphere, the troposphere is a non-dispersive medium for GNSS frequencies, i.e. the propagation delay does not depend on the frequency of the signal. Furthermore, the phase and group velocities are the same; therefore the tropospheric delays are equal for the code and carrier phase measurements.

The tropospheric delay can not be estimated from GNSS measurements, consequently tropospheric models and mapping functions are used to correct for it. Typically, the tropospheric delay is separated into a wet delay T_w, caused by the water vapor; and a dry delay T_d, caused by dry air and some water vapor, so that

$$T = T_d + T_w.$$

The tropospheric wet delay is much harder to model than the dry delay, which is fortunately larger and can be predicted with higher accuracy.

Random measurement noise

The code and carrier phase measurements are affected also by random errors unrelated to the signal, e.g. noise introduced by the antenna, signal quantization noise and interference from other signals. This noise is also called receiver noise and varies with the signal strength.

Multipath

Multipath refers to the effect of a signal arriving at an antenna via two or more paths due to the reflections of the direct path (i.e. line-of-sight) from buildings, structures and from the ground. The reflected signals are delayed and usually weaker than the direct signal. The magnitudes of the errors induced by multipath on the code and carrier phase measurements differ significantly. In the code measurements, it varies between 1 m and 5 m, whereas the

corresponding error in the carrier phase measurements is 1–5 cm. Moreover, the multipath error in the carrier phase measurements does not exceed a quarter cycle if the amplitude of the reflected signal is smaller than the amplitude of the direct signal.

Chapter 3

Carrier Phase Positioning and Integer Ambiguity Resolution

The precision and accuracy given by the code and carrier phase measurements are very different. The carrier phase measurements offer a very-high precision (order of millimeters), whereas the code measurement's precision is in the order of meters. Carrier phase measurements are therefore required for precise positioning. However, they are ambiguous (integer ambiguities); consequently, integer ambiguity resolution is necessary before the measurements can be used for precise positioning. Integer ambiguity resolution consists of an estimation and a validation part [10]. This means that given the estimates of the integers, it is necessary to prove their precision and accuracy in order to obtain precise position estimates. In the following section, some methods to improve the performance of ambiguity resolution for absolute carrier phase positioning are described. Moreover, an overview of some usually ambiguity resolution methods will be given on Section 3.3. Finally, a form to calculate their probability of correct estimation is shown on Section 3.4.

3.1 Simplification methods for ambiguity resolution

Usually, in the case of precise relative positioning, ambiguity resolution is done by using double-difference (DD) carrier phase measurements (see Appendix A), which are used to reduce nuisance parameters on the measurements. However, another methods, discussed below, can also be used to improve the performance of ambiguity resolution, and for absolute carrier phase positioning as will be discussed on Chapter 4.

3.1.1 Linear combinations

Integer ambiguity resolution of the carrier phase measurements can be simplified by using linear combinations of the measurements at multiple frequencies. The design of ionosphere-free mixed code-carrier linear combinations of minimum noise and maximum combination discrimination for Galileo has been performed by Henkel and Günther in [11] and [12]. An overview of the design and characteristics of these combinations is described below. Furthermore, this work has been extended to four-frequency Galileo combinations (E1-E5a-E5b-E6), which design and comparison to other combinations is introduced on Section 3.1.2.

Code-carrier linear combinations

Given the carrier phase measurements from Equation (2.4) and the code measurements from Equation (2.3), a linear combination of them at multiple frequencies can be done in order to obtain a larger wavelength and a low noise level, while the ionospheric delay is eliminated. Hence, the carrier phase and code measurements should be weighted by the corresponding coefficients, α_m and β_m. An illustration of this is shown in Figure 3.1. The properties of the linear combination at M frequencies are regulated by doing some constraints on the weighting coefficients:

Geometry-preserving (GP): The user-satellite range r should be preserved by

$$\sum_{m=1}^{M} \alpha_m + \sum_{m=1}^{M} \beta_m \stackrel{!}{=} 1, \tag{3.1}$$

where the phase part $\sum_{m=1}^{M} \alpha_m$ will be weighted by the carrier phase geometric weight τ_{lc}, and the code part $\sum_{m=1}^{M} \beta_m$ by $(1 - \tau_{lc})$. This constraint refers also to the non-dispersive errors, i.e. the satellite orbital errors, the satellite clock offsets and the tropospheric delays are not amplified.

Ionosphere-free (IF): The ionospheric delay I of first order is eliminated if

$$\sum_{m=1}^{M} \alpha_m q_{1m}^2 - \sum_{m=1}^{M} \beta_m q_{1m}^2 \stackrel{!}{=} 0. \tag{3.2}$$

Integer-preserving (NP): The combination of N_m ambiguities should be an integer multiple of a common wavelength λ_{lc}, that is

$$\sum_{m=1}^{M} \alpha_m \lambda_m N_m \stackrel{!}{=} \lambda_{lc} N, \tag{3.3}$$

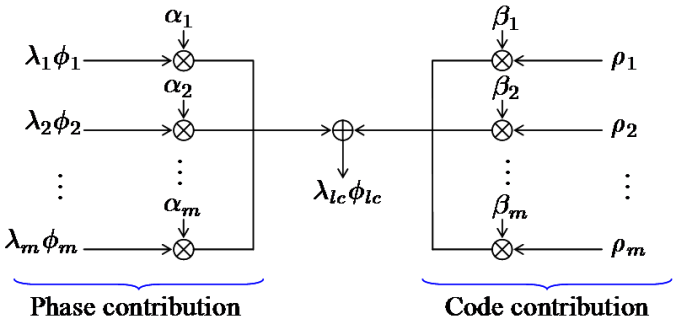

Figure 3.1: Code-carrier linear combination scheme.

which can be split into the next integer conditions

$$j_m = \frac{\alpha_m \lambda_m}{\lambda_{lc}} \in \mathbb{Z}, \tag{3.4}$$

where $\mathbb{Z}$ denote the space of integers.

The wavelength of the code-carrier combination is obtained as follows

$$\lambda_{lc}(\tau_{lc}) = \frac{\tau_{lc}}{\sum_{m=1}^{M} \frac{j_m}{\lambda_m}} = \tilde{\lambda}\tau_{lc} \qquad \text{with} \qquad \tilde{\lambda} = \frac{1}{\sum_{m=1}^{M} \frac{j_m}{\lambda_m}}. \tag{3.5}$$

A combination discrimination indicator is given as a cost function in order to select the linear combinations. This has been defined by Henkel and Günther in [11] as

$$D = \frac{\lambda_{lc}}{2\sigma_n}, \tag{3.6}$$

with the overall noise contribution of the linear combination

$$\sigma_n = \sqrt{\sum_{m=1}^{M} \alpha_m^2 \sigma_{\phi_m}^2 + \sum_{m=1}^{M} \beta_m^2 \sigma_{\rho_m}^2}, \tag{3.7}$$

where σ_{ρ_m} are the code noises; and σ_{ϕ_m} is the phase noise, which can be assumed to be equal for the Galileo frequencies (E1, E5b, E5b, E6) due to their close vicinity.

The code noises σ_{ρ_m} are obtained from the Cramér Rao Bound (CRB) given by

$$\Gamma_m = \frac{c^2}{\frac{C}{N_0} \cdot \frac{\int (2\pi f)^2 |S_m(f)|^2 df}{\int |S_m(f)|^2 df}}, \tag{3.8}$$

where c is the speed of light; C/N_0 is the carrier to noise power ratio; and $S_m(f)$ is the power spectral density, which has been derived for binary offset carrier (BOC) modulated signals

Table 3.1: Cramér Rao Bounds for Galileo signals.

Frequency band	Signal	Bandwidth [MHz]	CRB [cm]
E1	CBOC(6,1,1/11)	20	11.14
E5 (E5a+E5b)	AltBOC(15,10)	51	1.95
E5a	BPSK(10)	20	7.83
E5b	BPSK(10)	20	7.83
E6	BOC(10,5)	40	2.41

by Betz in [13]. Table 3.1 shows the Cramér Rao Bounds at a carrier to noise power ratio $C/N_0 = 45\text{dB/Hz}$ for the wideband Galileo signals.

Two kinds of optimization criteria for this indicator can be done by using the remaining degrees of freedom of the linear combination (e.g. τ_{lc}, code weighting coefficients β_m), after fulfilling the constraints mentioned above. One optimization criterion is to maximize the combination discrimination D, which is then used to select the linear combination that minimizes the probability of wrong fixing over all linear combinations. The probability of wrong fixing computation will be discussed on Section 3.4. On the other hand, the other criterion is to minimize the noise variance σ_n^2. For both criteria, a numerical search over the integers j_m should be also included.

For simplicity, the time and user indices are omitted and the index lc is used instead; and the resulting code-carrier linear combination is written as

$$\begin{aligned}\Phi_{lc}^k = \lambda_{lc}\phi_{lc}^k &= r^k + T^k + \lambda_{lc}N_{lc}^k + \delta r^k \\ &\quad + c(\delta\tau - \delta\tau^k) + b_{\phi_{lc}} + b_{\phi_{lc}}^k + \varepsilon_{\phi_{lc}}^k, \end{aligned} \tag{3.9}$$

where λ_{lc} is the wavelength of the linear combination; and $b_{\phi_{lc}} = \sum_{m=1}^{M} \alpha_m b_{\phi_m} + \sum_{m=1}^{M} \beta_m b_{\rho_m}$. Note that the ionospheric delay is eliminated, and the obtained large wavelength λ_{lc} increases the reliability of ambiguity resolution.

Code-only linear combinations

The reliability of ambiguity resolution is further improved by an additional linear combination of the code measurements from Equation (2.3), referred as to code-only combination, which does not add further ambiguities. Figure 3.2 depicts the linear combination. The properties of the linear combination at M frequencies are regulated by a geometry-preserving and ionosphere-free constraints, as for the code-carrier linear combinations, but without the

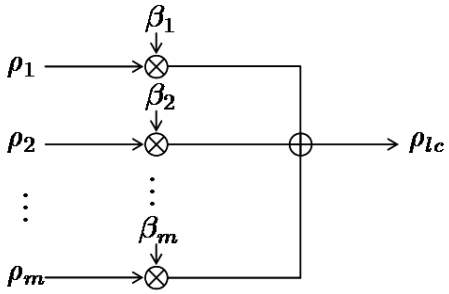

Figure 3.2: Code-only linear combination scheme.

carrier phase weighting coefficients. The corresponding constraints on the code weighting coefficients are then written as

Geometry-preserving (GP):

$$\sum_{m=1}^{M} b_m \stackrel{!}{=} 1, \tag{3.10}$$

Ionosphere-free (IF):

$$\sum_{m=1}^{M} b_m q_{1m}^2 \stackrel{!}{=} 0. \tag{3.11}$$

The code weighting coefficients b_m are represented in Roman letters in order to differentiate them from the corresponding code weighting coefficients of the code-carrier linear combination.

The noise variance of the code-only linear combination, which should be minimized as optimization criterion, is given by

$$\sigma_n^2 = \sum_{m=1}^{M} b_m^2 \sigma_{\rho_m}^2, \tag{3.12}$$

with the code noises σ_{ρ_m}, that can be also obtained as explained in the code-carrier linear combinations.

For simplicity, the time and user indices are omitted and the index lc is used instead; and the resulting code-only linear combination is written as

$$\rho_{lc}^k = r_{lc}^k + T_{lc}^k + \delta r_{lc}^k + c(\delta_{lc}\tau - \delta_{lc}\tau^k) + b_{\rho_{lc}} + b_{\rho_{lc}}^k + \varepsilon_{\rho_{lc}}^k, \tag{3.13}$$

where the ionospheric delay is also eliminated.

Carrier phase-only linear combinations

The design of the carrier phase-only combination follows the same constraints as for code-only combinations, i.e. the corresponding equations can be obtained by replacing the code weighting coefficients b_m of Equations (3.10) and (3.11) with the carrier phase weighting coefficients a_m. The integer preserving (NP) constraint can be also applied for the resulting ambiguities, but not necessarily.

The noise variance of the carrier phase-only linear combination, which should be minimized as optimization criterion, is given by

$$\sigma_n^2 = \sum_{m=1}^{M} a_m^2 \sigma_{\phi_m}^2, \tag{3.14}$$

with the phase noises σ_{ϕ_m}, that can be also obtained as explained in the code-carrier linear combinations.

This carrier-phase only combination can be useful to reduce the noise of the other linear combinations, as will be introduced on Section 3.1.3.

3.1.2 GP-IF-NP Four-frequency Galileo code-carrier combination

Given the code and carrier phase measurements from Equations (2.3) and (2.4), an ionosphere-free four-frequency Galileo (E1-E5a-E5b-E6) linear combination has been computed. Two different wavelengths with a noise level of a few centimeters were found: 4.469 m and 4.284 m. The analytic determination of this combination and comparison of its properties to other dual and triple frequency combinations is described below.

- **Analytic determination**

The properties of the linear combination are regulated by applying the geometry-preserving (GP), ionosphere-free (IF) and integer-preserving (NP) constraints from Equations (3.1) to (3.4) with $M = 4$ on the weighting coefficients.

In this case, the corresponding phase weighting coefficients can be rewritten to

$$\alpha_1 = \frac{j_1 \lambda_{lc}}{\lambda_1}, \qquad \alpha_2 = \frac{j_2 \lambda_{lc}}{\lambda_2}, \qquad \alpha_3 = \frac{j_3 \lambda_{lc}}{\lambda_3}, \qquad \alpha_4 = \frac{j_4 \lambda_{lc}}{\lambda_4}, \tag{3.15}$$

where λ_1 is the wavelength of the frequency E1; λ_2 is the wavelength of the frequency E5a; λ_3 is the wavelength of the frequency E5b;and λ_4 is the wavelength of the frequency E6.

The wavelength λ_{lc} of the combination will be obtained by replacing these coefficients in Equation (3.5). That is

$$\lambda_{lc} = \frac{\tau_{lc}}{\frac{j_1}{\lambda_1} + \frac{j_2}{\lambda_2} + \frac{j_3}{\lambda_3} + \frac{j_4}{\lambda_4}} = \tilde{\lambda}\tau \qquad \text{with} \qquad \tilde{\lambda} = \frac{1}{\frac{j_1}{\lambda_1} + \frac{j_2}{\lambda_2} + \frac{j_3}{\lambda_3} + \frac{j_4}{\lambda_4}}, \tag{3.16}$$

where $\tau_{lc} = \alpha_1 + \alpha_2 + \alpha_3 + \alpha_4$.

For this four frequency linear combination there exist 5 degrees of freedom: 4 for the code weights β_m and 1 for the wavelength λ_{lc}. The first two of them, β_1 and β_2, were required to fulfill the geometry-preserving (3.1) and ionosphere-free (3.2) constraints, and can be analytical derived as

$$\beta_1 = 1 - w_2 - (w_1 + 1)\tau_{lc} - (w_3 + 1)\beta_3 - (w_4 + 1)\beta_4, \tag{3.17}$$

$$\beta_2 = w_1\tau_{lc} + w_3\beta_3 + w_4\beta_4 + w_2, \tag{3.18}$$

with

$$w_1 = \tfrac{\tilde{k}+1}{q_{12}^2-1}, \quad w_2 = \tfrac{-1}{q_{12}^2-1}, \quad w_3 = \tfrac{1-q_{13}^2}{q_{12}^2-1}, \quad w_4 = \tfrac{1-q_{14}^2}{q_{12}^2-1} \quad \text{and} \quad \tilde{k} = \tilde{\lambda}\textstyle\sum_{m=1}^{4} \frac{j_m}{\lambda_m} q_{1m}^2,$$

where q_{1m} is the corresponding ratio of frequencies m = E5a, E5b and E6 with respect to the frequency E1.

The remaining degrees of freedom β_3, β_4 and τ_{lc} will be used to maximize the combination discrimination (see Equation 3.6), which is rewritten into

$$D = \frac{\lambda_{lc}}{2\sigma_n} = \frac{\lambda_{lc}}{2 \cdot \sqrt{\sigma_\phi^2(\alpha_1^2 + \alpha_2^2 + \alpha_3^2 + \alpha_4^2) + \beta_1^2\sigma_{\rho_1}^2 + \beta_2^2\sigma_{\rho_2}^2 + \beta_3^2\sigma_{\rho_3}^2 + \beta_4^2\sigma_{\rho_4}^2}}, \tag{3.19}$$

where the phase noise σ_ϕ will be assumed to 1 mm and 2 mm; and the code noises σ_{ρ_m} are obtained from the Cramér Rao Bounds (CRB) at a carrier to noise power ratio C/N_0 = 45dB/Hz from Table 3.1.

The optimization criterion includes a numerical search over the integers j_m which has been limited to $|j_m| \leq 5$ as all the other combinations suffer from biases and noise amplification. Moreover, the following optimization constraints are applied to the remaining degrees of freedom

$$\frac{\partial D^2(\beta_3, \beta_4, \tau_{lc})}{\partial \tau_{lc}} \stackrel{!}{=} 0, \qquad \frac{\partial D^2(\beta_3, \beta_4, \tau_{lc})}{\partial \beta_3} \stackrel{!}{=} 0 \qquad \text{and} \qquad \frac{\partial D^2(\beta_3, \beta_4, \tau_{lc})}{\partial \beta_4} \stackrel{!}{=} 0. \tag{3.20}$$

The results of the analytical derivation of the code weight β_3 and the carrier phase geometric weight τ_{lc} from Equation (3.20) are described as follows

$$\tau_{lc} = \frac{-(2c_1\beta_3^2 + 2c_2\beta_4^2 + 2c_5\beta_3\beta_4 + 2c_7\beta_3 + 2c_8\beta_4 + 2c_9)}{c_3\beta_3 + c_4\beta_4 + c_6}, \tag{3.21}$$

where

$$
\begin{aligned}
&c_1 = \sigma_{\rho_1}^2(w_3+1)^2 + \sigma_{\rho_2}^2 w_3^2 + \sigma_{\rho_3}^2, && c_2 = \sigma_{\rho_1}^2(w_4+1)^2 + \sigma_{\rho_2}^2 w_4^2 + \sigma_{\rho_4}^2,\\
&c_3 = 2(\sigma_{\rho_1}^2(w_1w_3 + w_1 + w_3 + 1) + \sigma_{\rho_2}^2 w_1w_3, && c_4 = 2(\sigma_{\rho_1}^2(w_1w_4 + w_1 + w_4 + 1) + \sigma_{\rho_2}^2 w_1w_4,\\
&c_5 = 2(\sigma_{\rho_1}^2(w_3w_4 + w_3 + w_4 + 1) + \sigma_{\rho_2}^2 w_3w_4, && c_6 = 2(\sigma_{\rho_1}^2(w_1w_2 - w_1 + w_2 - 1) + \sigma_{\rho_2}^2 w_1w_2,\\
&c_7 = 2(\sigma_{\rho_1}^2(w_2w_3 + w_2 - w_3 - 1) + \sigma_{\rho_2}^2 w_2w_3, && c_8 = 2(\sigma_{\rho_1}^2(w_2w_4 + w_2 - w_4 - 1) + \sigma_{\rho_2}^2 w_2w_4,\\
&c_9 = \sigma_{\rho_1}^2(1-w_2)^2 + \sigma_{\rho_2}^2 w_2^2;
\end{aligned}
$$

$$
\beta_3 = \frac{s_1\beta_4^2 - s_2\beta_4 + s_3}{s_4\beta_4 + s_5}, \tag{3.22}
$$

with the coefficients

$$
\begin{aligned}
&s_1 = c_4c_5 - 2c_2c_3, \quad s_2 = 2c_3c_8 - c_5c_6 - c_4c_7, \quad s_3 = c_6c_7 - 2c_3c_9,\\
&s_4 = c_3c_5 - 2c_1c_4, \quad s_5 = c_3c_7 - 2c_1c_6.
\end{aligned}
$$

The code weight β_4 is also analytically derived from Equation (3.20) as

$$
v_1\beta_4^3 + v_2\beta_4^2 + v_3\beta_4 + v_4 = 0, \tag{3.23}
$$

with the coefficients

$$
\begin{aligned}
v_1 &= s_1^2s_5 + r_3s_4^2 + s_1s_2s_4 + r_1s_1s_4,\\
v_2 &= 2r_3s_4s_5 + r_1s_1s_5 - s_1s_3s_4 - s_1s_2s_5 - r_1s_2s_4 - s_2^2s_4 - r_2s_4^2,\\
v_3 &= r_3s_5^2 + s_1s_3s_5 + r_1s_3s_4 + 2s_2s_3s_4 - 2r_2s_4s_5 - r_1s_2s_5,\\
v_4 &= s_3^2s_4 + r_2s_5^2 - r_1s_3s_5,
\end{aligned}
$$

where

$$
r_1 = 2c_4c_7 - c_5c_6 - c_3c_8, \qquad r_2 = c_6c_8 - 2c_4c_9, \qquad r_3 = c_4c_8 - 2c_2c_6.
$$

Table 3.2: Four-frequency code-carrier linear combinations ($\sigma_\phi = 1$ mm , $\sigma_{\rho_m} = \Gamma_m$).

		E1		E5a		E5b		E6		λ	σ_n	D
j_m	α_m	1	23.485	1	17.537	0	0.000	-2	-38.124	4.469m	6.34cm	35.3
	β_m		-0.047		-0.170		-0.162		-1.519			
j_m	α_m	4	2.284	-2	-0.853	-1	-0.437	0	0.000	10.87cm	2.48mm	21.9
	β_m		0.0002		0.0005		0.0005		0.0049			

The non-linear optimization can be obtained after solving for the non-linear equation of the code weight β_4, which can be solved analytically by using the Cardano's method (see

Appendix B). The resulting weighting coefficients and properties of the four frequency code-carrier linear combinations of maximum discrimination with a phase noise $\sigma_\phi = 1$ mm are shown in Table 3.2. The first combination refers to a widelane, while the second one to a narrowlane combination. The higher E1 code noise is significantly suppressed, which benefits by a larger wavelength of 4.469 m and a lower noise level of 6.34 cm.

Table 3.3: Four-frequency code-carrier linear combinations ($\sigma_\phi = 2$ mm , $\sigma_{\rho_m} = 3 \cdot \Gamma_m$).

		E1		E5a		E5b		E6		λ	σ_n	D
j_m	α_m	1	22.515	1	16.813	1	17.252	-3	-54.825	4.284m	13.7cm	15.6
	β_m		-0.018		-0.068		-0.064		-0.604			
j_m	α_m	4	2.284	-2	-0.853	-1	-0.437	0	0.000	10.87cm	4.97mm	10.9
	β_m		0.0002		0.0005		0.0005		0.0050			

Table 3.3 shows the resulting weighting coefficients and properties of the four-frequency code-carrier linear combinations of maximum discrimination with a phase noise $\sigma_\phi = 2$ mm and a Cramér Rao Bound scaled by a factor of three to include fast varying multipath. A different widelane combination is found with a large wavelength of 4.284 m and a noise level of 13.7 cm.

Table 3.4: GP-IF-NP code-carrier widelane combinations of maximum discrimination for two, three and four frequencies ($\sigma_\phi = 2$ mm, $\sigma_{\rho_m} = 3 \cdot \Gamma_m$).

		E1		E5		E5a		E5b		E6		λ	σ_n	D
j_m	α_m	1	17.263	-1	-13.059							3.285m	19.0cm	8.6
	β_m		-0.055		-3.148									
j_m	α_m	1	18.556			4	55.428	-5	-71.093			3.531m	34.0cm	5.2
	β_m		-0.234				-0.850		-0.807					
j_m	α_m	1	21.122	1	15.979					-2	-34.289	4.019m	11.9cm	16.9
	β_m		-0.020		-1.142						-0.649			
j_m	α_m	1	22.515			1	16.813	1	17.252	-3	-54.825	4.284m	13.7cm	15.6
	β_m		-0.018				-0.068		-0.064		-0.604			

The trade-off between the wavelength and the noise level for a limited numerical search over the integers j_m for four-frequency (E1-E5a-E5b-E6) widelane and narrowlane linear combinations is illustrated on Figure 3.3. The respective properties of the combinations that maximize the combination discrimination indicator are showed on Table 3.5.

The additional use of E6 measurements offers the advantage of using its lower code noise as the main noise contribution to the linear combination, which benefits by a larger wavelength an a lower noise level. This increases the combination discrimination by more than 50% in comparison to another optimized linear combinations with two and three Galileo frequencies. Table 3.4 depicts the weighting coefficients and properties of code-carrier widelane linear combinations of maximum discrimination for two, three and four Galileo frequencies (Henkel et al. [14]).

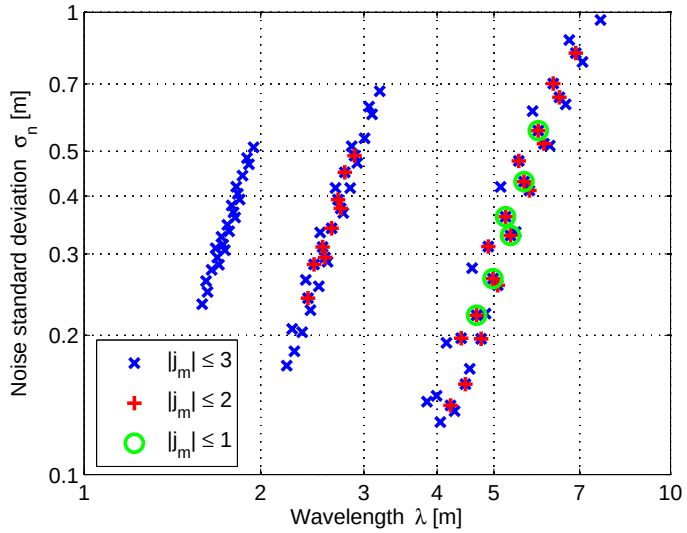

(a) Widelane

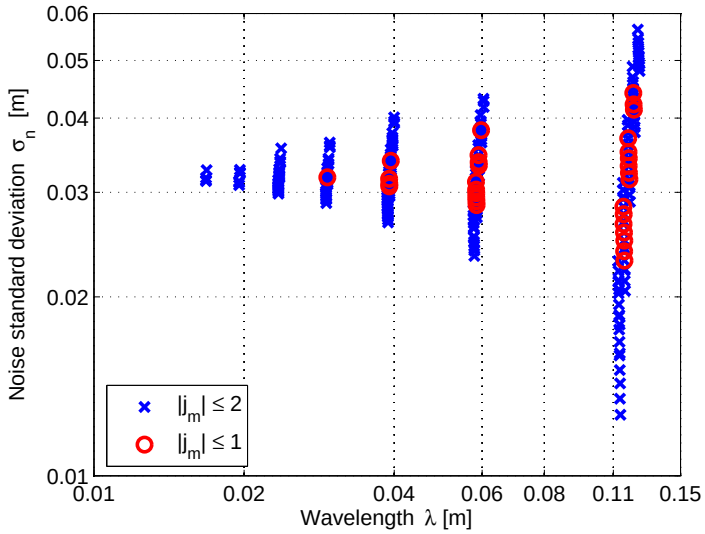

(b) Narrowlane

Figure 3.3: Four-frequency code-carrier linear combinations for a limited numerical search over the integers j_m. ($\sigma_\phi = 2$ mm, $\sigma_{\rho_m} = 3 \cdot \Gamma_m$)

Table 3.5: GP-IF-NP four-frequency code-carrier widelane and narrowlane combinations of maximum discrimination for a limited numerical search over the integers j_m. ($\sigma_\phi = 2$ mm, $\sigma_{\rho_m} = 3 \cdot \Gamma_m$)

		E1		E5a		E5b		E6		λ	σ_n	D
j_m	α_m	1	22.158	2	33.093	-1	-16.978	-2	-35.971	4.217m	14.1cm	14.9
	β_m		-0.032		-0.117		-0.111		-1.043			
j_m	α_m	1	24.542	1	18.326	-1	-18.805	-1	-19.920	4.670m	22.1cm	10.6
	β_m		-0.077		-0.282		-0.268		-2.517			
j_m	α_m	2	1.194	-2	-0.891	-1	-0.457	2	0.969	11.36cm	12.67mm	4.49
	β_m		0.0045		0.0166		0.0158		0.1486			
j_m	α_m	1	0.608	-1	-0.454	0	0.000	1	0.494	11.58cm	23.03mm	2.52
	β_m		0.0087		0.0315		0.0299		0.2816			

3.1.3 Carrier smoothing

The noise and multipath of the code-carrier and code-only combinations can be reduced by smoothing them with a carrier phase-only combination of minimum noise variance.

A non-recursive Hatch filter [15] variant introduced by Hwang et al. [16], which is illustrated on Figure 3.4, will be used to obtain the smoothed linear combination Ψ_{sm}. An ionosphere-free code-carrier combination of arbitrary wavelength or a code-only combination can be used as the noisy upper input Ψ_A, while an ionosphere-free carrier-phase-only combination is used as lower input Φ_B.

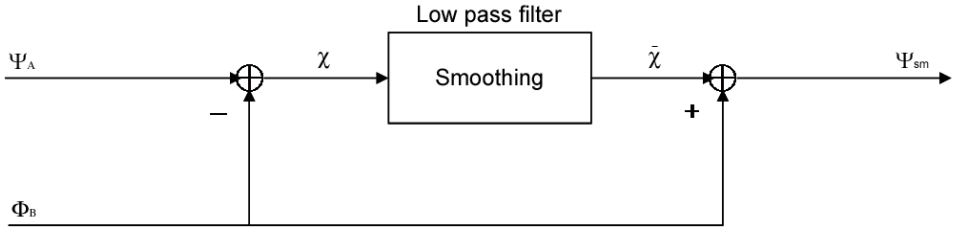

Figure 3.4: Carrier smoothing process.

The smoothed linear combination is written as

$$\Psi_{sm}(t) = \bar{\chi}(t) + \Phi_B(t), \tag{3.24}$$

with $\chi(t) = \Psi_A(t) - \Phi_B(t)$, which is filtered by a low pass filter, i.e.

$$\bar{\chi}(t) = \left(1 - \frac{1}{\tau}\right) \bar{\chi}(t-1) + \frac{1}{\tau}\chi(t). \tag{3.25}$$

The variance of the smoothed linear combination which can be derived by using the low pass filter equations and the geometric series $\sum_{n=0}^{\infty} q^n = 1/1-q$, is given by Henkel and Günther in [11] as

$$\sigma_{sm}^2 = \sigma_B^2 + \frac{1}{2\tau_s - 1} \cdot (\sigma_A^2 - 2\sigma_{AB} + \sigma_B^2) + \frac{2}{\tau_s} \cdot (\sigma_{AB} - \sigma_B^2), \tag{3.26}$$

where τ_s is the smoothing time constant; σ_B^2 is the variance of the carrier phase-only combination from Equation (3.14); σ_A^2 is the variance of the combination to be smoothed (e.g. code-carrier); and σ_{AB} is the covariance between both combinations.

Note that the use of carrier smoothing reduces the noise variance, which limits the margins for the biases, but having no impact on them; however, the main cost is the time needed for the desired accuracy. Also, the ambiguities of the carrier phase-only combination have no impact on the smoothed output as they are cancelled by the use of different signs in the addition.

3.1.4 Satellite-satellite single-difference (SD)

In order to eliminate the receiver biases and clock errors satellite-satellite single-difference (SD) measurements can be utilized. This simplifies the measurements and also improves their precision. For simplicity, the time indices are omitted, and the code and carrier phase satellite-satellite (kl) SD measurements obtained from Equations (2.3) and (2.4) are modeled as

$$\rho_{u,m}^{kl} = \rho_{u,m}^{k} - \rho_{u,m}^{l} = r_u^{kl} + T_u^{kl} + q_{1m}^2 I_u^{kl} + b_{\rho_{u,m}}^{kl} + \varepsilon_{\rho_{u,m}}^{kl}, \tag{3.27}$$

$$\Phi_{u,m}^{kl} = \Phi_{u,m}^{k} - \Phi_{u,m}^{l} = r_u^{kl} + T_u^{kl} - q_{1m}^2 I_u^{kl} + \lambda_m N_{u,m}^{kl} + \lambda_m b_{\phi_{u,m}}^{kl} + \varepsilon_{\phi_{u,m}}^{kl}, \tag{3.28}$$

where the corresponding SD clock offsets $c(\delta\tau^{kl})$ and the SD projected orbital errors δr_u^{kl} have been mapped respectively to the SD code biases $b_{\rho_{u,m}}^{kl}$ and SD phase biases $b_{\phi_{u,m}}^{kl}$.

3.2 Linear model for position estimation

The user-satellite range r_u^k obtained from the GNSS measurements can be expressed as a function of the satellite and the user positions as

$$r_u^k = ||\mathbf{x}^k - \mathbf{x}_u||, \tag{3.29}$$

where $\mathbf{x}^k = (x^k, y^k, z^k)^T$ is the satellite position vector; $\mathbf{x}_u = (x_u, y_u, z_u)^T$ is the user position vector; and $||\cdot||$ denotes the magnitude of a vector.

Given the code and carrier phase measurements, a linearization of them with respect to the user position can be done by using approximate values of all the parameters, that means a computed measurement is generated. For simplicity, it will be assumed that all the approximate values except for the user-satellite range are zero. Let $\mathbf{x}_0^k = (x_0^k, y_0^k, z_0^k)^T$ be the approximate satellite position and $\mathbf{x}_0 = (x_0, y_0, z_0)^T$ the approximate user position, then the corresponding range approximation is

$$r_0^k = ||\mathbf{x}_0^k - \mathbf{x}_0||, \tag{3.30}$$

and the resulting observed-minus-computed equations are given by

$$\delta\Phi_{u,m}^k = \Phi_{u,m}^k - r_0^k \qquad \text{and} \qquad \delta\rho_{u,m}^k = \rho_{u,m}^k - r_0^k. \tag{3.31}$$

Considering that the true position of the user can be represented as $\mathbf{x}_u = \mathbf{x}_0 + \delta\mathbf{x}$, with $\delta\mathbf{x}$ being a correction for the estimate, then the difference in the range can be linearized as follows

$$\begin{aligned} \delta r^k &= r_u^k - r_0^k \\ &= ||\mathbf{x}_0^k - \mathbf{x}_u|| - ||\mathbf{x}_0^k - \mathbf{x}_0|| \\ &= ||\mathbf{x}_0^k - \mathbf{x}_0 + \delta\mathbf{x}|| - ||\mathbf{x}_0^k - \mathbf{x}_0|| \\ &\approx -\frac{\mathbf{x}_0^k - \mathbf{x}_0}{||\mathbf{x}_0^k - \mathbf{x}_0||} \cdot \delta\mathbf{x} \quad = \quad -\mathbf{1}^k \cdot \delta\mathbf{x}, \end{aligned} \tag{3.32}$$

where $\mathbf{1}^k$ is the unit vector pointing from the user to the satellite and a Taylor series approximation have been used.

By substituting the linearized range on the observed-minus-computed equations gives the following linearized equations

$$\begin{aligned} \mathbf{y}_\rho = \delta\rho_{u,m}^k &= -\mathbf{1}^k \cdot \delta\mathbf{x} + T_u^k + q_{1m}^2 I_u^k + \delta r_u^k \\ &\quad + c(\delta\tau_u - \delta\tau^k) + b_{\rho_{u,m}} + b_{\rho_m}^k + \varepsilon_{\rho_{u,m}}^k, \end{aligned} \tag{3.33}$$

$$\begin{aligned} \mathbf{y}_\phi = \delta\Phi_{u,m}^k &= -\mathbf{1}^k \cdot \delta\mathbf{x} + T_u^k - q_{1m}^2 I_u^k + \lambda_m N_{u,m}^k + \delta r_u^k \\ &\quad + c(\delta\tau_u - \delta\tau^k) + b_{\phi_{u,m}} + b_{\phi_m}^k + \varepsilon_{\phi_{u,m}}^k. \end{aligned} \tag{3.34}$$

A GNSS mathematical model, also known as the *Gauss-Markov* model, can be obtained from the last linearized equations and is given in a general form as

$$E\{\mathbf{y}\} = \mathbf{A}\mathbf{x}; \qquad D\{\mathbf{y}\} = E\{\varepsilon\varepsilon^T\} = \mathbf{\Sigma}_y, \tag{3.35}$$

where $E\{\cdot\}$ is the expectation operator; $D\{\cdot\}$ is the dispersion operator; $\mathbf{y}$ is the vector of measurements; $\mathbf{A}$ is the design matrix; $\mathbf{x}$ is the vector of parameters; ε is the discrepancy between $\mathbf{y}$ and $\mathbf{Ax}$; and $\mathbf{\Sigma}_y$ is the noise covariance matrix of the measurements.

The first part of the model (*functional model*) describes the relation between the measurements and the parameters, while the second part (*stochastic model*) describes the noise characteristics of the measurements; therefore $\mathbf{\Sigma}_y$ is needed as weight of the measurements for the least-squares estimation of the unknown parameters, which will be discussed in the following section.

3.3 Integer estimation

The GNSS mathematical model from equation (3.35) can be parameterized in integers and real-values as

$$\mathbf{y} = \mathbf{A_1 N} + \mathbf{A_2 u} + \varepsilon, \qquad \mathbf{N} \in \mathbb{Z}^n, \quad \mathbf{u}, \varepsilon \in \mathbb{R}^n \tag{3.36}$$

where the vector $\mathbf{N}$ consists of the unknown integer ambiguities; the vector $\mathbf{u}$ consists of the remaining unknown parameters (e.g. user position, tropospheric delay); and ε is the noise vector.

A commonly used method to solve this model is the least-squares criterion, which looks for the estimates which minimizes the cost function

$$\mathcal{C}(\mathbf{N}, \mathbf{u}) = \left\|\mathbf{y} - \mathbf{A_1 N} - \mathbf{A_2 u}\right\|^2. \tag{3.37}$$

The cost function is the sum of the lengths of residuals squared, which would be directly to calculate if the integer constraint on each element of $\mathbf{N}$ were not considered. Hence, an *integer-least squares* problem arises, which can be solved by giving different weights to the residuals by using the inverse of the noise covariance matrix of the measurements $\mathbf{\Sigma}_y^{-1}$. It reads

$$\begin{aligned} \mathcal{C}_{\mathbf{\Sigma}_y^{-1}}(\mathbf{N}, \mathbf{u}) &= \left\|\mathbf{y} - \mathbf{A_1 N} - \mathbf{A_2 u}\right\|^2_{\mathbf{\Sigma}_y^{-1}} \\ &= (\mathbf{y} - \mathbf{A_1 N} - \mathbf{A_2 u})^T \mathbf{\Sigma}_y^{-1} (\mathbf{y} - \mathbf{A_1 N} - \mathbf{A_2 u}). \end{aligned} \tag{3.38}$$

The procedure to solve this minimization problem can be divided into three steps (Teunissen [1]) as follows:

1. *Float solution*: The integer constraint of the ambiguities $\mathbf{N}$ is disregarded (i.e. $\mathbf{N} \in \mathbb{R}^n$), and a float solution (denoted by a *hat* sign $\hat{\cdot}$) which minimizes the equation (3.38) is obtained.

The resulting real-valued estimates and their covariance matrix are written as

$$\begin{pmatrix} \hat{\mathbf{N}} \\ \hat{\mathbf{u}} \end{pmatrix}; \quad \boldsymbol{\Sigma}_{\mathbf{float}} = \begin{pmatrix} \boldsymbol{\Sigma}_{\hat{\mathbf{N}}} & \boldsymbol{\Sigma}_{\hat{\mathbf{N}},\hat{\mathbf{u}}} \\ \boldsymbol{\Sigma}_{\hat{\mathbf{u}},\hat{\mathbf{N}}} & \boldsymbol{\Sigma}_{\hat{\mathbf{u}}} \end{pmatrix}. \tag{3.39}$$

2. *Ambiguity resolution*: Given the float ambiguity vector $\hat{\mathbf{N}}$ from Equation (3.39) compute the integer ambiguity vector $\mathbf{N}$ which minimizes the cost function

$$\begin{aligned} \mathcal{C}(\mathbf{N}) &= \left\|\hat{\mathbf{N}} - \mathbf{N}\right\|^2_{\boldsymbol{\Sigma}^{-1}_{\hat{\mathbf{N}}}} \\ &= (\hat{\mathbf{N}} - \mathbf{N})^T \boldsymbol{\Sigma}^{-1}_{\hat{\mathbf{N}}} (\hat{\mathbf{N}} - \mathbf{N}). \end{aligned} \tag{3.40}$$

A *mapping* $\mathcal{S}$ from the space of reals to the space of integers is needed to obtain the integer solution (denoted by a *check* sign $\check{\cdot}$) to Equation (3.40), this means

$$\check{\mathbf{N}} = \mathcal{S}(\hat{\mathbf{N}}), \qquad \text{where} \quad \mathcal{S}\colon \mathbb{R}^n \to \mathbb{Z}^n. \tag{3.41}$$

Since the space of integers $\mathbb{Z}^n$ is discrete, the mapping will be a many-to-one map, this means that many real-valued ambiguity vectors $\mathbf{N}$ will be mapped to the same integer vector. Therefore, a subset $\mathcal{S}_z \subset \mathbb{R}^n$, also known as *pull-in region* by Teunissen [17] and Jonkman [18], can be assigned to each integer vector $\mathbf{z} \in \mathbb{Z}^n$ as follows

$$\mathcal{S}_z = \{x \in \mathbb{R}^n \big| \mathbf{z} = \mathcal{S}(x)\}, \qquad \mathbf{z} \in \mathbb{Z}^n. \tag{3.42}$$

Then, the integer estimator can be expressed as

$$\check{\mathbf{N}} = \sum_{z \in \mathbb{Z}^n} z s_z(\hat{N}), \qquad \text{with} \qquad s_z(x) = \begin{cases} 1 & \text{if } x \in \mathcal{S}_z \\ 0 & \text{otherwise} \end{cases} \tag{3.43}$$

where $s_z(x)$ is an indicator function.

Different integer estimators can be chosen for the mapping $\mathcal{S}$. A brief overview of them will be given on the following section.

3. *Fixed solution*: The integer ambiguity estimates are used to correct the float estimates of the remaining parameters $\hat{\mathbf{u}}$, it reads

$$\hat{\mathbf{u}}(\check{\mathbf{N}}) = \hat{\mathbf{u}} - \boldsymbol{\Sigma}_{\hat{\mathbf{u}},\hat{\mathbf{N}}} \boldsymbol{\Sigma}^{-1}_{\hat{\mathbf{N}}} (\hat{\mathbf{N}} - \check{\mathbf{N}}) = \check{\mathbf{u}}. \tag{3.44}$$

3.3.1 Integer estimators

The float ambiguity solution $\hat{\mathbf{N}}$ from Equation (3.39) can be represented as a vector of estimates with the corresponding covariance matrix as

$$\hat{\mathbf{N}} = \begin{pmatrix} \hat{N}_1 \\ \hat{N}_2 \\ \vdots \\ \hat{N}_n \end{pmatrix}, \qquad \boldsymbol{\Sigma}_{\hat{\mathbf{N}}} = \begin{pmatrix} \sigma^2_{\hat{N}_1} & \sigma^2_{\hat{N}_1\hat{N}_2} & \cdots & \sigma^2_{\hat{N}_1\hat{N}_n} \\ \sigma^2_{\hat{N}_2\hat{N}_1} & \sigma^2_{\hat{N}_2} & \cdots & \sigma^2_{\hat{N}_2\hat{N}_n} \\ \vdots & \vdots & \ddots & \vdots \\ \sigma^2_{\hat{N}_n\hat{N}_1} & \sigma^2_{\hat{N}_n\hat{N}_2} & \cdots & \sigma^2_{\hat{N}_n} \end{pmatrix}. \tag{3.45}$$

This notation of the float ambiguity solution will be used to describe the following integer estimators.

Integer Rounding

Integer rounding is the simplest integer estimator. The integer solution is obtained by *rounding* each of the entries of the float solution $\hat{\mathbf{N}}$ to their nearest integer. The corresponding integer estimation procedure is written then as

$$\check{\mathbf{N}}_R = \begin{pmatrix} [\hat{N}_1] \\ [\hat{N}_2] \\ \vdots \\ [\hat{N}_n] \end{pmatrix}, \tag{3.46}$$

where $[\cdot]$ denotes rounding to the nearest integer.

This estimator does not take the ambiguity correlation into account; therefore, the solution will *not always* satisfy the cost function formulated in Equation (3.40), unless the ambiguity covariance matrix $\boldsymbol{\Sigma}_{\hat{\mathbf{N}}}$ were a *diagonal* matrix (i.e. there is no correlation between the ambiguities).

Integer Bootstrapping

In contrast to integer rounding, the integer bootstrapping (Blewitt [19]) estimator takes some of the correlation between the ambiguities into account. It is also knows as *sequential integer rounding*, because the integer solution is computed as follows: the first ambiguity $\hat{N}_1$ is rounded to its nearest integer. After this, the estimates of the remaining ambiguities are corrected by virtue of their correlation with the first ambiguity. Then the second (corrected)

ambiguity is rounded to its nearest integer, and the remaining estimates are then now corrected by their correlation with this second ambiguity, and so on. The algorithm is given as

$$\check{\mathbf{N}}_B = \begin{pmatrix} [\hat{N}_1] \\ [\hat{N}_{2|1}] \\ \vdots \\ [\hat{N}_{n|N}] \end{pmatrix} = \begin{pmatrix} [\hat{N}_1] \\ [\hat{N}_2 - \sigma_{\hat{N}_2\hat{N}_1}\sigma^{-2}_{\hat{N}_1}(\hat{N}_1 - [\hat{N}_1])] \\ \vdots \\ [\hat{N}_n - \sum_{i=1}^{n-1}\sigma_{\hat{N}_n\hat{N}_{i|I}}\sigma^{-2}_{\hat{N}_{i|I}}(\hat{N}_{i|I} - [\hat{N}_{i|I}])] \end{pmatrix}, \tag{3.47}$$

where $\hat{N}_{i|I}$ stands for the ith least-squares ambiguity obtained through a conditioning on the previous $I = 1, ..., (i-1)$ sequentially rounded ambiguities.

The real-valued sequential least-squares solution can be obtained by the triangular decomposition of the covariance matrix of the ambiguities as follows

$$\boldsymbol{\Sigma}_{\hat{\mathbf{N}}} = \mathbf{L}^T\mathbf{D}\mathbf{L}, \tag{3.48}$$

with the diagonal matrix $\mathbf{D}$, with the conditional variances as its entries, and the unit lower triangular matrix $\mathbf{L}$, which have the following structure

$$\mathbf{D} = \text{diag}(\sigma^2_{\hat{N}_1}, \sigma^2_{\hat{N}_{2|1}}, ..., \sigma^2_{\hat{N}_{n|I}}), \tag{3.49}$$

$$\mathbf{L} = \begin{pmatrix} 1 & & & \\ \sigma_{\hat{N}_2\hat{N}_1}\sigma^{-2}_{\hat{N}_1} & 1 & & \\ \vdots & \ddots & \ddots & \\ \sigma_{\hat{N}_n\hat{N}_1}\sigma^{-2}_{\hat{N}_1} & \dots & \sigma_{\hat{N}_n\hat{N}_1}\sigma^{-2}_{\hat{N}_{n-1|1,...,n-2}} & 1 \end{pmatrix}. \tag{3.50}$$

Note that the integer solution depends on with which ambiguity is started and on the order of the ambiguities.

Integer least-squares (ILS) estimator

The integer least-squares estimator takes all the correlation between the ambiguities into account due to the use of the covariance matrix $\boldsymbol{\Sigma}_{\hat{\mathbf{N}}}$, and therefore, it really focuses to solve the cost function from (3.40), which can be rewritten into

$$\check{\mathbf{N}}_{LS} = \min_{\mathbf{z}\in\mathbb{Z}^n} \left\|\hat{\mathbf{N}} - \mathbf{z}\right\|^2_{\boldsymbol{\Sigma}^{-1}_{\hat{\mathbf{N}}}}, \tag{3.51}$$

where $\check{\mathbf{N}}_{LS}$ is the integer least-squares solution, which has the shortest distance to the float solution, in terms of the covariance matrix $\boldsymbol{\Sigma}_{\hat{\mathbf{N}}}$. In order to obtain this solution an integer search is needed. The *Least-squares AMBiguity Decorrelation Adjustment* (LAMBDA)

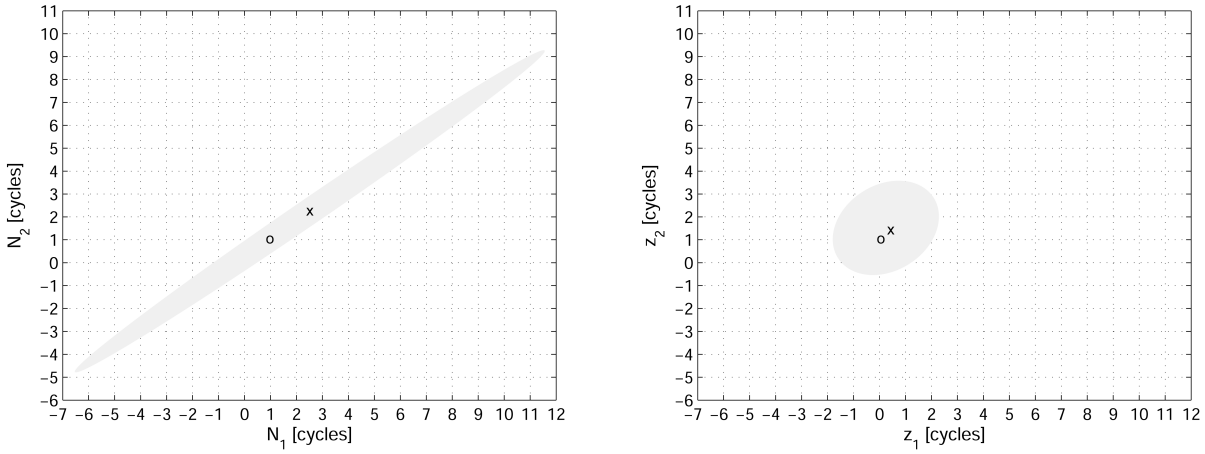

(a) (b)

Figure 3.5: 2D Ambiguity search space before (a) and after the ambiguity decorrelation (b).

method [1] provides the integer least-square solution for a sufficiently large search space volume.

• **LAMBDA method**

The search space is defined as

$$\Omega_{\mathbf{N}} = (\hat{\mathbf{N}} - \mathbf{N})^T \boldsymbol{\Sigma}_{\hat{\mathbf{N}}}^{-1} (\hat{\mathbf{N}} - \mathbf{N}) \leq \chi^2, \qquad \mathbf{N} \in \mathbb{Z}^n, \tag{3.52}$$

where χ^2 is a positive constant to be chosen which determines the size of the search space. The search space is an ellipsoid centered at $\hat{\mathbf{N}}$, and its shape is governed by the covariance matrix $\boldsymbol{\Sigma}_{\hat{\mathbf{N}}}$. It is usually extremely elongated due to the high correlation between the ambiguities, hence the computational efficiency of the search for the integer solution is highly affected. Therefore, the aim is to decorrelate the original float ambiguity solution before the search procedure starts. Figure 3.5 illustrates the 2D ambiguity search space (Odijk [20]) before and after the ambiguity decorrelation transformation, where the ambiguity float solution and the integer solution are marked with a cross and a circle, respectively. The ambiguity decorrelation is done by using the following transformation

$$\hat{\mathbf{z}} = \mathbf{Z}^T \hat{\mathbf{N}}, \qquad \boldsymbol{\Sigma}_{\hat{\mathbf{z}}} = \mathbf{Z}^T \boldsymbol{\Sigma}_{\hat{\mathbf{N}}} \mathbf{Z}. \tag{3.53}$$

This transformation $\mathbf{Z}$ must satisfy the following conditions to be admissible: $\mathbf{Z}$ and its inverse $\mathbf{Z}^{-1}$ must have integer entries and must be volume-preserving transformations (i.e.

$|\det\mathbf{Z}| = 1$), so that the integer nature of the ambiguities is preserved in both spaces. The transformed search space is then given by

$$\Omega_{\mathbf{z}} = (\hat{\mathbf{z}} - \mathbf{z})^T \boldsymbol{\Sigma}_{\hat{\mathbf{z}}}^{-1} (\hat{\mathbf{z}} - \mathbf{z}) \leq \chi^2, \qquad \mathbf{z} \in \mathbb{Z}^n, \tag{3.54}$$

where, by using the $\mathbf{L}^T\mathbf{D}\mathbf{L}$ decomposition of $\boldsymbol{\Sigma}_{\hat{\mathbf{z}}}$, the left-hand side of the quadratic inequality can be written as a sum-of-squares

$$\sum_{i=1}^{n} \frac{(\hat{\mathbf{z}}_{i|I} - \mathbf{z}_i)^2}{\sigma_{i|I}^2} \leq \chi^2, \tag{3.55}$$

with the conditional variances $\sigma_{i|I}^2$ obtained from the matrix D; and the conditional least-square estimator $\hat{\mathbf{z}}_{i|I}$.

In order to make the search more efficient, the choice of χ^2 should be chosen, such that the search space contains at least one integer. This can be done by using the integer bootstrapped solution, because it is a good approximation of the ILS estimator. Then the size of the search space is

$$\chi^2 = (\hat{\mathbf{z}} - \check{\mathbf{z}}_B)^T \boldsymbol{\Sigma}_{\hat{\mathbf{z}}}^{-1} (\hat{\mathbf{z}} - \check{\mathbf{z}}_B) \tag{3.56}$$

By using Equation (3.55), the n intervals used for the search of the integer candidates are bounded as follows

$$\begin{aligned}
(\hat{z}_1 - z_1)^2 &\leq \sigma_1^2 \chi^2 \\
(\hat{z}_{2|1} - z_2)^2 &\leq \sigma_{2|1}^2 \left(\chi^2 - \frac{(\hat{z}_1 - z_1)^2}{\sigma_1^2} \right) \\
&\vdots \\
(\hat{z}_{n|N} - z_n)^2 &\leq \sigma_{n|N}^2 \left(\chi^2 - \sum_{i=1}^{n} \frac{(\hat{z}_{i|I} - z_i)^2}{\sigma_{i|I}^2} \right)
\end{aligned}$$

This search based on the decorrelated ambiguities also results in a minimization of the cost function from (3.40)

$$\begin{aligned}
(\hat{\mathbf{z}} - \mathbf{z})^T \boldsymbol{\Sigma}_{\hat{\mathbf{z}}}^{-1} (\hat{\mathbf{z}} - \mathbf{z}) &= (\hat{\mathbf{N}} - \mathbf{N})^T \mathbf{Z} \boldsymbol{\Sigma}_{\hat{\mathbf{z}}}^{-1} \mathbf{Z}^T (\hat{\mathbf{N}} - \mathbf{N}) \\
&= (\hat{\mathbf{N}} - \mathbf{N})^T \mathbf{Z} (\mathbf{Z}^T \boldsymbol{\Sigma}_{\hat{\mathbf{N}}} \mathbf{Z})^{-1} \mathbf{Z}^T (\hat{\mathbf{N}} - \mathbf{N}) \\
&= (\hat{\mathbf{N}} - \mathbf{N})^T \boldsymbol{\Sigma}_{\hat{\mathbf{N}}}^{-1} (\hat{\mathbf{N}} - \mathbf{N}).
\end{aligned} \tag{3.57}$$

The obtained solution $\check{\mathbf{z}}$ can be back-transformed to the original domain by applying the inverse Z-transformation as follows

$$\check{\mathbf{N}} = \mathbf{Z}^{-T} \check{\mathbf{z}}. \tag{3.58}$$

3.4 Quality of ambiguity estimates

The probability of correct integer estimation, referred also as to *success rate*, is an important measure of the reliability of the ambiguity resolution. This probability depends on the functional and stochastic model, and the chosen method of integer estimation. In order to calculate it, the distribution functions of the ambiguity estimators are needed. Therefore, a brief description of how to obtain this distribution functions is given below.

If the noise vector ε from Equation (3.36) is assumed to be normally distributed with zero mean and covariance matrix $\mathbf{\Sigma}_y$, i.e. $\varepsilon \sim \mathcal{N}(0, \mathbf{\Sigma}_y)$; then the float ambiguities are also normally distributed with mean $\mathbf{N}$ and covariance matrix $\mathbf{\Sigma}_{\hat{\mathbf{N}}}$. It reads

$$\hat{\mathbf{N}} \sim \mathcal{N}(\mathbf{N}, \mathbf{\Sigma}_{\hat{\mathbf{N}}}), \qquad \mathbf{N} \in \mathbb{Z}^n. \tag{3.59}$$

Then, the probability density function (PDF) of the float ambiguities $\hat{\mathbf{N}}$ is

$$f_{\hat{\mathbf{N}}}(x) = \frac{1}{\sqrt{|\mathbf{\Sigma}_{\hat{\mathbf{N}}}|}(2\pi)^{\frac{1}{2}n}} \exp\{-\frac{1}{2}\|x - \mathbf{N}\|^2_{\mathbf{\Sigma}_{\hat{\mathbf{N}}}}\}, \tag{3.60}$$

where $|\cdot|$ denotes the determinant operator.

The joint PDF of the float and fixed ambiguities is given by

$$f_{\hat{\mathbf{N}}\check{\mathbf{N}}}(x, z) = f_{\hat{\mathbf{N}}}(x) s_z x, \qquad x \in \mathbb{R}^n, \quad z \in \mathbb{Z}^n, \tag{3.61}$$

where $s_z(x)$ is the indicator function of Equation (3.43).(See Teunissen [21] for the proof). By integration of this function over x and z the marginal distributions of $\hat{\mathbf{N}}$ and $\check{\mathbf{N}}$ can be obtained, which results in the following probability mass function (PMF) of the fixed ambiguities

$$P(\check{\mathbf{N}} = z) = \int_{\mathbb{R}^n} f_{\hat{\mathbf{N}}\check{\mathbf{N}}}(x, z)dx = \int_{\mathcal{S}_z} f_{\hat{\mathbf{N}}}(x)dx. \tag{3.62}$$

• Success rate and probability of wrong fixing

The success rate P_s can be then obtained from Equation (3.62) as

$$P_s = P(\check{\mathbf{N}} = \mathbf{N}) = \int_{\mathcal{S}_N} f_{\hat{\mathbf{N}}}(x)dx. \tag{3.63}$$

If the success rate is sufficiently close to one the integer ambiguity solution can be considered deterministic, this means that the uncertainty in the integer ambiguity solution can be safely neglected. On the other hand, incorrect estimates can be obtained due to very low success rates leading to unacceptable errors in the positioning results.

Note that the reliability of the ambiguity resolution can also be given in terms of the *probability of incorrect or wrong fixing* P_w, which can be given by

$$P_w = P(\check{\mathbf{N}} \neq \mathbf{N}) = 1 - P_s. \tag{3.64}$$

The corresponding success rate of each estimator can be obtained by evaluating Equation (3.63) for each one. Unfortunately, this evaluation is very complicated for the integer least-squares estimator because of the complex integration region, and for the vectorial case of the integer rounding estimator when the ambiguity covariance matrix is non-diagonal, which in practice is the case (Teunissen [22]). However, an exact and easy-to-compute evaluation of the success rate for the integer bootstrapping estimator can be possible. Therefore, it can be used as approximation or bound for the other estimators.

3.4.1 Success rate of the bootstrapped estimator

The bootstrapped success rate is given as

$$\begin{aligned} P_{s_B} = P(\check{\mathbf{N}}_B = \mathbf{N}) &= P(\bigcap_{i=1}^{n}\{\left|\hat{N}_{i|I} - N_i\right| \leq \frac{1}{2}\}) \qquad (3.65)\\ &= \prod_{i=1}^{n} P([\hat{N}_{i|I}] = N_i \Big| [\hat{N}_1] = N_1, ..., [\hat{N}_{i-1|I-1}] = N_{i-1}) \\ &= \prod_{i=1}^{n} \int_{-\frac{1}{2}}^{\frac{1}{2}} \frac{1}{\sigma_{i|I}\sqrt{2\pi}} \exp\{-\frac{1}{2}\left(\frac{x}{\sigma_{i|I}}\right)^2\} dx \\ &= \prod_{i=1}^{n} \left(2\Phi\left(\frac{1}{2\sigma_{i|I}}\right) - 1\right), \qquad (3.66) \end{aligned}$$

with the standard deviation of the ith least-squares ambiguity conditioned on the previous $I = \{1, ..., i-1\}$ ambiguities $\sigma_{i|I}$; and the cumulative normal distribution

$$\Phi(x) = \int_{-\infty}^{x} \frac{1}{\sqrt{2\pi}} \exp\{-\frac{1}{2}v^2\} dv. \tag{3.67}$$

Note that the chain rule of conditional probabilities have been applied to Equation (3.65), and the conditional standard deviations are equal to the square root of the entries of the matrix $\mathbf{D}$ from the triangular decomposition $\mathbf{L}^T\mathbf{D}\mathbf{L}$ of the covariance matrix $\mathbf{\Sigma}_{\hat{\mathbf{N}}}$.

3.4.2 Success rate bounds

The success rate of the bootstrapped estimator can be used as *upper bound* for the success rate of the rounding estimator as

$$P(\check{\mathbf{N}}_R = \mathbf{N}) \leq P(\check{\mathbf{N}}_B = \mathbf{N}). \tag{3.68}$$

Furthermore, it can also be used as *lower bound* for the ILS success rate, if the bootstrapped success rate from Equation (3.66) is computed for the decorrelated ambiguities $\hat{\mathbf{z}}$ and the corresponding conditional standard deviations.

$$P_{s_{LS}} = P(\check{\mathbf{N}}_{LS} = \mathbf{N}) \geq \prod_{i=1}^{n} \left(2\Phi \left(\frac{1}{2\sigma_{i|I}} \right) - 1 \right), \tag{3.69}$$

where $\sigma_{i|I}$ are equal to the square root of the entries of the matrix $\mathbf{D}$ from the triangular decomposition $\mathbf{L}^T\mathbf{D}\mathbf{L}$ of the covariance matrix $\mathbf{\Sigma}_{\hat{\mathbf{z}}}$.

• Invariant upper bound

The *Ambiguity Dilution of Precision* (ADOP) measure (units of cycles), introduced by Teunissen in [23], is invariant for the class of ambiguities transformations and approximates the average precision of the ambiguities. This means that it is independent of which parameterization is used. It is defined as

$$ADOP = \sqrt{|\mathbf{\Sigma}_{\hat{\mathbf{N}}}|}^{\frac{1}{n}}. \tag{3.70}$$

An *upper bound* for the bootstrapped success rate can be then given based on the ADOP as

$$P_{s_B} \leq \left(2\Phi \left(\frac{1}{2 \cdot ADOP} \right) - 1 \right)^n, \tag{3.71}$$

where n is the number of ambiguities to be resolved.

Chapter 4

Integer ambiguity resolution in the presence of biases

Usually, errors on the GNSS measurements (e.g. multipath, satellite clock offsets) can *not* be successfully corrected or modeled resulting in a measurement bias. These biases will lower the success rate and thus degrade the performance of ambiguity resolution. Therefore, it would be interesting to know the impact that biases have on this performance. On the following section, a measure for this impact, referred to as *bias-affected bootstrapped success rate*, will be discussed. Thereafter, a model for absolute carrier phase positioning in the presence of biases with satellite-satellite single difference measurements will be introduced on Section 4.2. For the ambiguity resolution of this model, the LAMBDA method does not achieve the integer least-squares solution, because the biases are amplified due to the integer decorrelation transformation. In Section 4.4, a method to approximate the magnitude and sign of the measurement biases is discussed. A partial integer decorrelation suggested for the LAMBDA method is discussed in Section 4.5. Moreover, a sequential fixing using the bootstrapping estimator with or without the partial integer decorrelation is also suggested. Finally, partial ambiguity fixing for severe multipath or large uncorrected biases will be introduced on Section 4.6.

4.1 Biased-affected bootstrapped success rate

In the presence of uncorrected biases, the float ambiguity solution is assumed to be biased and normally distributed as follows

$$\hat{\mathbf{N}} \sim \mathcal{N}(\mathbf{N} + \mathbf{b}_{\hat{\mathbf{N}}}, \mathbf{\Sigma}_{\hat{\mathbf{N}}}), \qquad \mathbf{N} \in \mathbb{Z}^n, \quad \mathbf{b}_{\hat{\mathbf{N}}} \in \mathbb{R}^n, \tag{4.1}$$

where $\mathbf{b}_{\hat{\mathbf{N}}}$ denotes the real-valued bias vector.

The reduction of the success rate due to biases in the float solution increases with the size of the bias along a fixed direction. However, this reduction could be very large or it could be so small, that the success rate can still be sufficiently high. Hence, it is important to be able to evaluate the success rate in the presence of biases. An exact and easy-to-compute evaluation of this *biased-affected* success rate can be only possible for the bootstrapped estimator.

The biased-affected bootstrapped success rate has been derived by Teunissen in [24] as

$$P_{s_B,bias} = P_{bias}(\check{\mathbf{N}}_B = \mathbf{N}) = \prod_{i=1}^{n} \left(\Phi\left(\frac{1 - 2b_{\hat{N}_{i|I}}}{2\sigma_{\hat{N}_{i|I}}} \right) + \Phi\left(\frac{1 + 2b_{\hat{N}_{i|I}}}{2\sigma_{\hat{N}_{i|I}}} \right) - 1 \right), \tag{4.2}$$

where $b_{\hat{N}_{i|I}}$ is the ith entry of the conditional bias vector $\mathbf{b}_{\hat{N}_{i|I}} = \mathbf{L}^{-1}\mathbf{b}_{\hat{\mathbf{N}}}$, with the unit lower triangular matrix $\mathbf{L}$ from the factorization $\mathbf{\Sigma}_{\hat{\mathbf{N}}} = \mathbf{L}^T\mathbf{D}\mathbf{L}$; $\sigma_{\hat{N}_{i|I}}$ the standard deviation of the ith least-squares ambiguity conditioned on the previous $I = \{1, ..., i-1\}$ ambiguities; and $\Phi(x)$ is the cumulative normal distribution given in Equation (3.67).

This bias-affected success rate can also be evaluated for the decorrelated ambiguity vector $\hat{\mathbf{z}} = \mathbf{Z}^T\hat{\mathbf{N}}$ of the LAMBDA method. But when the original ambiguities are biased, the transformed ambiguities will also be biased. This reads

$$\hat{\mathbf{z}} \sim \mathcal{N}(\mathbf{z} + \mathbf{Z}^T\mathbf{b}_{\hat{\mathbf{N}}}, \mathbf{Z}^T\mathbf{\Sigma}_{\hat{\mathbf{N}}}\mathbf{Z}), \tag{4.3}$$

where $\mathbf{Z}^T\mathbf{b}_{\hat{\mathbf{N}}}$ is the transformed bias vector.

In this case, the factorization $\mathbf{\Sigma}_{\hat{\mathbf{z}}} = \mathbf{L}^T\mathbf{D}\mathbf{L}$ is applied, and the corresponding conditional bias vector $\mathbf{b}_{\hat{N}_{i|I}} = \mathbf{L}^{-1}\mathbf{Z}^T\mathbf{b}_{\hat{\mathbf{N}}}$ and the conditional standard deviations $\sigma_{\hat{z}_{i|I}}$ should be replaced in Equation (4.2) to obtain the bias-affected success rate $P_{bias}(\check{\mathbf{z}}_B = \mathbf{z})$.

4.2 Absolute carrier phase positioning model

Given the bias-affected success rate to measure the impact biases have on ambiguity resolution, the linear positioning model to be used for this study will be derived as follows.

• Use of code-carrier and code-only linear combinations

A dual frequency (E1-E5) GP-IF-NP code-carrier linear combination of maximum discrimination is applied to the code and carrier phase measurements in order to increase the robustness of ambiguity resolution. Furthermore, an additional dual frequency (E1-E5) GP-IF

code-only linear combination, which is uncorrelated with respect to the previous code-carrier combination, is also used to improve the ambiguity resolution. This code-carrier combination benefits from a wavelength of 3.285 m with a lower noise level (see Section 3.1.1, Table 3.4). The covariance matrix of both combinations is given by

$$\mathbf{\Sigma}_{LC} = \begin{pmatrix} \sigma_{n_1}^2 & \sigma_{n_1 n_2} \\ \sigma_{n_1 n_2} & \sigma_{n_2}^2 \end{pmatrix}, \tag{4.4}$$

with the noise variances of the code-carrier and code-only linear combinations

$$\sigma_{n_1}^2 = \sum_{m=1}^{M} \alpha_m^2 \sigma_\phi^2 + \beta_m^2 \sigma_{\rho_m}^2, \qquad \sigma_{n_2}^2 = \sum_{m=1}^{M} b_m^2 \sigma_{\rho_m}^2,$$

and the cross-correlation

$$\sigma_{n_1 n_2} = \sum_{m=1}^{M} \beta_m b_m \sigma_{\rho_m}^2,$$

which equals zero in the case of the code-carrier of maximum combination discrimination and the code-only of minimum noise variance combinations.

• Use of carrier smoothing

Carrier smoothing is applied to both linear combinations in order to reduce their noise variance. Therefore, the smoothed covariance matrix of both combinations is obtained from Equation 3.26 and is given by

$$\mathbf{\Sigma}_{LC_{sm}} = \begin{pmatrix} \sigma_{n_1 sm}^2 & \sigma_{n_1 n_2 sm} \\ \sigma_{n_1 n_2 sm} & \sigma_{n_2 sm}^2 \end{pmatrix}, \tag{4.5}$$

with

$$\begin{aligned}
\sigma_{n_1 sm}^2 &= \sigma_B^2 + \frac{1}{2\tau_s - 1} \cdot (\sigma_{n_1}^2 - 2\sigma_{n_1 B} + \sigma_B^2) + \frac{2}{\tau_s} \cdot (\sigma_{n_1 B} - \sigma_B^2), \\
\sigma_{n_2 sm}^2 &= \sigma_B^2 + \frac{1}{2\tau_s - 1} \cdot (\sigma_{n_2}^2 + \sigma_B^2) + \frac{2}{\tau_s} \cdot (-\sigma_B^2), \\
\sigma_{n_1 n_2 sm}^2 &= \sigma_B^2 + \frac{1}{2\tau_s - 1} \cdot (\sigma_{n_1 n_2}^2 - \sigma_{n_1 B} + \sigma_B^2) + \frac{1}{\tau_s} \cdot (\sigma_{n_1 B} - 2\sigma_B^2).
\end{aligned}$$

• Use of satellite-satellite SD with linear combinations

Satellite-satellite single difference is used with the code-carrier and code-only combinations. In this case, the corresponding equations for the SD linear combinations are given by

$$\Phi_{lc_1}^{kl} = \Phi_{lc_1}^{k} - \Phi_{lc_1}^{l} = r_{lc_1}^{kl} + T_{lc_1}^{kl} + \lambda_{lc_1} N_{lc_1}^{kl} + \lambda_{lc_1} b_{\phi_{lc_1}}^{kl} + \varepsilon_{\phi_{lc_1}}^{kl}, \tag{4.6}$$

$$\rho_{lc_2}^{kl} = \rho_{lc_2}^{k} - \rho_{lc_2}^{l} = r_{lc_2}^{kl} + T_{lc_2}^{kl} + b_{\rho_{lc_2}}^{kl} + \varepsilon_{\rho_{lc_2}}^{kl}, \tag{4.7}$$

where the indices lc_1 and lc_2 correspond to the code-carrier combination and the code-only combination, respectively.

The single-differences (SD) introduce a correlation which can be derived as follows

$$\Phi_{SD} = \begin{pmatrix} \Phi^{12} \\ \Phi^{13} \\ \Phi^{14} \\ \vdots \\ \Phi^{1K} \end{pmatrix} = \begin{pmatrix} \Phi^1 - \Phi^2 \\ \Phi^1 - \Phi^3 \\ \Phi^1 - \Phi^4 \\ \vdots \\ \Phi^1 - \Phi^K \end{pmatrix} = \underbrace{\begin{pmatrix} 1 & -1 & 0 & 0 & 0 & 0 \\ 1 & 0 & -1 & 0 & 0 & 0 \\ 1 & 0 & 0 & -1 & 0 & 0 \\ \vdots & 0 & 0 & 0 & \ddots & 0 \\ 1 & 0 & 0 & 0 & 0 & -1 \end{pmatrix}}_{\mathbf{C}_{base}} \cdot \underbrace{\begin{pmatrix} \Phi^1 \\ \Phi^2 \\ \Phi^3 \\ \Phi^4 \\ \vdots \\ \Phi^K \end{pmatrix}}_{\Phi}, \tag{4.8}$$

where, for simplicity, the first satellite has been taken as the reference satellite; and $\mathbf{C}_{base}$ is the design matrix for the single-differences. The correlation from the single-differences can be then given as

$$\mathbf{C}_{SD} = E\{\Phi_{SD}\Phi_{SD}^T\} = \mathbf{C}_{base} \cdot E\{\Phi\Phi^T\} \cdot \mathbf{C}_{base}^T, \tag{4.9}$$

where $E\{\Phi\Phi^T\} = \sigma_n^2 \cdot \mathbf{1}$, because of their full correlation. Therefore,

$$\begin{aligned} \mathbf{C}_{SD} &= \sigma_n^2 \cdot \mathbf{C}_{base} \cdot \mathbf{C}_{base}^T \\ &= \sigma_n^2 \cdot \begin{pmatrix} 2 & 1 & \dots & 1 \\ 1 & 2 & \ddots & \vdots \\ \vdots & \ddots & \ddots & 1 \\ 1 & \dots & 1 & 2 \end{pmatrix}. \end{aligned} \tag{4.10}$$

• Linear model for ambiguity resolution

Given the single-difference combinations from Equations (4.6) and (4.7), a transformation of them from range into position domain is necessary for position estimation as explained in Section 3.2. Corrections on the SD combinations for the projected satellite orbital error, for the satellite clock offsets and biases, and for the dry components of the tropospheric delays are assumed; then, the resulting SD of the linear combinations are written as

$$\Phi_{lc_1}^{kl} = \lambda_{lc_1}\phi_{lc_1}^k - \lambda_{lc_1}\phi_{lc_1}^l = r_{lc_1}^{kl} + T_{w_{lc_1}}^{kl} + \lambda_{lc_1}N_{lc_1}^{kl} + \varepsilon_{\phi_{lc_1}}^{kl}, \tag{4.11}$$

$$\rho_{lc_2}^{kl} = \rho_{lc_2}^k - \rho_{lc_2}^l = r_{lc_2}^{kl} + T_{w_{lc_2}}^{kl} + \varepsilon_{\rho_{lc_2}}^{kl}. \tag{4.12}$$

For simplicity, the indices lc_1 and lc_2 are omitted, and the obtained single-difference observed-

minus-computed combinations for K satellites are represented as

$$\begin{aligned}\mathbf{y}_1 &= \left(\lambda\phi^{1K_{ref}}, \lambda\phi^{2K_{ref}}, ..., \lambda\phi^{(K-1)K_{ref}}\right)^T \\ \mathbf{y}_2 &= \left(\rho^{1K_{ref}}, \rho^{2K_{ref}}, ..., \rho^{(K-1)K_{ref}}\right)^T,\end{aligned}$$

where $\lambda = \lambda_{lc_1}$; and K_{ref} is the SD reference satellite.

The linear model parameterized in integers and real-values, based on the Gauss-Markov model from Equation (3.36), is represented in matrix-vector notation as

$$\begin{pmatrix}\mathbf{y}_1 \\ \mathbf{y}_2\end{pmatrix} = \begin{pmatrix}\mathbf{H}_1 & \mathbf{H}_2 \\ \mathbf{H}_1 & \mathbf{H}_2\end{pmatrix} \cdot \begin{pmatrix}\mathbf{x} \\ T_z\end{pmatrix} + \begin{pmatrix}\lambda \cdot \mathbf{I} \\ \mathbf{0}\end{pmatrix} \cdot \mathbf{N} + \begin{pmatrix}\varepsilon_1 \\ \varepsilon_2\end{pmatrix}, \tag{4.13}$$

where $\mathbf{x}$ is the user position; T_z is the wet component of the tropospheric zenith delay; $\mathbf{N}$ are the combined single-difference (K-1) ambiguities which are still integers; $\mathbf{I}$ is a (K-1)×(K-1) identity matrix; ε_1 and ε_2 are the phase and code noises, respectively; and

$$\mathbf{H}_1 = \left(\mathbf{e}^{1K_{ref}}, \mathbf{e}^{2K_{ref}}, ..., \mathbf{e}^{(K-1)K_{ref}}\right)^T, \tag{4.14}$$

$$\mathbf{H}_2 = \left(m_w^{1K_{ref}}, m_w^{2K_{ref}}, ..., m_w^{(K-1)K_{ref}}\right)^T, \tag{4.15}$$

where $\mathbf{e}^{kK_{ref}} = -(\mathbf{1}^k - \mathbf{1}^{K_{ref}})$ is the SD user-satellite unit direction vectors; and $m_w^{kK_{ref}}$ is the SD tropospheric Niell mapping functions that scales the wet component of the tropospheric zenith delay as a function of the elevation angle of the satellite.

The corrections made for the satellite orbital errors and satellite clock offsets have a centimeter level accuracy, which results in a measurement bias that is taking into account on the noise. The bias generated by multipath is also included on it. Therefore, a biased mean Gaussian noise $\varepsilon \sim \mathcal{N}(\mathbf{b}, \mathbf{\Sigma})$ is assumed. The SD correlation from Equation (4.10) is taken on the covariance matrix from Equation (4.5) into account, so that the resulting noise covariance matrix of the measurements is given by

$$\mathbf{\Sigma} = \mathbf{\Sigma}_{LC_{sm}} \otimes \mathbf{C}_{SD}, \tag{4.16}$$

where $\otimes$ denotes the Kronecker product (see Appendix C).

The linear model from Equation (4.13) can be further simplified in order to relate both linear combinations to the unknown parameters $\mathbf{x}, T_z$ and $\mathbf{N}$ as

$$\begin{pmatrix}\mathbf{y}_1 \\ \mathbf{y}_2\end{pmatrix} = \mathbf{X} \cdot \begin{pmatrix}\mathbf{x} \\ T_z \\ \mathbf{N}\end{pmatrix} + \begin{pmatrix}\varepsilon_1 \\ \varepsilon_2\end{pmatrix}, \qquad \text{with} \quad \mathbf{X} = \begin{pmatrix}\mathbf{H}_1 & \mathbf{H}_2 & \lambda \cdot \mathbf{I} \\ \mathbf{H}_1 & \mathbf{H}_2 & \mathbf{0}\end{pmatrix}. \tag{4.17}$$

This model will be used on the following analysis for ambiguity resolution.

4.3 Sequential fixing

A sequential ambiguity fixing using the bootstrapping estimator with a LAMBDA search (if decorrelation is applied) is suggested. In this case, the fixing is performed from the last to the first ambiguity, i.e. the kth conditional ambiguity is given by

$$\check{\mathbf{N}}_B = [\hat{N}_{k|\mathbf{k}}] = [\hat{N}_k - \sum_{i=k+1}^{K-1} \sigma_{\hat{N}_k \hat{N}_{i|I}} \sigma^{-2}_{\hat{N}_{i|I}} (\hat{N}_{i|I} - [\hat{N}_{i|I}])] \tag{4.18}$$

where $\hat{N}_{i|I}$ stands for the ith least-squares ambiguity obtained through a conditioning on the previous $(I = (j+1), ..., (K-1))$ sequentially rounded ambiguities; and $[\cdot]$ denotes the rounding to the nearest integer operator. The conditional variances can be obtained from the diagonal matrix $\mathbf{D}_{i,i} = \sigma^2_{\hat{N}_{i|I}}$ due to the triangular decomposition of the covariance matrix of the decorrelated ambiguities as follows

$$\mathbf{\Sigma}_{\hat{\mathbf{N}}'} = \mathbf{L}^T \mathbf{D} \mathbf{L} = \mathbf{Z}^T \mathbf{P} \big(\mathbf{X}^T \mathbf{\Sigma}^{-1} \mathbf{X} \big)^{-1} \mathbf{P}^T \mathbf{Z}, \tag{4.19}$$

where $\mathbf{X}$ is the design matrix of the unknown parameters from Equation (4.17); $\mathbf{\Sigma}$ is the covariance matrix of the measurements from Equation (4.16); and $\mathbf{P} = (\mathbf{0}^{(K-1)\times 4}, \mathbf{1}^{(K-1)\times(K-1)})$ selects the float ambiguities $\hat{\mathbf{N}}$ from the float solution $(\hat{\mathbf{x}}, \hat{T}_z, \hat{\mathbf{N}})$.

The bias-affected bootstrapped success rate was described already in Section 4.1. In order to compute it, the real-valued biased vector $\mathbf{b}_{\hat{\mathbf{N}}}$ and the corresponding conditional bias vector $\mathbf{b}_{\hat{N}_{k|\mathbf{k}}}$ are needed. In the following section, a method to approximate these biases will be introduced.

4.4 Bounding the biases

4.4.1 Exponential bias profile

In order to approximate the magnitude of the biases of the real-valued bias vector $\mathbf{b}_{\hat{\mathbf{N}}}$, the following exponential bias profile is assumed for the measurement biases

$$b(\theta) = b_{\max}(0^\circ) \cdot \exp\left\{\frac{\theta}{\xi}\right\}, \tag{4.20}$$

where θ is the elevation angle of the satellite; and ξ is the decay constant of the exponential profile, which can be regulated with the following equation

$$\xi = \frac{90}{\ln\left(\frac{b_{\min}(90^\circ)}{b_{\max}(0^\circ)}\right)}, \tag{4.21}$$

with the minimum assumed bias at an elevation angle of ninety degrees $b_{\min}(90°)$, and the maximum assumed bias at an elevation angle of zero degrees $b_{\max}(0°)$. Figure 4.1 depicts a phase bias profile with a $b_{\min}(90°) = 0.01$ cyc and a $b_{\max}(0°) = 0.1$ cyc.

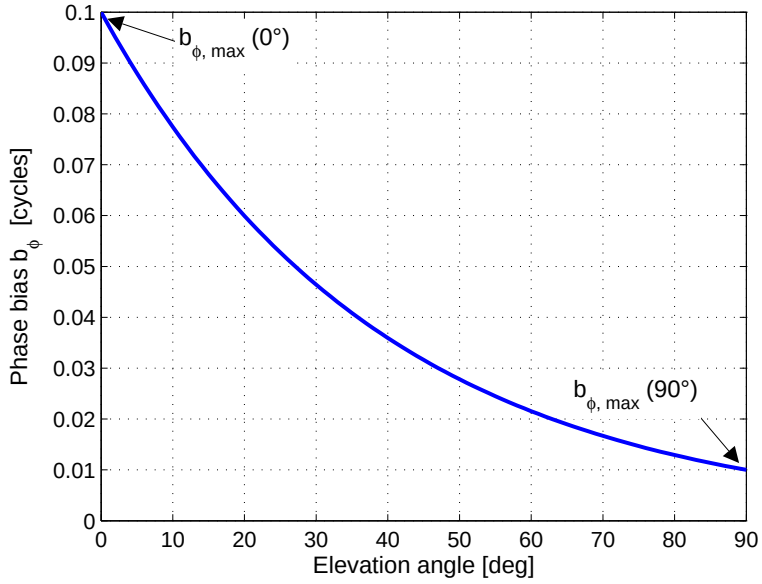

Figure 4.1: Example of an exponential phase bias profile ($b_{\phi,\max}(0°) = 0.1$ cyc, $b_{\phi,\min}(90°) = 0.01$ cyc).

The advantage of this bias profile is that it can be used for the phase and code biases, and it can be adapted for different bias scenarios by changing the $b_{\min}$ and $b_{\max}$ values. In the following section, an upper bound for the conditional biases $b_{\hat{N}_{k|\mathbf{k}}}$ will be derived using the exponential bias profile.

4.4.2 Bounding of conditional biases

In Section 4.1, it has been discussed that the conditional bias vector $\mathbf{b}_{\hat{N}_{i|I}}$ can be linearly related to the real-valued bias vector $\mathbf{b}_{\hat{\mathbf{N}}}$, when the bootstrapping estimator is used. By using the decomposition of the covariance matrix of the decorrelated ambiguities from Equation (4.19), this relation can be written as

$$\begin{aligned}\begin{pmatrix} b_{\hat{N}_1} \\ \vdots \\ b_{\hat{N}_{k|\mathbf{k}}} \end{pmatrix} &= (\mathbf{L}^T)^{-1}\mathbf{Z}^T\mathbf{b}_{\hat{\mathbf{N}}} \\ &= \Big(\underbrace{(\mathbf{L}^T)^{-1}\mathbf{Z}^T\mathbf{P}\big(\mathbf{X}^T\mathbf{\Sigma}^{-1}\mathbf{X}\big)^{-1}\mathbf{X}^T\mathbf{\Sigma}^{-1}}_{\mathbf{S}}\Big)\begin{pmatrix}\mathbf{b}_{lc_1}\\ \mathbf{b}_{lc_2}\end{pmatrix}, \end{aligned} \tag{4.22}$$

where

$$\mathbf{b}_{lc_1} = \alpha_1\lambda_1 b_{\phi_{E1}} + \alpha_2\lambda_2 b_{\phi_{E5}} + \beta_1 b_{\rho_{E1}} + \beta_2 b_{\rho_{E5}}, \tag{4.23}$$

$$\mathbf{b}_{lc_2} = b_1 b_{\rho_{E1}} + b_2 b_{\rho_{E5}} \tag{4.24}$$

are the residual biases of the code-carrier and code-only combinations; with the phase and code weighting coefficients $\alpha_1, \alpha_2, \beta_1$ and β_2 of the code-carrier combination; the code weighting coefficients b_1 and b_2 of the code-only combination; and the phase and code biases on E1 and E5 $b_{\phi_{(\cdot)}}$ and $b_{\rho_{(\cdot)}}$. Note that the conditional biases depend also on the decorrelation **Z**-matrix, (see Section 4.5).

By substituting Equations (4.23) and (4.24) into (4.22), the conditional biases can be rewritten into

$$\begin{aligned} b_{\hat{N}_{k|\mathbf{k}}} &= \sum_{i=1}^{K-1} \mathbf{S}_{k,i} \cdot b_{lc_1}^{(i)} + \sum_{i=1}^{K-1} \mathbf{S}_{k,i+(K-1)} \cdot b_{lc_2}^{(i)} \\ &= \sum_{i=1}^{K-1} \mathbf{S}_{k,i}\alpha_1\lambda_1 \cdot b_{\phi_{E1}}^{(i)} + \sum_{i=1}^{K-1} \mathbf{S}_{k,i}\alpha_2\lambda_2 \cdot b_{\phi_{E5}}^{(i)} \\ &\quad + \sum_{i=1}^{K-1} (\mathbf{S}_{k,i}\beta_1 + \mathbf{S}_{k,i+(K-1)}b_1) \cdot b_{\rho_{E1}}^{(i)} \\ &\quad + \sum_{i=1}^{K-1} (\mathbf{S}_{k,i}\beta_2 + \mathbf{S}_{k,i+(K-1)}b_2) \cdot b_{\rho_{E5}}^{(i)}. \end{aligned} \tag{4.25}$$

The magnitude and sign of the biases are not known. However, an upper bound on the magnitude can be derived first for them by using the *bias exponential profile*. The exponential profile is determined for the phase and code biases as

$$b_{\phi,\max}^{(i)}(\theta) = b_{\phi,\max}(0^\circ) \cdot \exp\left\{\frac{\theta^{(i)}}{\xi_\phi}\right\}, \qquad \xi_\phi = \frac{90}{\ln\left(\frac{b_{\phi,\min}(90^\circ)}{b_{\phi,\max}(0^\circ)}\right)} \tag{4.26}$$

$$b_{\rho,\max}^{(i)}(\theta) = b_{\rho,\max}(0^\circ) \cdot \exp\left\{\frac{\theta^{(i)}}{\xi_\rho}\right\}, \qquad \xi_\rho = \frac{90}{\ln\left(\frac{b_{\rho,\min}(90^\circ)}{b_{\rho,\max}(0^\circ)}\right)}. \tag{4.27}$$

The resulting magnitude of the phase and code biases are assumed to be equal on the frequencies E1 and E5, this means

$$b_{\phi,\max}^{(i)}(\theta) = b_{\phi,\max_{E1}}^{(i)}(\theta) = b_{\phi,\max_{E5}}^{(i)}(\theta) \tag{4.28}$$

$$b_{\rho,\max}^{(i)}(\theta) = b_{\rho,\max_{E1}}^{(i)}(\theta) = b_{\rho,\max_{E5}}^{(i)}(\theta). \tag{4.29}$$

Having the magnitude of the phase and code biases, the upper bound on the conditional biases is derived by assuming that all the biases in Equation (4.25) accumulate positively,

this means

$$\begin{aligned} b_{\phi_{E1}}^{(i)} &= \text{sign}(\mathbf{S}_{k,i}\alpha_1\lambda_1) \cdot b_{\phi,\max_{E1}}^{(i)} \\ b_{\phi_{E5}}^{(i)} &= \text{sign}(\mathbf{S}_{k,i}\alpha_2\lambda_2) \cdot b_{\phi,\max_{E5}}^{(i)} \\ b_{\rho_{E1}}^{(i)} &= \text{sign}(\mathbf{S}_{k,i}\beta_1 + \mathbf{S}_{k,i+(K-1)}b_1) \cdot b_{\rho,\max_{E1}}^{(i)} \\ b_{\rho_{E5}}^{(i)} &= \text{sign}(\mathbf{S}_{k,i}\beta_2 + \mathbf{S}_{k,i+(K-1)}b_2) \cdot b_{\rho,\max_{E5}}^{(i)}. \end{aligned}$$

Given the conditional biases $b_{\hat{N}_{k|\mathbf{k}}}$, it would be interesting to know which satellite could affect primarily the success rate. This can be given by

$$k_c = \arg\min_k \frac{0.5 - b_{\hat{N}_{k|\mathbf{k}}}}{\sigma_{\hat{N}_{k|\mathbf{k}}}}, \tag{4.30}$$

with the corresponding conditional variance $\sigma_{\hat{N}_{k|\mathbf{k}}}$.

4.5 Partial integer decorrelation

For unbiased measurements, the LAMBDA method achieves a higher success rate due to the integer decorrelation which can also be beneficial for the sequential bootstrapped estimator. However, this performance degrades notably in the presence of biases as the integer decorrelation amplifies the biases, disturbing also the gain obtained from the variance reduction by carrier smoothing. Furthermore, if the biases are amplified to more than half a cycle, reliable ambiguity resolution is prevented. Therefore, a partial integer decorrelation is suggested.

The ambiguity decorrelation matrix $\mathbf{Z}$ is constructed by a sequence of integer approximated Gauss transformations, which carry out the decorrelation, and permutations of the ambiguities in order to allow further decorrelation. A triangular decomposition of the covariance matrix is done, where the Gauss transformation only affects the unit lower triangular matrix $\mathbf{L}$ without changing the diagonal matrix $\mathbf{D}$. This means, that the variances are changed, while the conditional variances are not affected until a reordering of ambiguities is done. Thus, the ambiguity decorrelation matrix is constructed iteratively as

$$\mathbf{Z} = \mathbf{Z}_1 \cdot \mathbf{Z}_2 \cdot ... \cdot \mathbf{Z}_{N_{it}}. \tag{4.31}$$

The problem by a complete integer decorrelation, i.e. $N_{it} = N_{it,\max}$, with original biased ambiguities is that the corresponding transformed ambiguities will also be biased as explained in Section 4.1. And the transformed real-valued biased vector is affected by the ambiguity decorrelation matrix $\mathbf{Z}$ as

$$\mathbf{Z}^T\mathbf{b}_{\hat{\mathbf{N}}} = (\mathbf{Z}_1 \cdot \mathbf{Z}_2 \cdot ... \cdot \mathbf{Z}_{N_{it}})^T\mathbf{b}_{\hat{\mathbf{N}}}. \tag{4.32}$$

Therefore, a reduce number of decorrelation steps, i.e. $N_{it} < N_{it,\max}$ is suggested or even more no decorrelation at all. Figure 4.2 shows this problem when a complete or a partial integer decorrelation of five sequentially fixed ambiguities is applied. The conditional biases are affected in both cases in the same manner (i.e. there exists amplification and reduction of them), however, the severity is considerably reduced with partial integer decorrelation. The amplification of the biases is several times higher than their reduction. Moreover, this amplification occurs on the first ambiguities to be fixed reducing thus the bootstrapping success rate. The corresponding conditional standard deviations are showed in Figure 4.3, in order to compare the effect of the decorrelation on the variance.

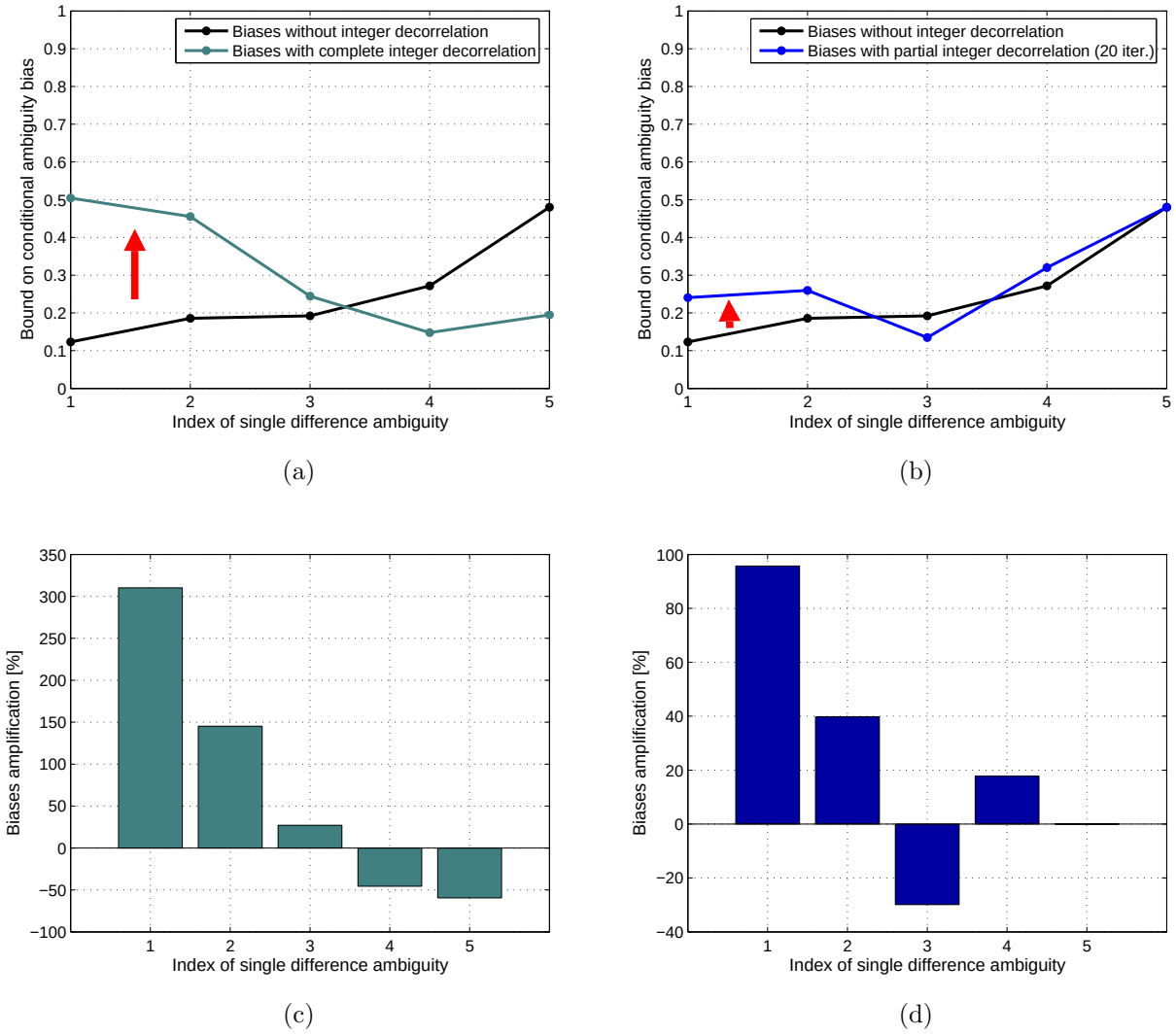

Figure 4.2: Biases amplification with complete integer decorrelation (a,c) and partial integer decorrelation (b,d) with their corresponding decorrelation matrix $\mathbf{Z}$.

The resulting complete and partial decorrelation matrices are

$$\mathbf{Z}_{comp} = \begin{pmatrix} -1 & 0 & 0 & 1 & 1 \\ 0 & 0 & 1 & 1 & 1 \\ 0 & 1 & 1 & 2 & 1 \\ 1 & 0 & -1 & -2 & -1 \\ 0 & 0 & 0 & -1 & -1 \end{pmatrix} \qquad \mathbf{Z}_{part} = \begin{pmatrix} 1 & 0 & 0 & 0 & 0 \\ 0 & 0 & 0 & 1 & 0 \\ 0 & 1 & 1 & 1 & 1 \\ 0 & 0 & 0 & -1 & -1 \\ 0 & -1 & 0 & 0 & 0 \end{pmatrix}$$

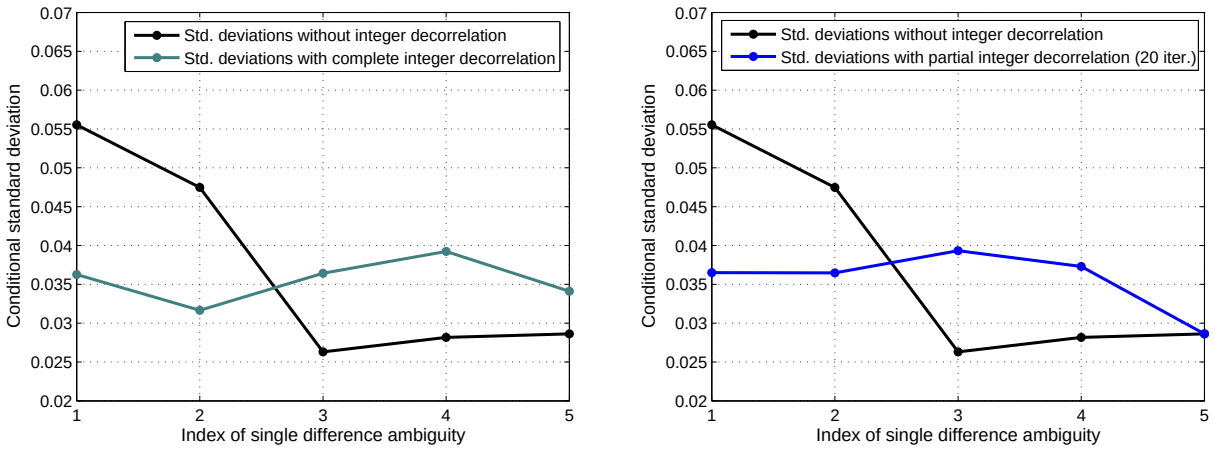

(a) (b)

Figure 4.3: Conditional standard deviations with complete integer decorrelation (a) and partial integer decorrelation (b).

Figure 4.4 shows the probability of wrong fixing as a function of the maximum phase and code biases, and the number of decorrelation iterations. An exponential bias profile is assumed, where the maximum code bias $b_{\rho,\max}(90°) = 1$ cm; and a smoothing time of 30 seconds is applied for both linear combinations. As the biases increase, a reduced number of decorrelation iterations is required for a lower probability of wrong fixing. The achievable probability of wrong fixing by a partial integer decorrelation can be several orders of magnitude lower than in the case of a complete integer decorrelation.

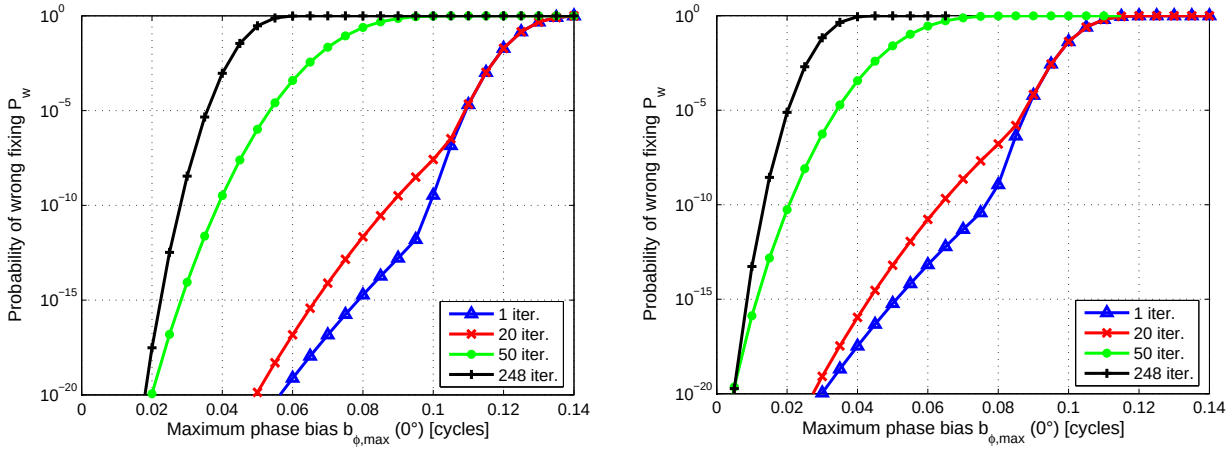

(a) $b_{\rho,\max}(0°) = 2cm$ (b) $b_{\rho,\max}(0°) = 5cm$

Figure 4.4: Probability of wrong fixing as a function of the E1 and E5 phase biases upper bound ($b_{\phi,\max_{E1}}(0°) = b_{\phi,\max_{E5}}(0°)$); and different number of integer decorrelation iterations.

4.6 Partial ambiguity fixing

A higher reliable resolution of all ambiguities can not always be possible within a few epochs, especially in the presence of severe multipath or large uncorrected biases. However, some of them can still be resolved with higher reliability. As the success rate of the bootstrapped estimator depends plenty on the utilized order of the measurements for sequential fixing, the number of sequentially fixable ambiguities N_p can be maximized by choosing an appropriate sorting of the measurements. The permutation of the measurements from Equation (4.17) can be given by

$$\begin{pmatrix}\tilde{\mathbf{y}}_1\\ \tilde{\mathbf{y}}_2\end{pmatrix} = \begin{pmatrix}\mathbf{P_O y}_1\\ \mathbf{P_O y}_2\end{pmatrix} = \tilde{\mathbf{X}} \cdot \begin{pmatrix}\mathbf{x}\\ T_z\\ \tilde{\mathbf{N}}\end{pmatrix} + \begin{pmatrix}\tilde{\varepsilon}_1\\ \tilde{\varepsilon}_2\end{pmatrix}, \tag{4.33}$$

with

$$\tilde{\mathbf{X}} = \begin{pmatrix}\mathbf{P_O H}_1 & \mathbf{P_O H}_2 & \lambda \cdot \mathbf{I}\\ \mathbf{P_O H}_1 & \mathbf{P_O H}_2 & \mathbf{0}\end{pmatrix} \quad \text{and} \quad \tilde{\mathbf{N}} = \mathbf{P_O N}, \tag{4.34}$$

where $\mathbf{P_O}$ is a $(K-1)\times(K-1)$ permutation matrix, in which every row and column contains precisely a single 1 with zeros everywhere else according to the permutation vector $\mathbf{O}$. For example,

$$\mathbf{P_O} = \begin{pmatrix}0 & 1 & 0\\ 1 & 0 & 0\\ 0 & 0 & 1\end{pmatrix} \qquad \text{with} \qquad \mathbf{O} = (2,1,3).$$

The permutation matrix is also applied to the phase and code residual biases from Equations (4.28) and (4.29) as follows

$$\tilde{b}^{(i)}_{\phi,\max}(\theta) = \mathbf{P_O} \cdot b^{(i)}_{\phi,\max}(\theta) \tag{4.35}$$

$$\tilde{b}^{(i)}_{\rho,\max}(\theta) = \mathbf{P_O} \cdot b^{(i)}_{\rho,\max}(\theta). \tag{4.36}$$

The sequentially fixable ambiguities that satisfy a required higher reliability in terms of the biased success rate from Equation (4.2) will then compose the partial ambiguity fixing subset $\mathbf{N}_p \in \mathbf{N}$. The maximum number of fixable ambiguities while using different permutations of measurements is given by

$$\max_{\mathbf{P_O}} N_p \quad : \quad P_s = \prod_{i=K-N_p}^{K-1} P(\check{\tilde{N}}_{i|I} = \tilde{N}_i) \overset{!}{\leq} P_{th}, \tag{4.37}$$

where P_{th} is the required probability of correct integer estimation; and

$$P(\check{\tilde{N}}_{i|I} = \tilde{N}_i) = \Phi\left(\frac{1 - 2b_{\hat{\tilde{N}}_{i|I}}}{2\sigma_{\hat{\tilde{N}}_{i|I}}}\right) + \Phi\left(\frac{1 + 2b_{\hat{\tilde{N}}_{i|I}}}{2\sigma_{\hat{\tilde{N}}_{i|I}}}\right) - 1, \tag{4.38}$$

with the conditional variances $\sigma_{\hat{\tilde{N}}_{i|I}}$ and the conditional biases $b_{\hat{\tilde{N}}_{i|I}}$, which can be obtained by replacing $\mathbf{X}$ by the permuted matrix $\tilde{\mathbf{X}}$ in Equations (4.19) and (4.22).

An appropriate order of the measurements for sequential fixing is however not an easy challenge due to all the different possibilities to determine it. In the following chapter, some methods to find a larger subset of reliable fixable ambiguities $\mathbf{N}_p$ by looking for an adequate order of fixing are discussed. Furthermore, a new method is suggested to find the largest subset $\mathbf{N}_p$ by performing a search for an optimum order of fixing.

Chapter 5

Partial ambiguity fixing methods

Five different methods to find a larger subset of reliable fixable ambiguities are discussed on this chapter. The first four of them are based on a sequential fixing scheme, hence a specific order of fixing is needed; while the last one is based on an integer rounding scheme. All of them are based on the absolute carrier phase positioning model described on the last chapter.

5.1 PRN order method

This method is actually based on a sequential fixing of the *pseudo-random noise* (PRN)-number order of the satellites. It is a very simple method, because a permutation of the measurements is not required. However, it usually does not offer an improvement on the number of reliably fixable ambiguities N_p. Figure 5.1 shows the scheme for this method.

5.2 Sequential fixing Ascending Variance Order (SAVO) method

The aim of this method is to determine an order, in which the first ambiguities to be fixed show lower variances; and thus to increase the probability to obtain a larger number of reliably fixable ambiguities N_p. Figure 5.2 illustrates the scheme for this method, where the shadowed boxes refer to the algorithm to find the respective order.

The algorithm for K visible satellites and $(K-1)$ single difference ambiguities consists of the following steps:

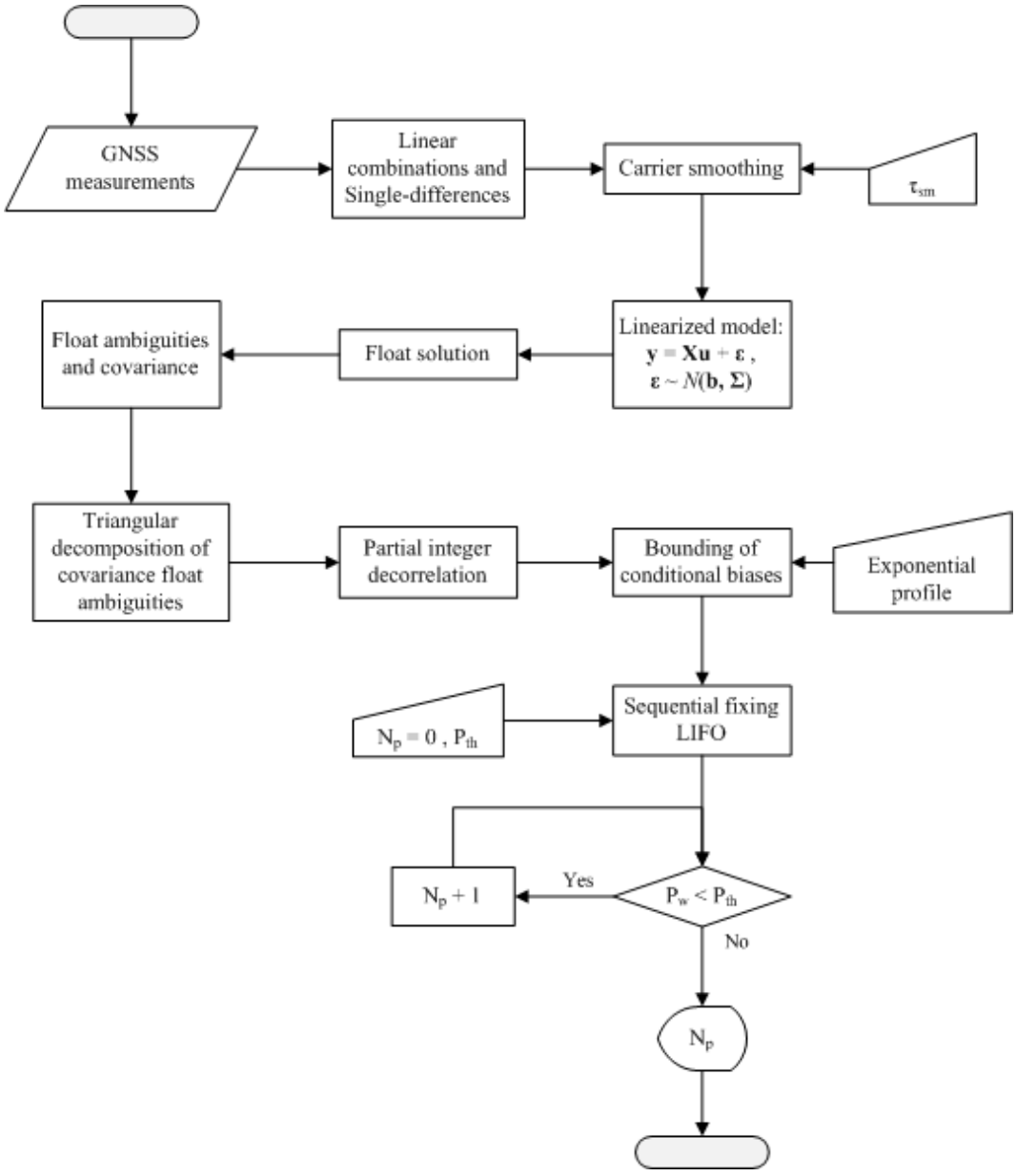

Figure 5.1: PRN-order scheme.

Step 1: The ambiguity with the minimum variance of the covariance matrix of the float ambiguities $\boldsymbol{\Sigma}_{\hat{N}} = \mathbf{P}\left(\mathbf{X}^T\boldsymbol{\Sigma}^{-1}\mathbf{X}\right)^{-1}\mathbf{P}^T$ is selected to be fixed first, it reads

$$N_{\mathrm{V}_1} = \min_i \boldsymbol{\Sigma}_{\hat{N}}(i,i), \qquad \text{for} \qquad i = 1, 2, ..., K-1. \tag{5.1}$$

Step 2: The covariance matrix of the remaining float ambiguities is calculated again, but now for $(K-2)$ ambiguities, because the ambiguity selected on step 1 is assumed to be fixed. This is done by deleting the $(4+i\text{th})$ column in the design matrix of the unknown parameters $\mathbf{X}$ and by using the adapted selection matrix $\mathbf{P} = (\mathbf{0}^{(K-2)\times 4}, \mathbf{1}^{(K-2)\times(K-2)})$. Afterwards, the

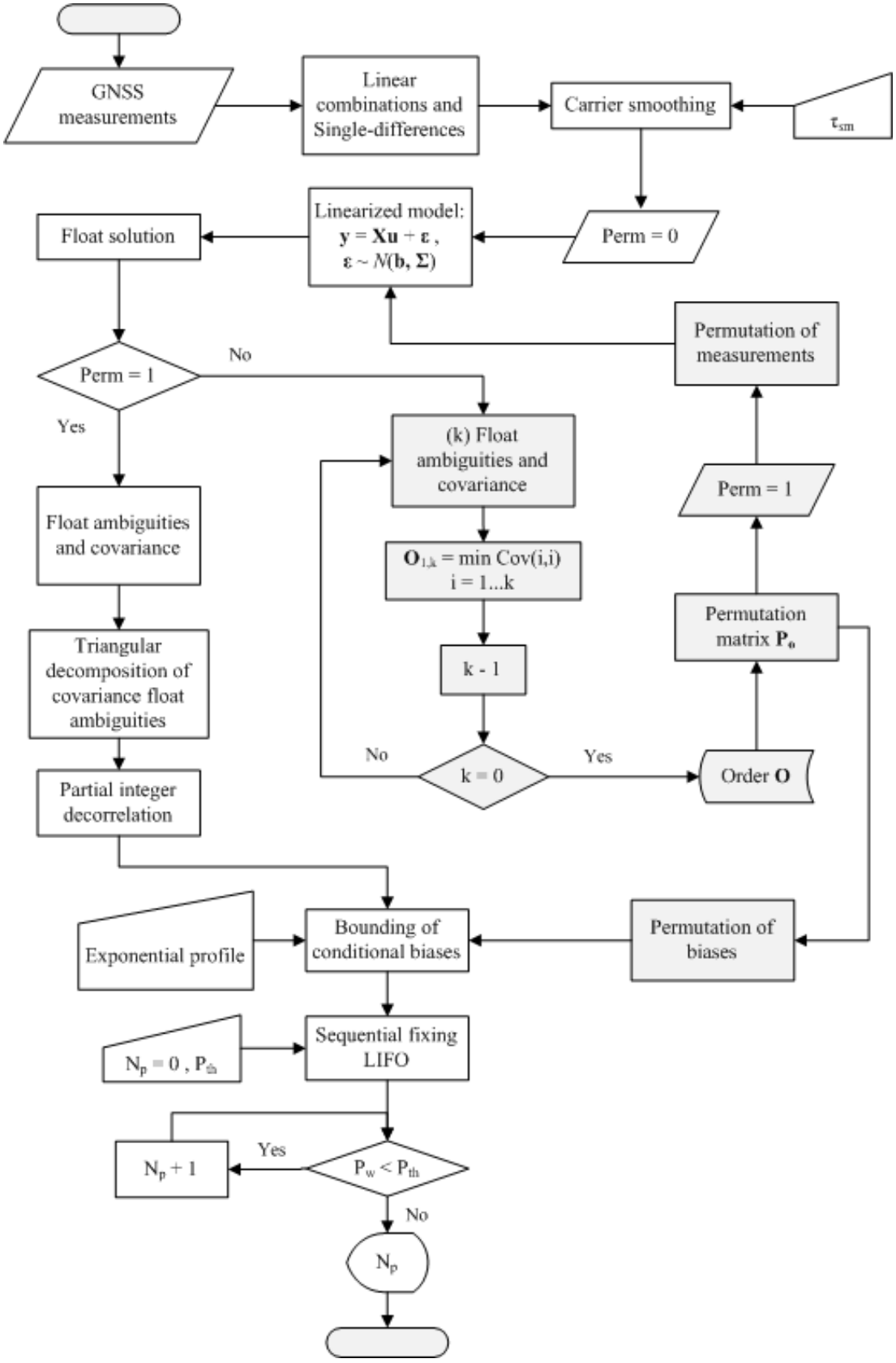

Figure 5.2: SAVO method scheme.

ambiguity with the minimum variance is chosen now as the second to be fixed, i.e.

$$N_{\mathrm{V}_2} = \min_i \acute{\mathbf{\Sigma}}_{\hat{N}}(i,i), \qquad \text{for} \qquad i = 1, 2, ..., K-2. \tag{5.2}$$

Note that the assumed covariance matrix is denoted by an *acute* sign ($\acute{\cdot}$) in order to differentiate it from the primary covariance matrix of float ambiguities.

The following example for $K = 7$ satellites shows how is determined step-by-step the order of fixing vector $\mathbf{O}$, which contains the sub-indices of the ambiguities as entries.

$$\begin{aligned}
&(1) \quad \mathbf{O} = (1,2,3,4,5,6), \quad \text{with} \quad N_{\mathrm{V}_1} = 2 \quad \rightarrow \quad \mathbf{O} = (1,3,4,5,6,2) \\
&(2) \quad \mathbf{O} = (1,3,4,5,6,2), \quad \text{with} \quad N_{\mathrm{V}_2} = 5 \quad \rightarrow \quad \mathbf{O} = (1,3,4,6,5,2) \\
&\qquad\qquad\quad \vdots \qquad\qquad\quad \vdots
\end{aligned}$$

Step 3: The previous step is performed but now for $(K-3)$ ambiguities and the third ambiguity to be fixed N_{V_3} is chosen. This is done iteratively for all the rest of the ambiguities in order to determine the order of fixing vector as follows

$$\mathbf{O} = (N_{\mathrm{V}_{K-1}}, N_{\mathrm{V}_{K-2}}, ..., N_{\mathrm{V}_1}). \tag{5.3}$$

Step 4: The permutation matrix $\mathbf{P_O}$ is constructed based on the order of fixing vector $\mathbf{O}$ and is applied to the measurements, and the phase and code biases by using Equations (4.33), (4.35) and (4.36).

Step 5: Sequential fixing from the last to the first ambiguity is used, and the number of reliable fixable ambiguities N_p using this method is obtained from Equation (4.37).

5.3 Sequential BLewitt fixing Order (SEBLO) method

This method is similar to the previous SAVO method. It determines the order of fixing by looking for the first ambiguities to be fixed which have a minimum probability of wrong fixing. As in the previous section, Figure 5.3 shows the scheme for this method, where the shadowed boxes refer to the algorithm.

The algorithm for K visible satellites and $(K-1)$ single difference ambiguities consists of the following steps:

Step 1: The biased success rate of each ambiguity is computed by using the standard deviations from the covariance matrix of the float ambiguities and the PRN order as follows

$$P_s^{(i)}(\acute{N}_i = N_i) = \Phi\left(\frac{1 - 2b_{\hat{N}_{i|I}}}{2\sigma_{\hat{N}_i}}\right) + \Phi\left(\frac{1 + 2b_{\hat{N}_{i|I}}}{2\sigma_{\hat{N}_i}}\right) - 1, \qquad \sigma_{\hat{N}_i} = \sqrt{\mathbf{\Sigma}_{\hat{N}}(i,i)}. \tag{5.4}$$

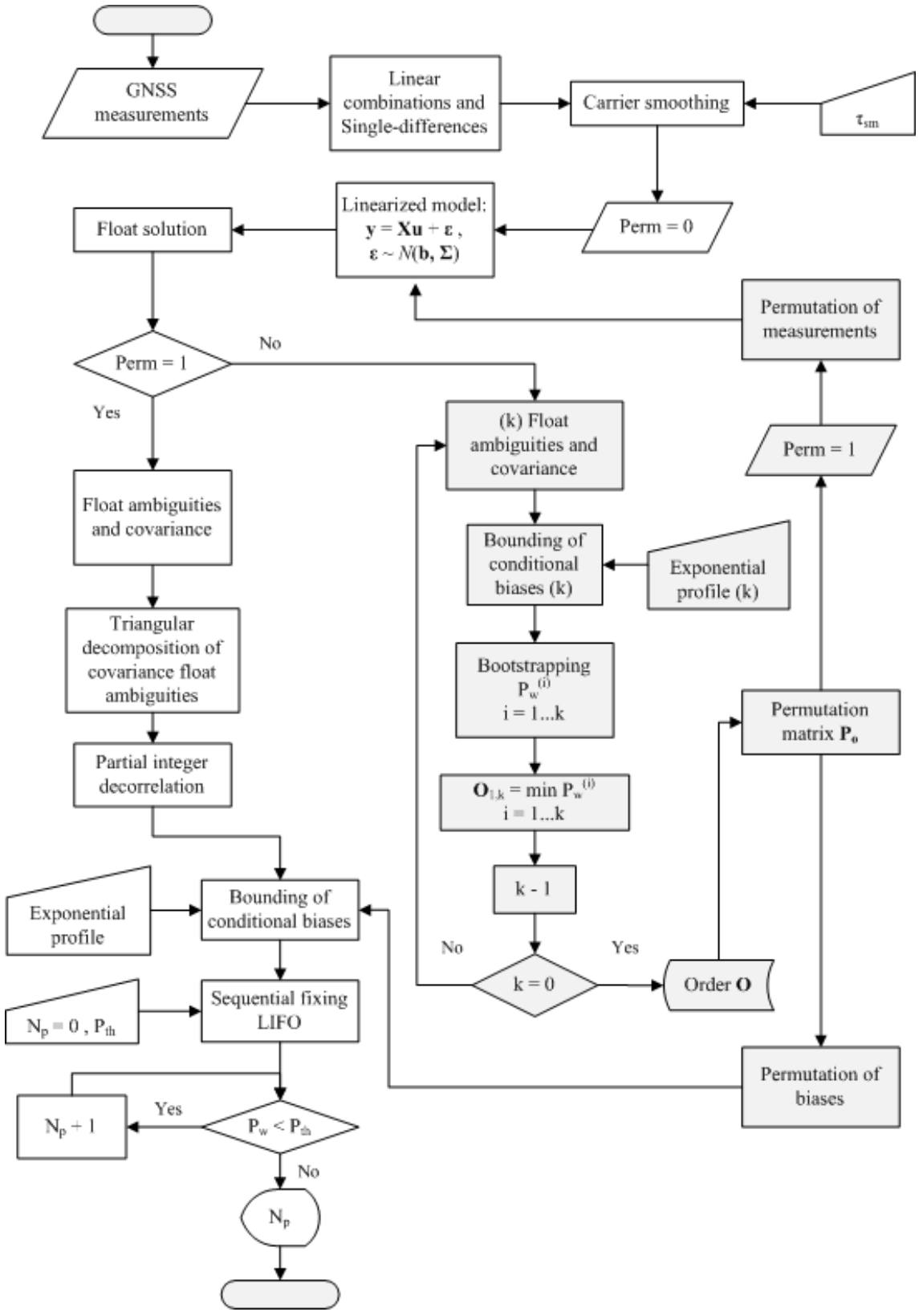

Figure 5.3: SEBLO method scheme.

The probability of wrong fixing $P_w^{(i)}$ is calculated from the resulting success rate as (1 - $P_s^{(i)}$). And the ambiguity with the corresponding minimum probability of wrong fixing is selected to be fixed first, it reads

$$N_{pw_1} = \min_i P_w^{(i)}, \qquad \text{for} \qquad i = 1, 2, ..., K-1. \tag{5.5}$$

Step 2: The covariance matrix of the remaining float ambiguities is calculated again $\acute{\mathbf{\Sigma}}_{\hat{N}}$, but now for $(K-2)$ ambiguities, because the ambiguity selected on step 1 is assumed to be fixed. This is done by deleting the $(4+i\text{th})$ column in the design matrix of the unknown parameters $\mathbf{X}$ and by using the adapted selection matrix $\mathbf{P} = (\mathbf{0}^{(K-2)\times 4}, \mathbf{1}^{(K-2)\times(K-2)})$. Afterwards, the success rate is calculated again as given in step 1, and the ambiguity with the minimum probability of wrong fixing is chosen now as the second to be fixed, i.e.

$$N_{pw_2} = \min_i P_w^{(i)}, \qquad \text{for} \qquad i = 1, 2, ..., K-2. \tag{5.6}$$

The order of fixing vector $\mathbf{O}$ is determined step-by-step as given in the example for the SAVO method (see Section5.2).

Step 3: The previous step is performed but now for $(K-3)$ ambiguities and the third ambiguity to be fixed N_{pw_3} is chosen. This is done iteratively for all the rest of the ambiguities in order to determine the order of fixing vector as follows

$$\mathbf{O} = (N_{pw_{K-1}}, N_{pw_{K-2}}, ..., N_{pw_1}). \tag{5.7}$$

Step 4: The permutation matrix $\mathbf{P_O}$ is constructed based on the order of fixing vector $\mathbf{O}$ and is applied to the measurements, and the phase and code biases by using Equations (4.33), (4.35) and (4.36).

Step 5: Sequential fixing is used as in the previous methods, and the number of reliable fixable ambiguities N_p using this method is obtained from Equation (4.37).

5.4 Sequential Optimum Fixing Order Search (SOFOS) method

This new method suggest a search for the optimum fixing order which maximizes the number of reliable fixable ambiguities N_p for a required probability of wrong fixing P_{th}. In this case, for K visible satellites and thus $(K-1)$ single difference ambiguities to be fixed, the search space consists of $(K-1)!$ possible orders. Therefore, it could be very large in cases for

Table 5.1: Search space SOFOS method.

K satellites	No. of possible orders
8	5,040
9	40,320
10	362,880
11	3,628,800

example where more than nine satellites are visible for the user. Table 5.1 shows this size of the corresponding search space for eight to eleven visible satellites.

A completely search for the optimum order is then often unfeasible and would take a lot of time. However, the search space can be dramatically reduced by using the two following constraints:

1. Azimuth constraint

The azimuth constraint is based on the idea that a good satellite geometry offers usually a lower probability of wrong fixing. Therefore, a required azimuthal separation between two sequentially fixable ambiguities is suggested. A maximum azimuthal threshold ΔAzi_{th} between the first two ambiguities to be fixed is given. Depending on this maximum threshold, the following required azimuthal separation for the remaining ambiguities decreases gradually in order to facilitate their less probable but not excluded fixing. Hence, the choice of ΔAzi_{th} represents a trade-off between the maximum number of fixable ambiguities N_p and the reduction of the search space. This trade-off is illustrated on Figure 5.4, where the number of fixable ambiguities reduces while the azimuthal threshold increases. However, the reduction of the number of fixable ambiguities varies also for different satellite geometries. Figure 5.4a shows that one fixable ambiguity is already lost by an $\Delta Azi_{th} < 20°$, while for another case, it happens until $\Delta Azi_{th} > 120°$ (Figure 5.4b).

After investigating different scenarios for this trade-off, it has been identified that a $\Delta Azi_{th} = 45°$ reduces radically the search space with a considerably lower effect on the maximum number of fixable ambiguities. This can be seen on Figure 5.5, where the number of fixable ambiguities without an azimuthal separation constraint and a $\Delta Azi_{th} = 45°$ are compared for different simulated Galileo geometries.

The azimuth constraint reads mathematically

$$|Azi^{(k)} - Azi^{(k+1)}| \overset{!}{>} \left(\frac{K-1-k}{K-2}\right) \cdot \Delta Azi_{th}. \tag{5.8}$$

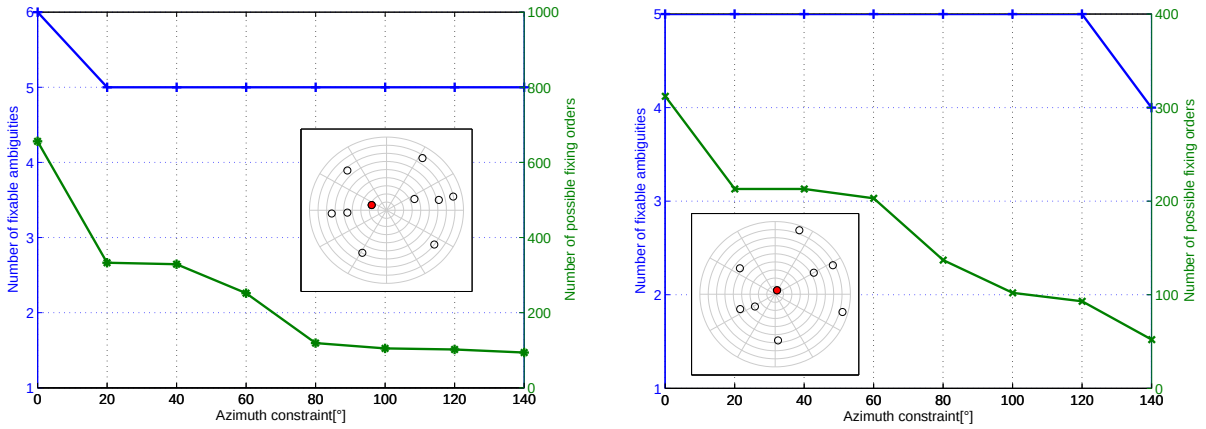

(a) (b)

Figure 5.4: Azimuth trade-off for two different satellite geometries.

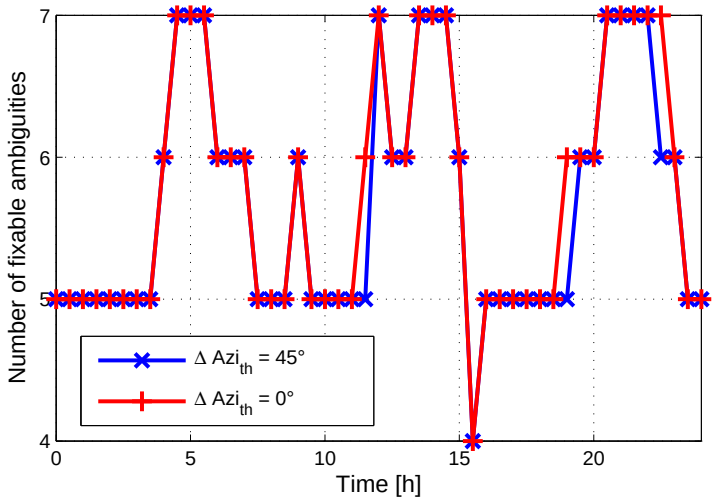

Figure 5.5: Number of fixable ambiguities comparison between an azimuthal threshold of 45° and without it.

Figure 5.6 shows two skyplots, where the azimuth constraint is graphically described. In the first fixing step (Figure 5.6a), the number of fixing candidates is reduced from 9 to 7, where the maximum azimuthal threshold was chosen to 45°. The selected ambiguity is marked in green, while the ambiguities, which have been constrained, are marked in red. On the second fixing step (Figure 5.6b), the number of candidates is from 8 to 5 reduced, despite the azimuthal separation constraint is weakened to 40°. This process continues until all ambiguities have been taken into account.

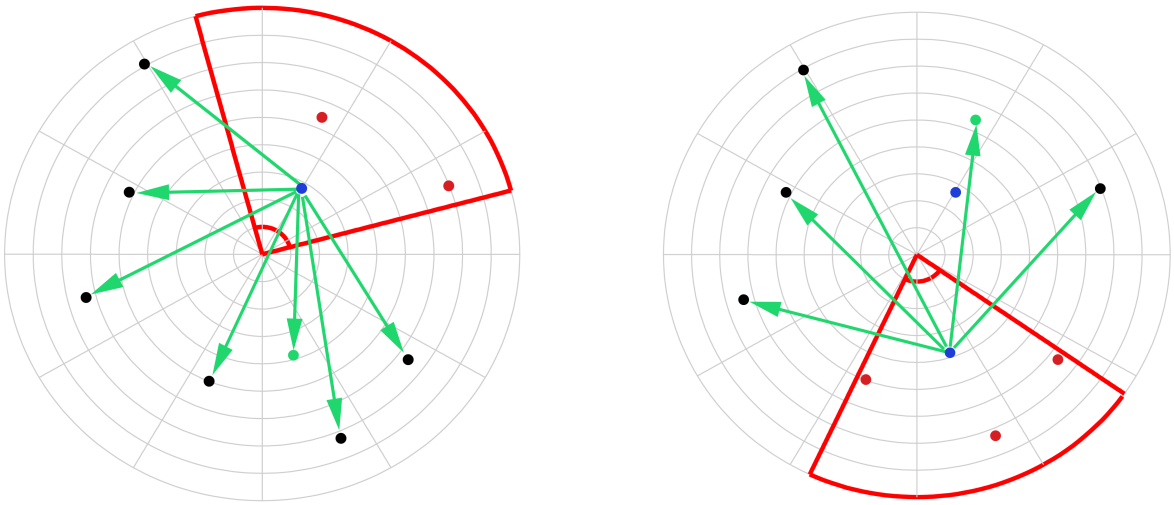

(a) 1st fixing step ($\Delta Azi_{1-2} = 45°$). (b) 2nd fixing step ($\Delta Azi_{2-3} = 40°$).

Figure 5.6: Azimuth constraint graphical representation.

2. Suffix constraint

The search space can be represented by a tree diagram, where the nodes refer to the ambiguities and the branches are characterized by the probability of wrong fixing. The suffix constraint is based on the required probability of wrong fixing P_{th}, this means that the probability of wrong fixing is computed for one order, and once the probability of wrong fixing of a branch exceeds the threshold P_{th} in a node, the following branch is no more extended; and thus the corresponding orders are not taken anymore into account. The respective reached number of fixable ambiguities is saved as current maximum $N_{p_{cur}}$ until another reaches more than it. Moreover, if the reached number of fixable ambiguities by following orders is less than the current maximum, the respective branches are also no more extended. Figure 5.7 depicts the idea of the suffix constraint and azimuth constraint for $k = K - 1$ ambiguities in a tree diagram.

Both constraints complement one another, because the azimuth constraint confines shorter branches, while the other constrains larger branches. The reduction of the search space is depicted on Figure 5.8, where the number of remaining fixing orders to be searched is dramatically reduced in comparison to the (K-1)! initial possible fixing orders. An exponential profile of $b_{\max}(0°) = 0.1$ and $b_{\max}(90°) = 0.01$ for the code [cm] and phase [cyc] biases, a maximum azimuthal threshold of $\Delta Azi_{th} = 45°$ and a smoothing time $\tau_{sm} = 20s$ have been considered with a simulated Galileo geometry at 48.1507° latitude and 11.569° longitude. Figure 5.8b shows the comparison between the search spaces, in a logarithmic scale, before and after the constraints are applied.

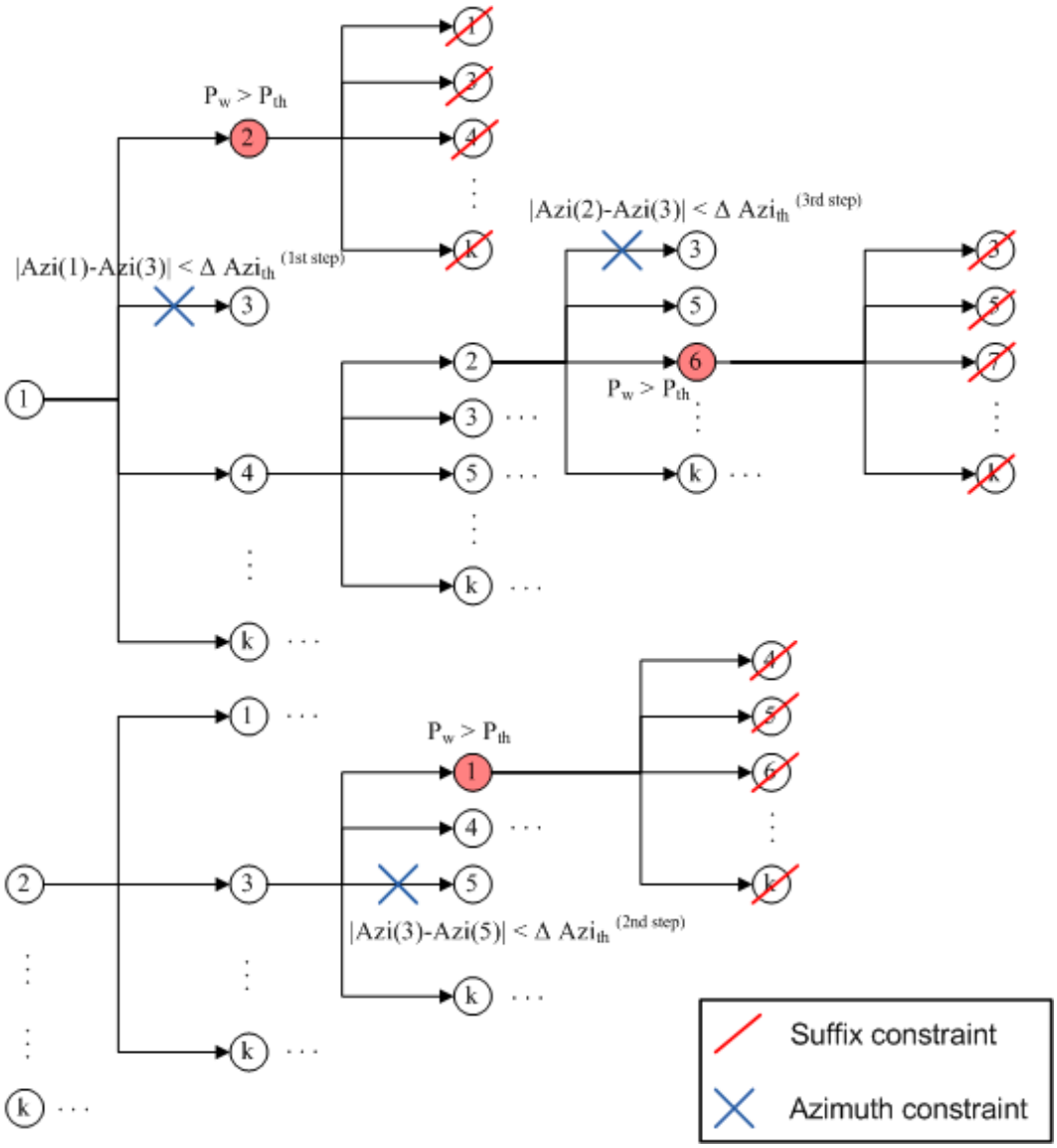

Figure 5.7: Suffix and azimuth constraint for the search space represented as a tree diagram.

After both constraints are applied and sequential fixing is done, many orders reach usually the same maximum number of fixable ambiguities N_p. In order to solve this, the optimum one is chosen by comparing the probability of wrong fixing of the fixed ambiguities. The maximum probability of wrong fixing of each corresponding order is selected, and then the order with the minimum probability of wrong fixing from these is chosen as the optimum order $\mathbf{O}_{opt}$. This is described in the following example for $K = 6$, where the P_w from three

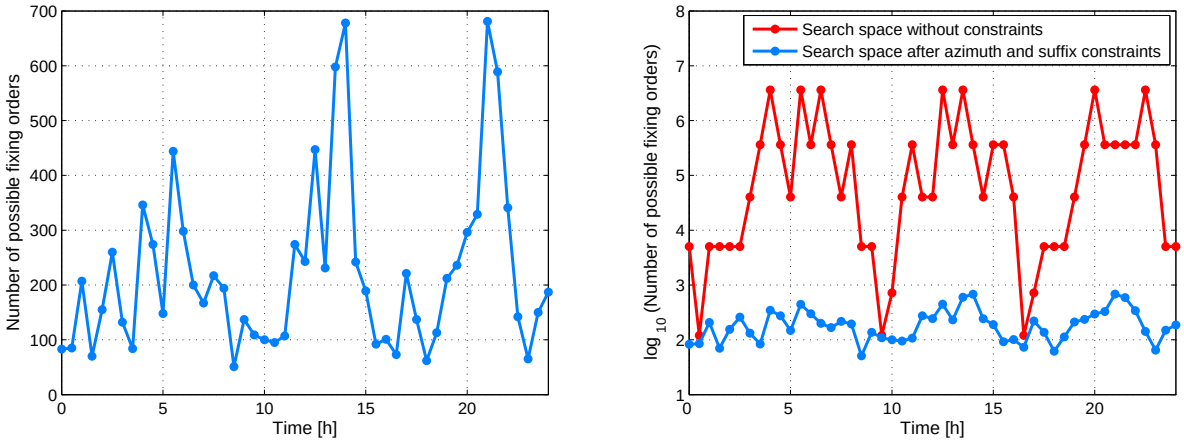

(a) Reduced search space after azimuth and suffix constraints.

(b) Comparison between the original and reduced search spaces.

Figure 5.8: Search space reduction.

orders with $N_p = 3$ is analyzed:

$$(\mathbf{O}_1) \quad P_w = (1.0, 0.8, \underbrace{5.28 \cdot 10^{-10}, 5.20 \cdot 10^{-10}, 3.18 \cdot 10^{-12}}_{P_{w,\max_1}=5.28\cdot 10^{-10}})$$

$$(\mathbf{O}_2) \quad P_w = (1.0, 0.6, \underbrace{8.38 \cdot 10^{-10}, 3.20 \cdot 10^{-10}, 2.18 \cdot 10^{-15}}_{P_{w,\max_2}=8.38\cdot 10^{-10}})$$

$$(\mathbf{O}_3) \quad P_w = (1.0, 0.3, \underbrace{6.48 \cdot 10^{-10}, 5.25 \cdot 10^{-11}, 1.18 \cdot 10^{-14}}_{P_{w,\max_3}=6.48\cdot 10^{-10}})$$

$$\text{Then:} \qquad \mathbf{O}_{opt} = \min_{O_{P_{w,\max}}} (P_{w,\max_1}, P_{w,\max_2} P_{w,\max_3}) \qquad \rightarrow \mathbf{O}_{opt} = \mathbf{O}_1.$$

The algorithm of this method is illustrated on Figure 5.9.

5.5 Rounding fixing method

The ambiguity resolution of this method is based on an integer rounding estimator, therefore it does not need a search for an adequate order of fixing, making it very simple to use. An ambiguity decorrelation is also not used. Figure 5.10 shows the scheme for this method. Although this method it does not take the correlation between the ambiguities into account, the success rate can be approximated by using the following equation

$$\begin{aligned} P_s &= \prod_{i=1}^{n} P_s^{(i)}(\check{N}_i = N_i) \\ &= \left(\min_i P_s^{(i)} \right)^n, \end{aligned} \tag{5.9}$$

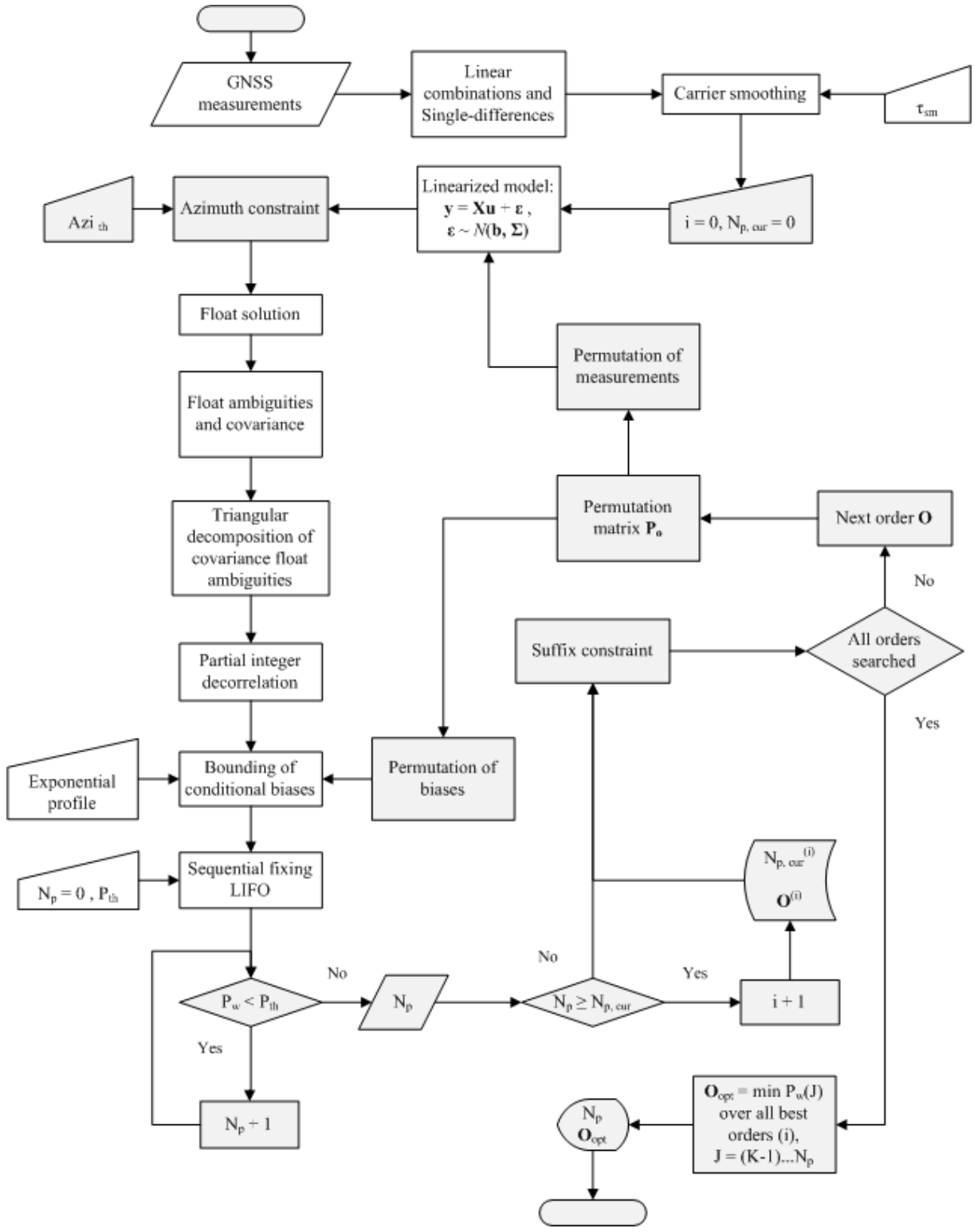

Figure 5.9: SOFOS method scheme.

with

$$P_s^{(i)}(\check{N}_i = N_i) = \Phi\left(\frac{1-2b_{\hat{N}_i}}{2\sigma_{\hat{N}_i}}\right) + \Phi\left(\frac{1+2b_{\hat{N}_i}}{2\sigma_{\hat{N}_i}}\right) - 1, \qquad \sigma_{\hat{N}_i} = \sqrt{\mathbf{\Sigma}_{\hat{N}}(i,i)}. \tag{5.10}$$

where $b_{\hat{N}_i}$ is the ith entry of the bias vector $\mathbf{b}_{\hat{\mathbf{N}}}$; and $\Phi(x)$ is the cumulative normal distribution given in Equation (3.67).

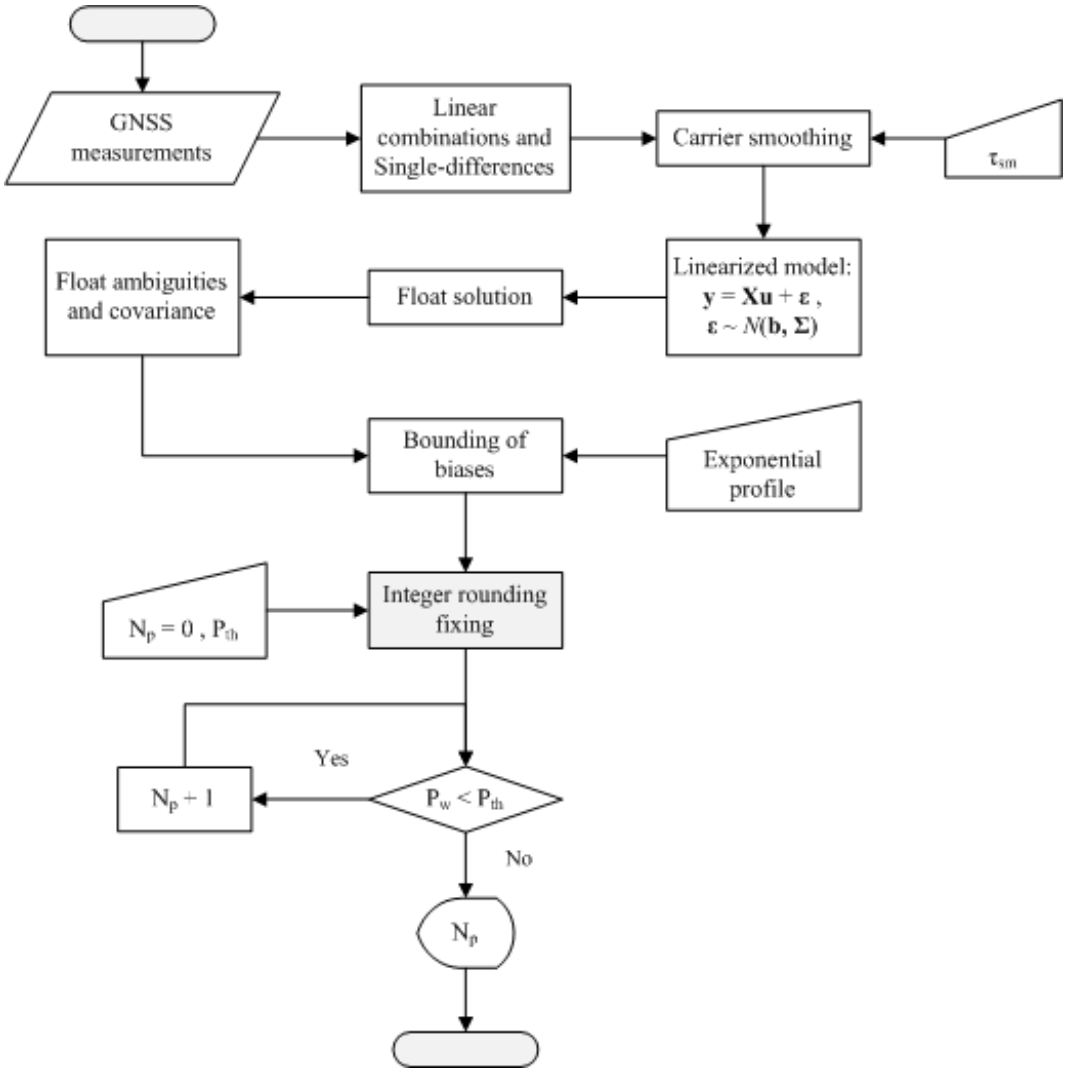

Figure 5.10: Rounding fixing scheme.

Chapter 6

Comparison of the partial ambiguity fixing methods

In the previous chapter, the different partial ambiguity fixing methods were described. It is now interesting to compare their performance for absolute carrier phase positioning with satellite-satellite single difference measurements in the presence of biases. For this purpose snapshots for simulations of Galileo measurements at 48.1507° latitude and 11.569° longitude, and through Europe are used. Moreover, an exponential bias profile with the parameters from Table 6.1, and a carrier smoothing time τ_{sm} of 20 seconds have been applied. Furthermore, the simulations are done without integer decorrelation of the ambiguities.

Table 6.1: Exponential bias profile for simulations.

	$b_{\phi,\max_{E1}}$	$b_{\phi,\max_{E5}}$	$b_{\rho,\max_{E1}}$	$b_{\rho,\max_{E5}}$
$\theta = 0°$	0.1 cyc.	0.1 cyc.	10 cm	10 cm
$\theta = 90°$	0.01 cyc.	0.01 cyc.	1 cm	1 cm

The dual frequency (E1-E5) GP-IF-NP code-carrier linear combination of maximum discrimination with a wavelength of 3.285 m is applied to the measurements. Furthermore, a probability of wrong fixing threshold P_{th} of 10^{-9} is taken into account for obtaining the largest subset of reliably fixable ambiguities $\mathbf{N}_p$ from each method. For the special case of the SOFOS method, a $\Delta Azi_{th} = 45°$ has been set in order to have a good trade-off with respect to the maximum number of fixable ambiguities.

The comparison of the methods will be done with respect to the new SOFOS method. The obtained bound on the biases, the standard deviations of the ambiguities, the probability of wrong fixings and the respective orders of fixings are analyzed for the different methods.

6.1 SOFOS and SAVO methods

The first method to be compared is the SAVO method. Figure 6.1 shows the probability of wrong fixing and a skyplot with the corresponding fixing orders obtained after using both methods. The satellite geometry consists of 8 satellites (i.e. $K = 8$). The reference satellite used for the single differences (SD) is marked in red in the skyplot. This is chosen to be the highest satellite in order to use it's higher precision. Although both methods begin to fix with the same satellite, from the remaining 7 single-difference ambiguities the SOFOS method fixes up to $N_p = 4$ ambiguities, while the SAVO method can fix only up to 3 ambiguities. This result is reflected on the probability of wrong fixing, where the characteristics of the methods are better recognized. The probability of wrong fixing of the SAVO method is very small for the first two ambiguities because these correspond to the two higher satellites ($\theta = 68°$ and $\theta = 52°$), however the third and fourth satellites to be fixed are lower in comparison to the last ones increasing thus faster the probability of wrong fixing, which exceeds the threshold after the fixing of the third ambiguity. In the case of the SOFOS method, this increment is slower because it prefers to fix at the second and third places lower satellites (approx. $\theta = 42°$ and $\theta = 29°$, respectively) sacrificing thus an acceptable reliability, but afterwards this is compensated by the next higher satellite to be fixed ($\theta = 52°$). A highly reliable fixing of the other three remaining satellites is not possible because of their very low elevation.

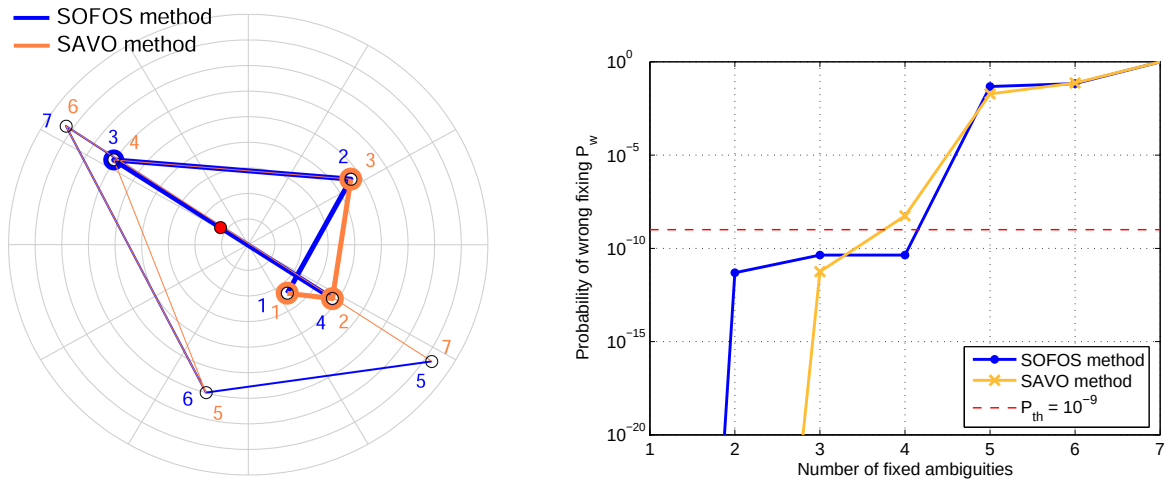

(a) Skyplot (order of fixings).

(b) Probability of wrong fixings.

Figure 6.1: Skyplot and probability of wrong fixing for a simulated Galileo geometry.

The corresponding conditional biases and standard deviations of the ambiguities for the previous satellite geometry are illustrated in Figure 6.2. In the case of the SAVO method, the conditional biases and standard deviations increase gradually for the first satellites. The conditional biases up to the fourth satellite reach approximately 0.31 cyc. which is not to high so far, however the respective conditional standard deviation is high enough (approx. 0.0325 cyc.) to prevent its reliable fixing. In the case of the SOFOS method, the conditional standard deviations are higher. Nevertheless, the fixing of more ambiguities can be possible due to the lower conditional biases. For example, the conditional bias of 0.2 cyc. compensates the high conditional standard deviation of 0.043 cyc for the second fixable ambiguity.

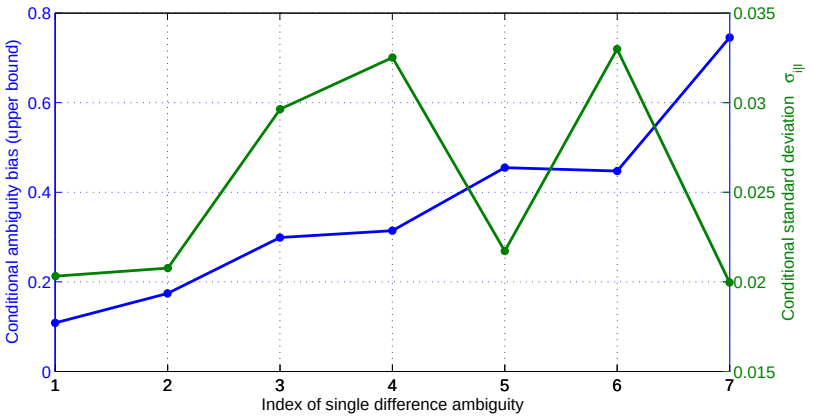

(a) SAVO method.

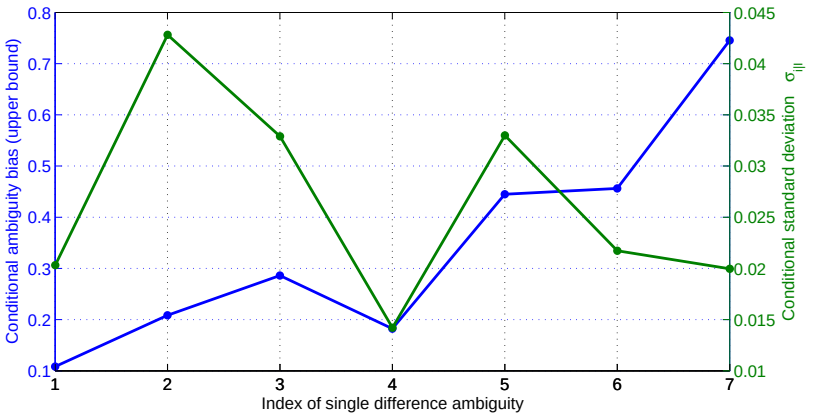

(b) SOFOS method.

Figure 6.2: Conditional ambiguity biases (upper bound) and conditional standard deviations.

A skyplot which contains the order of fixings, and the probability of wrong fixing for a different satellite geometry is showed in Figure 6.3. For this case with $K = 9$ satellites, the number of fixable ambiguities of the SOFOS method compared to of the SAVO method is rather higher. The SAVO method fixes only 2 of the 8 ambiguities, whereas the SOFOS method fixes up to 6 ambiguities. This benefit can be explained based on the satellite geometry, which consist only of medium and low elevated satellites. Therefore, the SAVO method performs badly due to the absence of high elevated satellites. On the other hand, the SOFOS method takes advantage of this geometry by fixing sequentially medium elevated satellites with a similar elevation from side to side, keeping the increment of the probability of wrong fixing slow. This is reflected on the conditional biases and standard deviations, which are illustrated for both methods in Figure 6.4, where the SOFOS conditional biases increase slowly while the conditional standard deviations decrease.

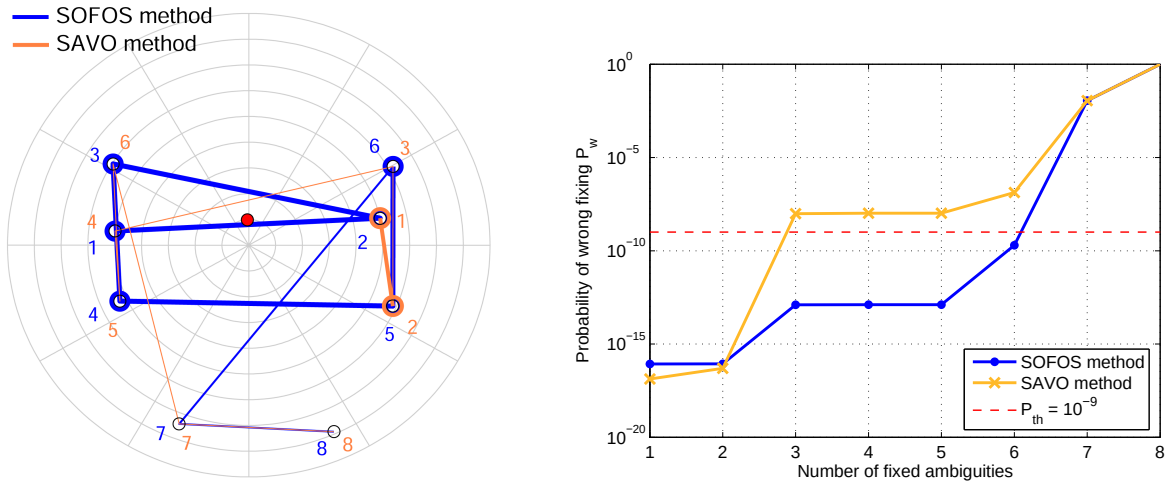

(a) Skyplot (order of fixings).

(b) Probability of wrong fixings.

Figure 6.3: Skyplot and probability of wrong fixing for a simulated Galileo geometry.

The performance on the number of fixable ambiguities obtained from both methods for different Galileo geometries is shown in Figure 6.5 and is further described on Table 6.2. The SOFOS method can fix in 51% of the times 2 or more ambiguities than the SAVO method; and in 84% of the times it can fix at least one ambiguity more.

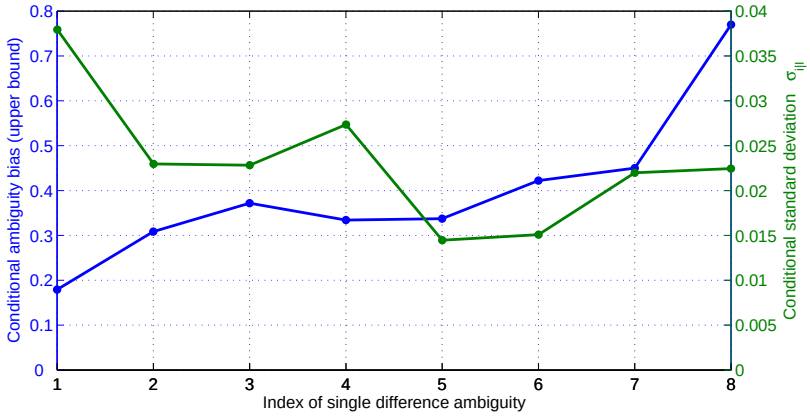

(a) SAVO method.

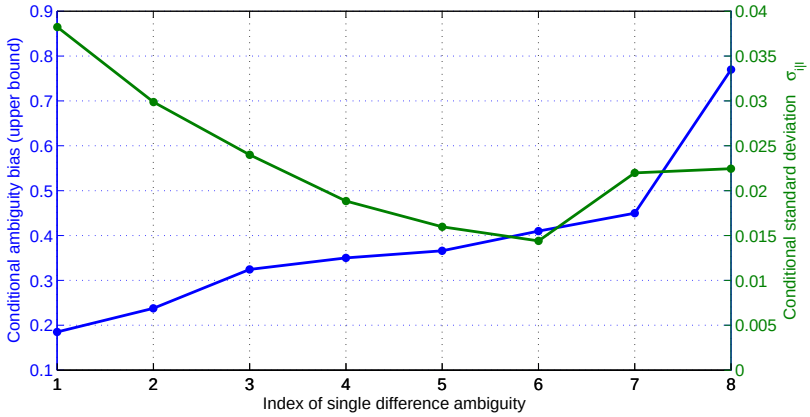

(b) SOFOS method.

Figure 6.4: Conditional ambiguity biases (upper bound) and conditional standard deviations.

Table 6.2: Performance description for the number of fixable ambiguities from Figure 6.5.

	SOFOS		SAVO	
N_p	n times	Percentage	n times	Percentage
6	5	10.22%	–	–
5	24	48.97%	6	12.24%
4	18	36.73%	2	4.08%
3	2	4.08%	33	67.35%
2	–	–	8	16.33%
Total	49	100%	49	100%

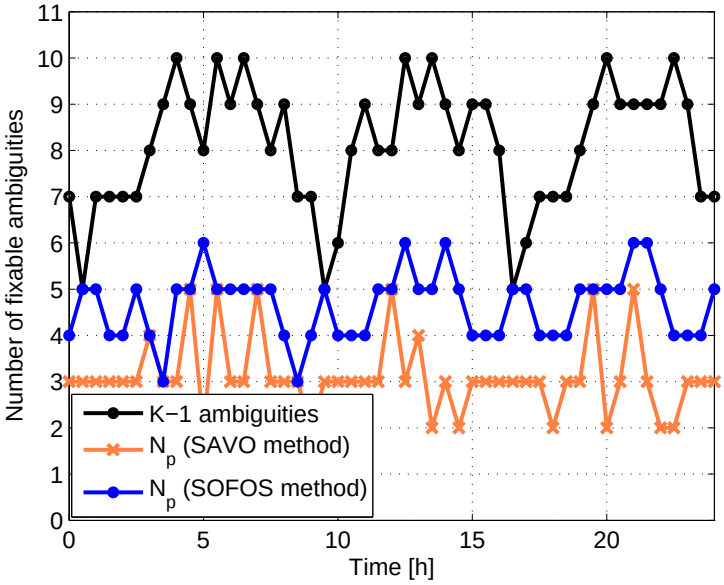

Figure 6.5: Number of fixable ambiguities N_p for different simulated Galileo geometries.

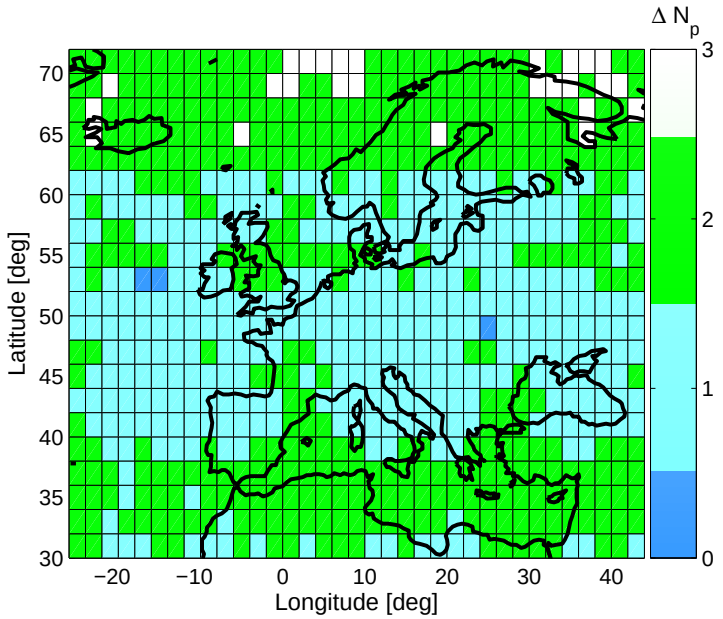

Figure 6.6: Benefit on the minimum number of maximum fixable ambiguities with a probability of wrong fixing lower than $P_{th} = 10^{-9}$ of the SOFOS method compared to the SAVO method for a snapshot through Europe.

Figure 6.6 shows the resulted benefit between the minimum number of the maximum fixable ambiguities for the methods through different locations in Europe. This means that the resulted worst cases in the maximum number of fixable ambiguities for each location from the SOFOS and the SAVO method are first chosen, and then the difference between them is calculated. This reads mathematically

$$\Delta N_p = \min_i N^{(i)}_{p,\max_{SOFOS}} - \min_i N^{(i)}_{p,\max_{SAVO}}. \tag{6.1}$$

Although the worst cases are considered, the SOFOS method can still fix up to 3 ambiguities more than the SAVO method in some locations. Moreover, the fixing of at least one more ambiguity occurs in 99.5% of the times.

6.2 SOFOS and SEBLO methods

The second method to be analyzed is the so-called SEBLO method. Figure 6.7 shows the probability of wrong fixing and a skyplot with the corresponding fixing orders for a selected snapshot. $K = 10$ visible satellites are available, from which the highest satellite (in red) is chosen as reference for the single differences. From the 9 ambiguities, the SEBLO method can fix up to 3, while the SOFOS method fixes up to 6 of them. In this case, the SOFOS method shows a similar behavior to the second case analyzed with the SAVO method in the previous section. It takes advantage from the medium elevated satellites geometry and prefers to lose some acceptable reliability in the first fixed ambiguities in order to fix more ambiguities while keeping their probability of wrong fixing almost flat. The remaining three ambiguities can not be fixed due to their lower elevation ($\theta < 18°$). On the other hand, the SEBLO method which based its order of fixing by taken the minimum probability of wrong fixing into account, shows a very low probability of wrong fixing for the first ambiguities, however this benefit is lost quickly after the fixing of the third ambiguity. The corresponding conditional biases and standard deviations are shown in Figure 6.8.

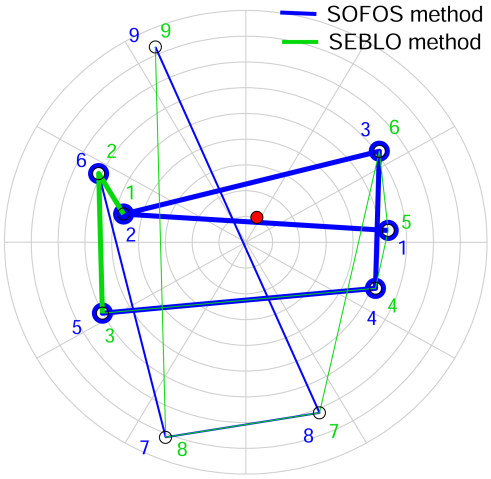

(a) Skyplot (order of fixings).

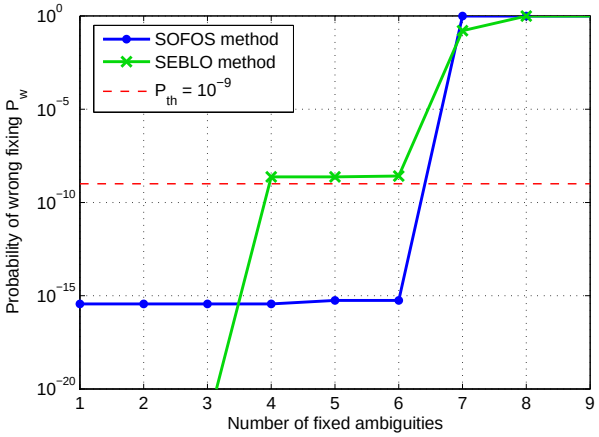

(b) Probability of wrong fixings.

Figure 6.7: Skyplot and probability of wrong fixing for a simulated Galileo geometry.

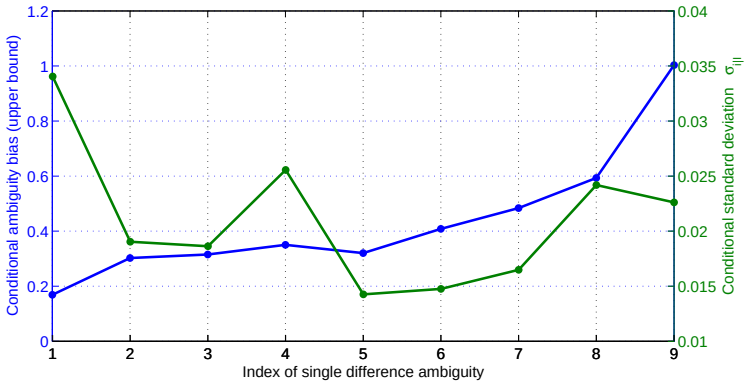

(a) SEBLO method.

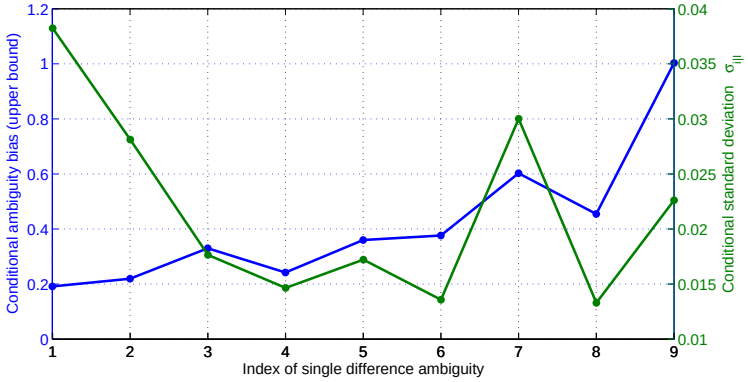

(b) SOFOS method.

Figure 6.8: Conditional ambiguity biases (upper bound) and conditional standard deviations.

A second geometry with $K = 10$ satellites is analyzed below. The corresponding skyplot and probability of wrong fixings are illustrated in Figure 6.9. In this case, the SEBLO method performs almost similar to the SOFOS method and can fix up to 5 of the 9 ambiguities. This similarity in the performance is better recognized in the respective conditional standard deviations and biases, which are shown in Figure 6.10. Both methods show a slowly increase of the conditional biases for the first 5 ambiguities, while their conditional standard deviation decreases. However, the conditional bias of the sixth ambiguity for the SEBLO method increases suddenly from 0.33 to 0.42 cyc. preventing its fixing, while the sixth ambiguity of the SOFOS method decreases due to its higher elevation compared to the last fixed ambiguity facilitating its reliable fixing.

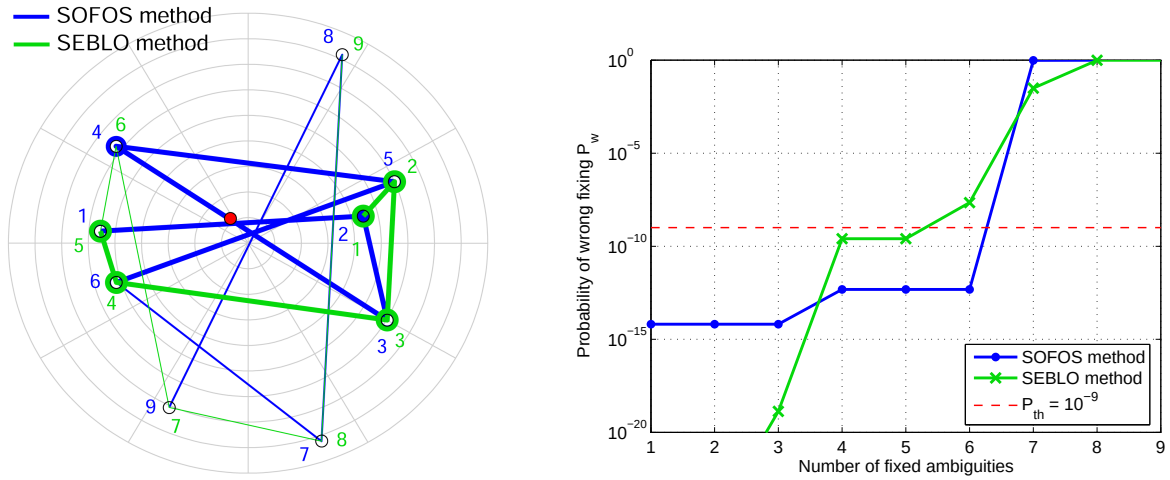

(a) Skyplot (order of fixings).

(b) Probability of wrong fixings.

Figure 6.9: Skyplot and probability of wrong fixing for a simulated Galileo geometry.

Table 6.3: Performance description for the number of fixable ambiguities from Figure 6.11.

	SOFOS		SEBLO	
N_p	n times	Percentage	n times	Percentage
6	5	10.22%	1	2.04%
5	24	48.97%	10	20.41%
4	18	36.73%	17	34.69%
3	2	4.08%	21	42.86%
Total	49	100%	49	100%

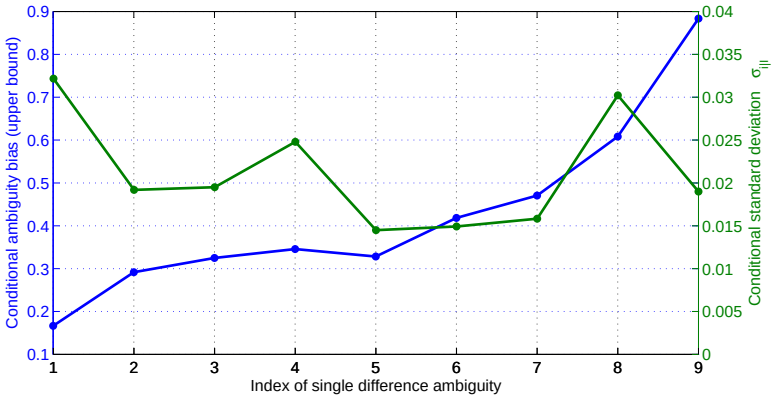

(a) SEBLO method.

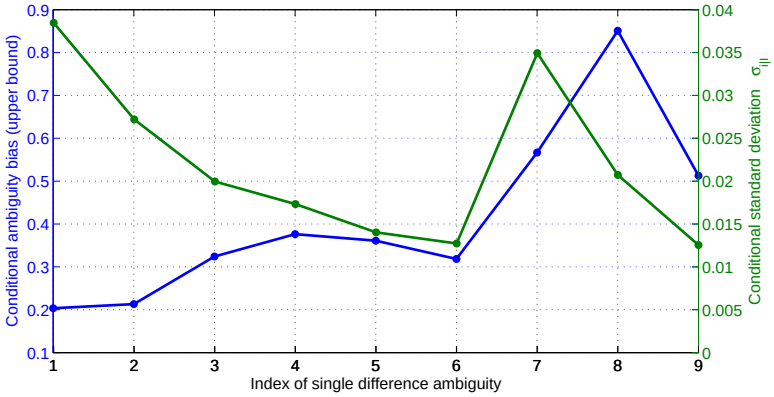

(b) SOFOS method.

Figure 6.10: Conditional ambiguity biases (upper bound) and conditional standard deviations.

Figure 6.11 depicts the number of fixable ambiguities obtained from both methods for different Galileo geometries. These results are further described on Table 6.3. The SOFOS method can fix in 16% of the times 2 or more ambiguities than the SEBLO method; and in 63% of the times it can fix at least one ambiguity more.

The resulted benefit between the minimum number of the maximum fixable ambiguities for the methods through different locations in Europe is shown in Figure 6.12. As explained in Section 6.1, this benefit is given by

$$\Delta N_p = \min_i N^{(i)}_{p,\max_{SOFOS}} - \min_i N^{(i)}_{p,\max_{SEBLO}}. \tag{6.2}$$

For this worst case, the SOFOS method can still fix up to 3 ambiguities more than the SEBLO method, but in less locations compared to the previous SAVO method. However, the fixing of at least one ambiguity more represents more than 65% of the times. On the other

hand, the effect of the azimuthal trade-off for the SOFOS method discussed on Section 5.4 takes place on this result, where the lost of one ambiguity occurs one time at 50° latitude and 24° longitude.

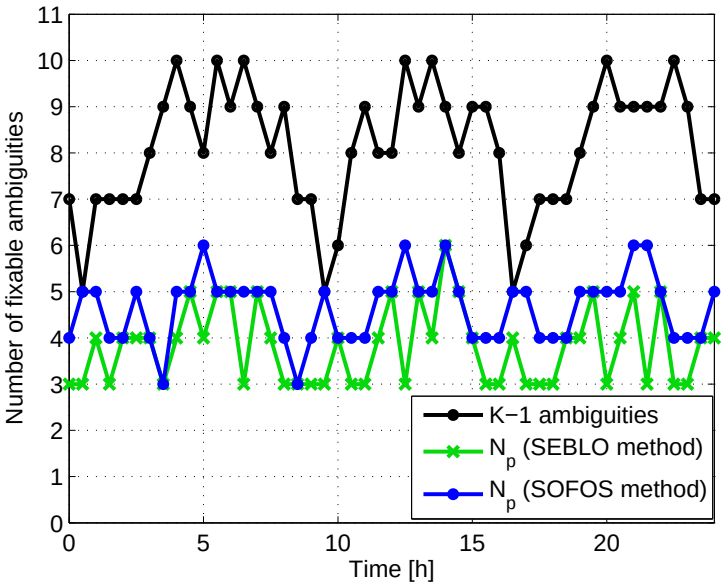

Figure 6.11: Number of fixable ambiguities N_p for different simulated Galileo geometries.

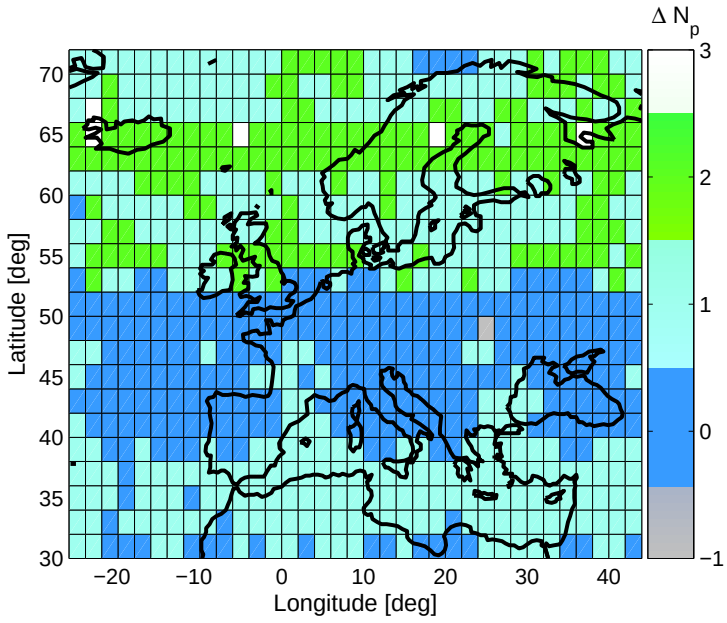

Figure 6.12: Benefit on the minimum number of maximum fixable ambiguities with a probability of wrong fixing lower than $P_{th} = 10^{-9}$ of the SOFOS method compared to the SEBLO method for a snapshot through Europe.

6.3 SOFOS and Rounding fixing methods

In this section the performance comparison between the Rounding fixing method which does not fix the ambiguities sequentially as the previous two methods and the SOFOS method is presented. Figure 6.13 shows the probability of wrong fixing and a skyplot for a snapshot of a selected geometry. In this case with $K = 9$ visible satellites, the Rounding fixing method fixes 3 of the 8 ambiguities, while the SOFOS method fixes up to 6 ambiguities. The order of fixing for the SOFOS method is shown as in the previous sections on the skyplot. For the batch case of the Rounding fixing method, the corresponding three fixed ambiguities are marked with a dashed circle. These ambiguities belongs actually to the three highest satellites as it was probably awaited. Figure 6.14 shows the conditional biases and standard deviations for the SOFOS method, and the biases and standard deviations of the ambiguities for the Rounding fixing method.

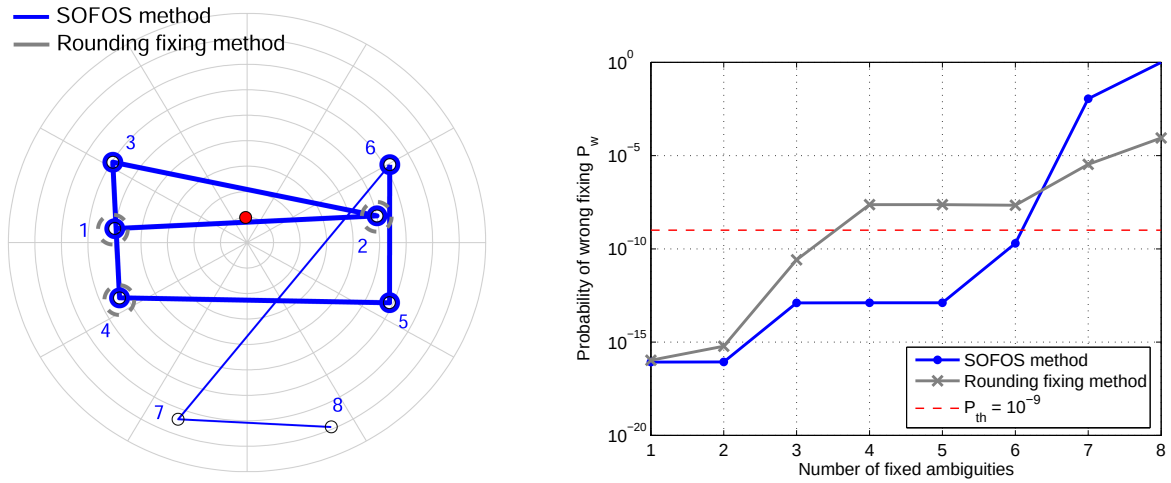

(a) Skyplot (order of fixings).

(b) Probability of wrong fixings.

Figure 6.13: Skyplot and probability of wrong fixing for a simulated Galileo geometry.

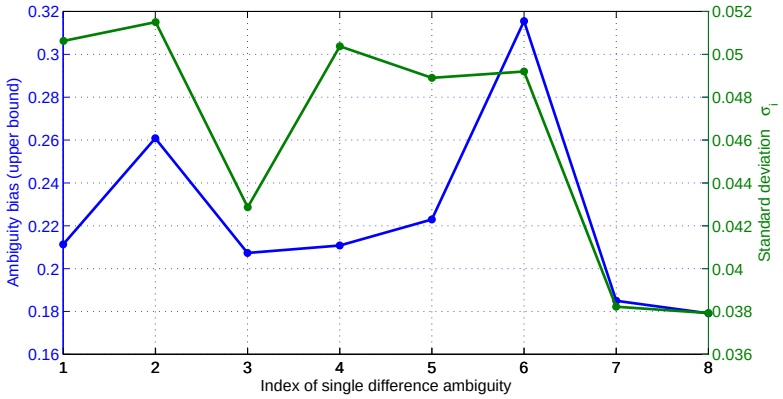

(a) Ambiguity biases (upper bound) and standard deviations (Rounding fixing method).

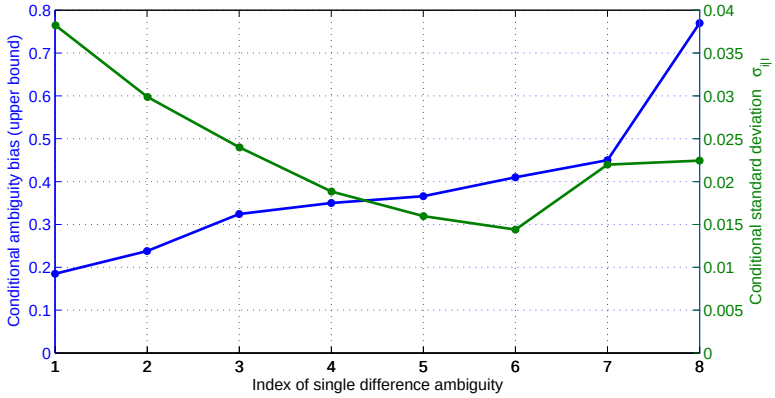

(b) Conditional ambiguity biases (upper bound) and conditional standard deviations (SOFOS method).

Figure 6.14: Biases and standard deviations for the SOFOS and Rounding fixing methods.

Figure 6.15 illustrates the probability of wrong fixing and the skyplot for a different satellite geometry which consists of $K = 9$ satellites. In a similar way as in the previous geometry, the Rounding fixing method concentrates on the fixing of the three highest satellites which in this case have an elevation above $\theta = 40°$. On the other hand, the SOFOS method fixes 5 ambiguities by using its characteristic of losing a little of reliability on the first fixable ambiguities while keeping almost flat the course of the probability of wrong fixing for the next fixed ambiguities. The corresponding biases and standard deviations are shown in Figure 6.16.

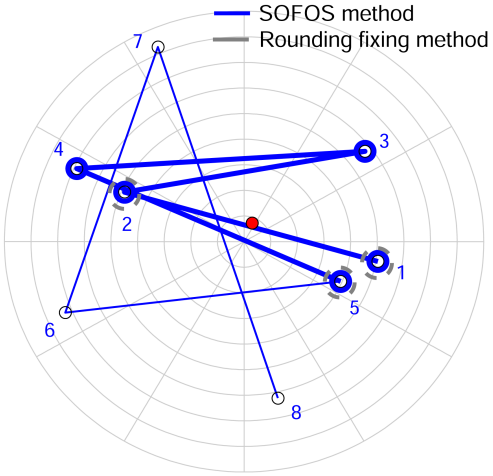

(a) Skyplot (order of fixings).

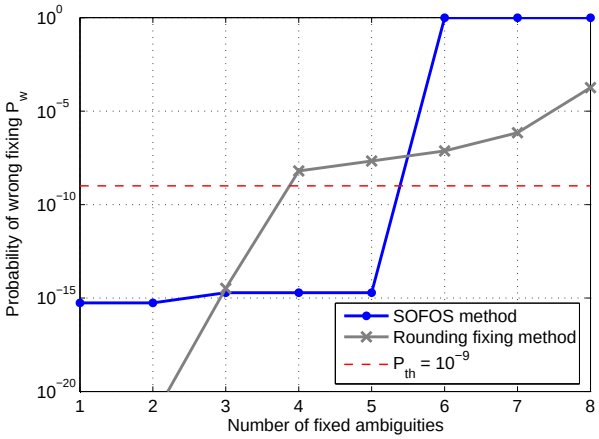

(b) Probability of wrong fixings.

Figure 6.15: Skyplot and probability of wrong fixing for a simulated Galileo geometry.

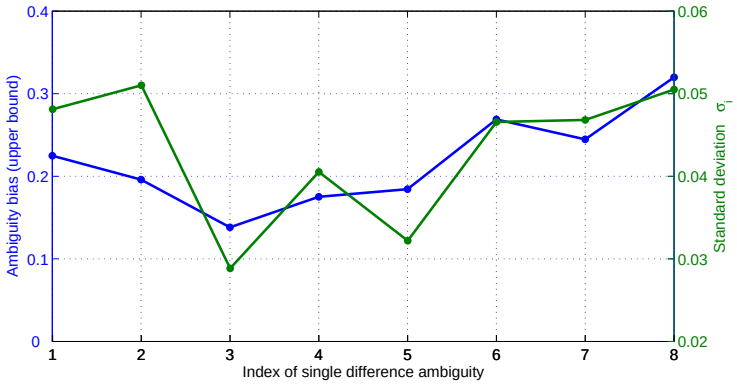

(a) Ambiguity biases (upper bound) and standard deviations (Rounding fixing method).

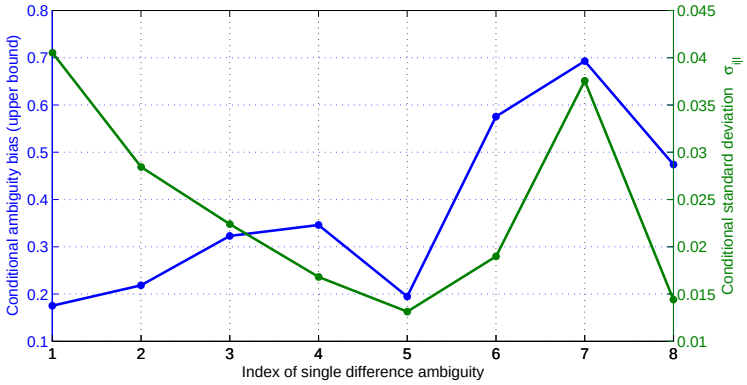

(b) Conditional ambiguity biases (upper bound) and conditional standard deviations (SOFOS method).

Figure 6.16: Biases and standard deviations for the SOFOS and Rounding fixing methods.

The obtained number of fixable ambiguities from the Rounding fixing and the SOFOS methods for different Galileo geometries are shown in Figure 6.17. The corresponding results are described on Table 6.4. The SOFOS method can fix in 33% of the times 2 or more ambiguities than the Rounding fixing method; and in 65% of the times it can fix at least one ambiguity more.

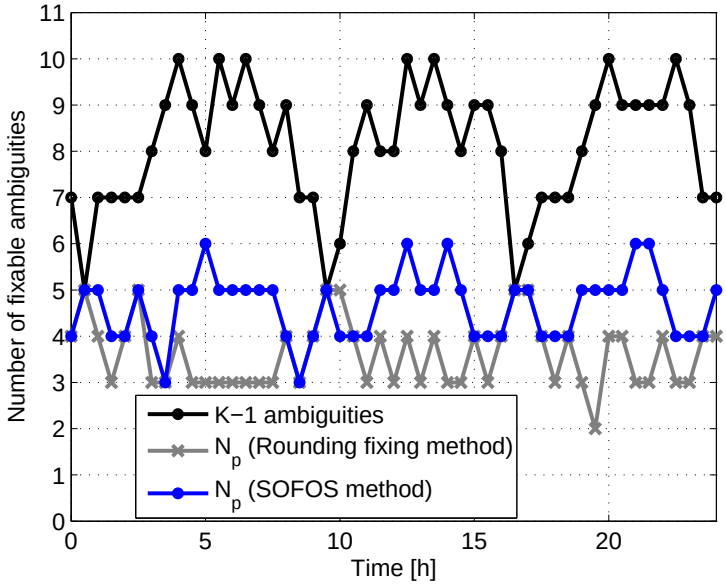

Figure 6.17: Number of fixable ambiguities Np for different simulated Galileo geometries.

Table 6.4: Performance description for the number of fixable ambiguities from Figure 6.17.

	SOFOS		Rounding fixing	
N_p	n times	Percentage	n times	Percentage
6	5	10.22%	–	–%
5	24	48.97%	6	12.24%
4	18	36.73%	19	38.78%
3	2	4.08%	23	46.94%
2	2	4.08%	1	2.04%
Total	49	100%	49	100%

The resulted benefit between the minimum number of the maximum fixable ambiguities for the methods through different locations in Europe is shown in Figure 6.18. This benefit is given by the following equation

$$\Delta N_p = \min_i N^{(i)}_{p,\max_{SOFOS}} - \min_i N^{(i)}_{p,\max_{Round}}. \tag{6.3}$$

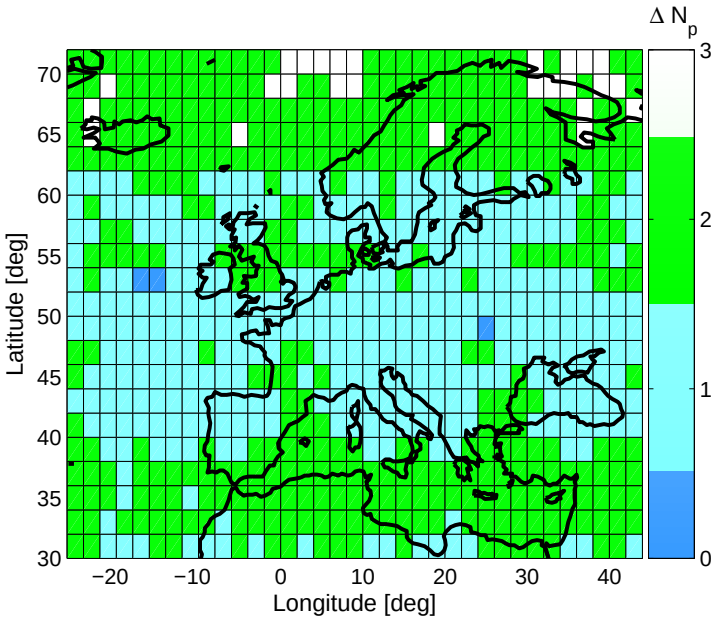

Figure 6.18: Benefit on the minimum number of maximum fixable ambiguities with a probability of wrong fixing lower than $P_{th} = 10^{-9}$ of the SOFOS method compared to the Rounding fixing method for a snapshot through Europe.

In this case, the resulted benefit is equal as for the SAVO method, i.e. the SOFOS method can fix up to 3 ambiguities more than the Rounding fixing method in some locations, and it fixes at least one more ambiguity in 99.5% of the times. However, this does not mean that both methods perform in the same manner.

Chapter 7

Summary and conclusions

In this thesis carrier phase ambiguity resolution in the presence of biases have been investigated for absolute positioning. Geometry-preserving, ionosphere-free mixed code-carrier linear combinations with two, three and four Galileo frequencies that maximize the ratio between wavelength and noise power have been derived. A four frequency (E1-E5a-E5b-E6) combination with a wavelength of 4.469 m and a low noise level of 6.34 cm have been found. Moreover, the dual frequency (E1-E5) mixed code-carrier linear combination with a wavelength of 3.285 m and a noise level of 19 cm, and an additional code-only linear combination have been considered in the analysis to improve the reliability of ambiguity resolution.

Satellite-satellite single differences are applied with the linear combinations for reduction of parameters on the measurements. The noise variance of the linear combinations is further reduced by using an ionosphere-free carrier smoothing.

An exponential bias profile, whose decay factor depends on the maximum and minimum assumed biases at $\theta = 90°$ and $\theta = 0°$ elevation angles, was used for upper bounding the residual phase and code biases on E1 and E5. This presence of biases on the measurements affects substantially the ambiguity resolution performed by the LAMBDA method, which usually achieves the integer least-square solution for unbiased measurements, since its ambiguity decorrelation transformation amplifies the biases while it reduces the variance. Therefore, a partial and non-integer decorrelation have been suggested to achieve an optimum variance and bias amplification trade-off.

A higher reliable resolution of all the ambiguities is prevented for significant biases. However, a subset of ambiguities can still be fixed sufficiently reliable. A new partial ambiguity fixing method has been developed for this reason. This so-called SOFOS method is based on a sequentially fixing of the ambiguities. It searches efficiently for the optimum order which

fixes the largest subset of reliably fixable ambiguities for a given probability of wrong fixing threshold.

The performance of the SOFOS method has been evaluated with another three partial ambiguity fixing methods: SAVO, SEBLO and Rounding fixing. As the SOFOS method, the SAVO and SEBLO methods are based on a sequentially fixing of the ambiguities, whereas the Rounding fixing method is based on a batch fixing. Simulations for different Galileo geometries were performed for making the comparison between the methods possible.

The obtained results shows that the SOFOS method performs rather better than the other methods on the achieved number of reliably fixable ambiguities at a single epoch. This benefit is possible due to its overall order search. Moreover, it fixes at least four ambiguities through Europe for a probability of wrong fixing of 10^{-9} and a carrier smoothing time of 20 seconds. The SAVO and Rounding fixing methods show a poor performance compared to the SOFOS and SEBLO methods. However, they are computationally simpler.

The SOFOS method demonstrates also that the order of fixing does not have to be started with the most precise ambiguity or in other words with the highest elevated satellite in order to achieve a larger subset of ambiguities.

The following further research on the implementation aspects for the SOFOS method are recommended:

- Lagrange optimization of multi-frequency GP-IF-NP linear combinations of maximum discrimination with constrained bias amplification

$$\max_{\alpha_m,\beta_m} D \quad = \quad \max_{\alpha_m,\beta_m} \frac{\lambda_{lc}}{2\sigma_n}, \tag{7.1}$$

  such that

$$\sum_{m=1}^{M} |\alpha_m| \cdot \lambda_m \cdot b_{\phi_m,\max} \quad + \quad \sum_{m=1}^{M} |\beta_m| \cdot b_{\rho_m,\max} \overset{!}{\leq} b_{\max}, \quad \text{for} \quad M \geq 2. \tag{7.2}$$

- Comparison of SOFOS with Integer Least-Squares Estimation (LAMBDA).
- Validation tests.

Appendix A

Differencing

In order to eliminate some parameters from the GNSS measurements, differencing is applied. This means that differences between the measurements from receivers and/or satellites are taken.

A.1 Single difference

By taking a difference of the measurements at two receivers (e.g. the user and the reference receiver) at the same epoch, the satellite clock and ephemeris errors cancels out in the difference. For simplicity, the time indices are omitted, and the code and carrier phase (ur) between-receiver SD measurements obtained from Equations (2.3) and (2.4) are modeled as

$$\rho^k_{ur,m} = \rho^k_{u,m} - \rho^k_{r,m} = r^k_{ur} + T^k_{ur} + q^2_{1m} I^k_{ur} + c(\delta\tau_{ur}) + b_{\rho_{ur,m}} + \varepsilon^k_{\rho_{ur,m}}, \tag{A.1}$$

$$\begin{aligned}\Phi^k_{ur,m} = \Phi^k_{u,m} - \Phi^k_{r,m} &= r^k_{ur} + T^k_{ur} - q^2_{1m} I^k_{ur} + \lambda_m N^k_{ur,m} + c(\delta\tau_{ur}) \\ &\quad + \lambda_m b_{\phi_{ur,m}} + \varepsilon^k_{\phi_{ur,m}},\end{aligned} \tag{A.2}$$

where $(\cdot)_{ur} = (\cdot)_u - (\cdot)_r$.

A.2 Double difference

The number of parameters can be further reduced by taking between-receiver and between-satellite double differences (DD). The obtained code and carrier phase DD measurements are modeled as

$$\rho_{ur,m}^{kl} = \rho_{ur,m}^{k} - \rho_{ur,m}^{l} = r_{ur}^{kl} + T_{ur}^{kl} + q_{1m}^{2} I_{ur}^{kl} + \varepsilon_{\rho_{ur,m}}^{kl}, \tag{A.3}$$

$$\Phi_{ur,m}^{kl} = \Phi_{ur,m}^{k} - \Phi_{ur,m}^{l} = r_{ur}^{kl} + T_{ur}^{kl} - q_{1m}^{2} I_{ur}^{kl} + \lambda_m N_{ur,m}^{kl} + \varepsilon_{\phi_{ur,m}}^{kl}, \tag{A.4}$$

where $(\cdot)_{ur}^{kl} = (\cdot)_{ur}^{k} - (\cdot)_{ur}^{l}$; and the relative receiver clock biases from the single-difference measurements have now also cancelled.

Appendix B

Cardano's method

A cubic function, in mathematics, is a function of the form

$$f(x) = ax^3 + bx^2 + cx + d, \qquad \text{with} \quad a \neq 0. \tag{B.1}$$

By setting $f(x) = 0$, the following cubic equation is generated

$$ax^3 + bx^2 + cx + d = 0. \tag{B.2}$$

In order to solve a cubic equation, which accounts to find the roots of a cubic function, one can uses the Cardano's method. It is named after the Italian mathematician Gerolamo Cardano, and is described by the following steps:

1. The standard cubic equation is divided by the first coefficient a and the following equation is obtained:

$$x^3 + \dot{a}x^2 + \dot{b}x + \dot{c} = 0, \qquad \dot{a} = \tfrac{b}{a} \quad \dot{b} = \tfrac{c}{a} \quad \dot{c} = \tfrac{d}{a}. \tag{B.3}$$

2. Substitute $x = z - \dot{a}/3$ in order to eliminate the quadratic term and obtain the following *depressed cubic equation*:

$$z^3 + pz + q = 0, \tag{B.4}$$

with the coefficients

$$p = \dot{b} - \frac{\dot{a}^2}{3} \qquad \text{and} \qquad q = \dot{c} + \frac{2\dot{a}^3 - 9\dot{a}\dot{b}}{27} \tag{B.5}$$

3. Substitute $z = u + v$ into Equation B.4 to obtain

$$u^3 + v^3 + (3uv + p)(u + v) + q = 0. \tag{B.6}$$

4. Substitute the condition $(3uv + p) = 0$ proposed by Cardano into the previous equation:

$$u^6 + qu^3 - \frac{p^3}{27} = 0, \tag{B.7}$$

where this equation can be seen as a quadratic equation for u^3.

5. Solve the previous equation as a quadratic equation to get:

$$u^3 = -\frac{q}{2} \pm \sqrt{\frac{q^2}{4} + \frac{p^3}{27}} \qquad \rightarrow u = \sqrt[3]{-\frac{q}{2} \pm \sqrt{\frac{q^2}{4} + \frac{p^3}{27}}}. \tag{B.8}$$

6. Since $z = x + \dot{a}/3 = u + v$, this results in

$$x = u + v - \frac{\dot{a}}{3}, \qquad \text{with} \quad v = -\frac{p}{3u} \qquad \text{then} \quad x = u - \frac{p}{3u} - \frac{\dot{a}}{3}. \tag{B.9}$$

Where the three roots x_1, x_2, x_3 for the cubic equation (B.2) are obtained by substituting the three values obtained for u from Equation (B.8).

Appendix C

Kronecker product

The *Kronecker product*, denoted by $\otimes$, is named after the German mathematician and logician Leopold Kronecker. It is an operation on two matrices of arbitrary size resulting in a block matrix.

If A is an $m \times n$ matrix and B is a $p \times q$ matrix, then their Kronecker product is defined as the following $mp \times nq$ matrix

$$A \otimes B = \begin{pmatrix} a_{11}B & \dots & a_{1n}B \\ \vdots & \ddots & \vdots \\ a_{m1}B & \dots & a_{mn}B \end{pmatrix}. \tag{C.1}$$

It has the following properties:

$$\begin{aligned} (A+B) \otimes C &= A \otimes C + B \otimes C \\ A \otimes (B+C) &= A \otimes B + A \otimes C \\ (A \otimes B) \otimes C &= A \otimes (B \otimes C) \\ (A \otimes B)(C \otimes D) &= (AC \otimes BD) \\ (A \otimes B)^T &= A^T \otimes B^T \\ (A \otimes B)^{-1} &= A^{-1} \otimes B^{-1} \end{aligned}$$

Note: The Kronecker product is *not commutative* $A \otimes B \neq B \otimes A$.

Appendix D

Further SOFOS simulations

The following simulations of Galileo measurements for the SOFOS method are also based on the same parameters used for the comparison between the methods in Chapter 6, except for the carrier smoothing time τ_{sm}, whose value is given for each figure. Moreover, an azimuthal threshold $\Delta Azi_{th} = 45°$ is also used for the SOFOS method, and a probability of wrong fixing threshold $P_{th} = 10^{-9}$ is considered.

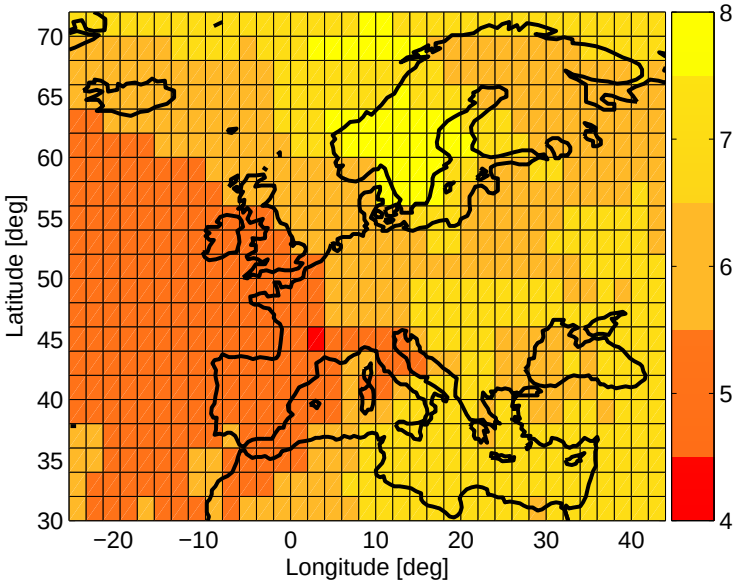

Figure D.1: Number of fixable ambiguities N_p for a snapshot through Europe. ($\tau_{sm} = 30$ s)

Figure D.1 and Figure D.2 show that at least four ambiguities can be fixed through Europe and for different geometries. Moreover, in 98% of the times at least 5 ambiguities can be fixed in both scenarios.

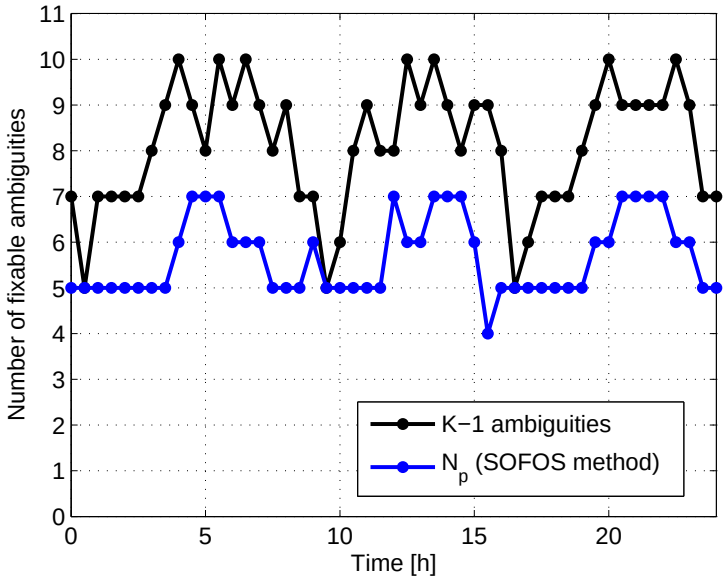

Figure D.2: Number of fixable ambiguities N_p for different simulated Galileo geometries. ($\tau_{sm} = 30$ s)

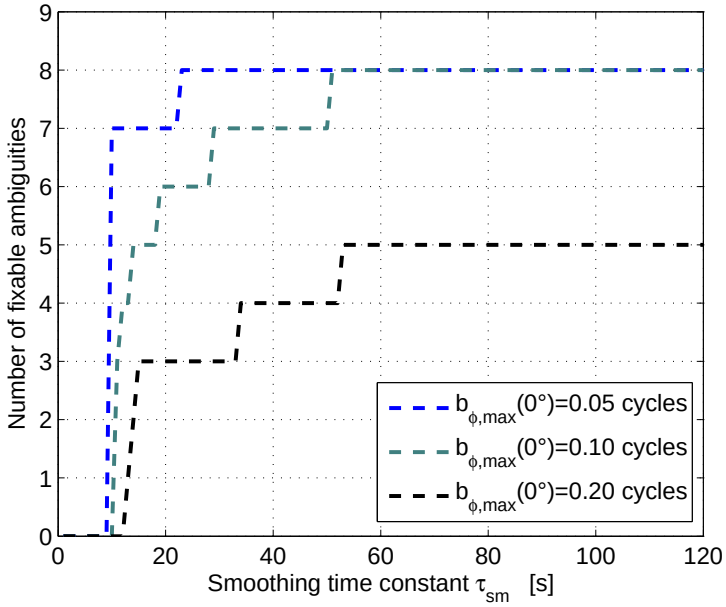

Figure D.3: Impact of the carrier smoothing time on the number of fixable ambiguities N_p. ($b_{\rho,\max}(0°) = 5$ cm)

The impact of the smoothing time on the number of fixable ambiguities is shown in Figures D.3 and D.4 for different code and phase biases. N_p converges to the number of conditional biases which are smaller than 0.5 cycles, when large smoothing periods are applied.

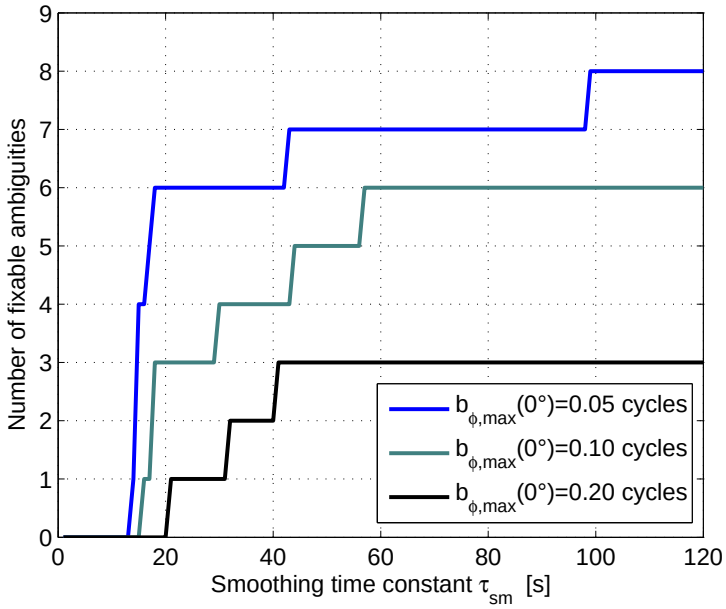

Figure D.4: Impact of the carrier smoothing time on the number of fixable ambiguities N_p. ($b_{\rho,\max}(0°) = 10$ cm)

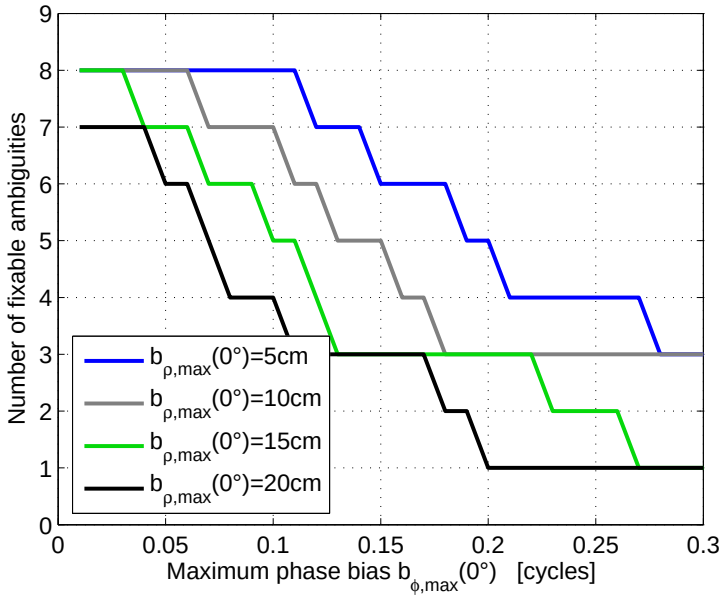

Figure D.5: Impact of the biases exponential profile on the number of fixable ambiguities N_p. ($\tau_{sm} = 30$ s)

Bibliography

[1] P.J.G. Teunissen, *Least-squares estimation of the integer ambiguities*, Invited lecture, Section IV, Theory and Methodology, IAG General Meeting, Beijing, China, 1993.

[2] P. de Jonge and C. Tiberius, *The LAMBDA method for integer ambiguity estimation: implementation aspects*, Publications of the Delft Geodetic Computing Centre, No. 12, Aug. 1996.

[3] P.J.G. Teunissen, *An optimality property of the integer least-squares estimator*, Journal of Geodesy, Vol.73, pp. 587-593, Springer, 1999.

[4] W. Cao, K. O'Keefe and M. Cannon, *Partial Ambiguity Fixing within Multiple Frequencies and Systems*, Proceedings of ION GNSS 20th International Technical Meeting 2007, pp. 312-323, Fort Worth, TX, USA, September 2007.

[5] P. Misra and P. Enge, *Global Positioning System: Signals, Measurements, and Performance*, 2nd Edition, Ganga-Jamuna Press, Lincoln, MA, 2006.

[6] InsideGNSS, *GPS, GLONASS, Galileo, Compass*, Online: http://www.insidegnss.com/.

[7] S. Verhagen, *The GNSS integer ambiguities estimation and validation*, Dissertation, Delft University of Technology, 2004.

[8] J.A. Ávila, *The MBOC Modulation A Final Touch for the Galileo Frequency and Signal Plan*, Online: http://www.insidegnss.com/node/174, September/October 2007.

[9] B. Forssell, M. Martin-Neira, and R. A. Harris, *Carrier phase ambiguity resolution in GNSS-2*, Proceedings of ION GPS 10th International Technical Meeting 1997), Vol. 2, pp. 17271736, Kansas City, MO, USA, September 1997.

[10] P.J.G. Teunissen and S. Verhagen, *GNSS Phase Ambiguity Validation: A Review*, Proceedings Space, Aeronautical and Navigational Electronics Symposium (SANE), The Institute of Electronics, Information and Communication Engineers (IEICE), Vol.107, No.2, pp. 1-6, Japan, 2007.

[11] P. Henkel and C. Günther, *Joint L/C-Band Code-Carrier Linear Combinations for Galileo*, International Journal of Navigation and Observation, Special Issue on Future GNSS Signals, Hindawi Publ., Jan. 2008.

[12] P. Henkel and C. Günther, *Precise Point Positioning with multiple Galileo frequencies*, Proceedings of the Positioning, Location and Navigation Symposium (PLANS), Monterey, USA, pp. 592-599, May 2008.

[13] J. Betz, *Binary Offset Carrier Modulations for Radionavigation*, Navigation, Vol. 48, No. 4, pp. 227-246, 2002.

[14] P. Henkel, V. Gómez and C. Günther, *Modified LAMBDA for absolute carrier phase positioning in the presence of biases*, ION International Technical Meeting 2009, Anaheim, CA, USA, January 2009.

[15] R. R. Hatch, *A new three-frequency, geometry-free, technique for ambiguity resolution*, Proceedings of ION GNSS 19th International Technical Meeting 2006, Vol.1, pp. 309-316, Fort Worth, TX, USA, September 2006.

[16] P. Hwang, G. Graw and J. Bader, *Enhanced Differential GPS Carrier-Smoothed Code Processing Using Dual-Frequency Measurements*, Journal of Navigation, Vol. 46, No. 2, pp. 127-137, Summer 1999.

[17] P.J.G. Teunissen, *On the integer normal distribution of the GPS ambiguities*, Artificial satellites, Vol.33, No.2, pp. 49-64, 1998.

[18] N.F. Jonkman, *Integer GPS ambiguity estimation without the receiver-satellite geometry*, Delft Geodetic Computing Center,LGR series No.18, Delft University of Technology, 95pp.

[19] G. Blewitt, *Carrier-phase ambiguity resolution for the Global Positioning System applied to geodetic baselines up to 2000 km*, Journal Geophysic Research, Vol. 94, pp. 10187-10203, 1989.

[20] D. Odijk, *Fast precise GPS positioning in the presence of ionospheric delays*, Doctoral Thesis, Delft University of Technology, 2002.

[21] P.J.G. Teunissen, *The parameter distributions of the integer GPS model*, Journal of Geodesy, Vol.76, pp. 41-48, 2002.

[22] P.J.G. Teunissen, *Success Probability of Integer GPS Ambiguity Rounding and Bootstrapping*, Journal of Geodesy, Vol.72, No.10, pp. 606-612, Springer, 1998.

[23] P.J.G. Teunissen, *A canonical theory for short GPS baselines. Part IV: Precision versus reliability*, Journal of Geodesy, Vol.71, pp. 513-525, Springer, 1997.

[24] P.J.G. Teunissen, *Integer estimation in the presence of biases*, Journal of Geodesy, Vol.75, pp. 399-407, Springer, 2001.